# Development of On-line Coupled Capillary Electrophoresis to Portable Microcoil NMR Detection

Von der Naturwissenschaftlichen Fakultät

der Gottfried Wilhelm Leibniz Universität Hannover

zur Erlangung des Grades

Doktorin der Naturwissenschaften

Dr. rer. nat.

genehmigte Dissertation

von

M. Sc. Joana Diekmann

geboren am 17.06.1985, in Berlin

2012

Referentin: Prof. Dr. Carla Vogt

Korreferent: Prof. Dr. Helmut Duddeck

Tag der Promotion: 25.09.2012

*Dedicated to my Family*

The present work was carried out between October 2009 and September 2012 (36 months) at the following institutes:

**Gottfried Wilhelm Leibniz University Hannover (19 months)**
Faculty of Natural Sciences
**Home Supervisor:** Prof. Dr. Carla Vogt
Institute of Inorganic Chemistry
Department of Analytical Chemistry
Callinstraße 1, 30167 Hannover
Germany

**Lawrence Livermore National Laboratory (13 months)**
Physical and Life Sciences Directorate
**Local Supervisors:** Dr. Gregory L. Klunder and Dr. Kristl L. Adams
Chemical Sciences Division
7000 East Avenue, Livermore, CA 94550
USA

**ABQMR (2 months)**
Innovations in Magnetic Resonance
**Local Supervisor:** Dr. Andrew McDowell
2301 Yale Blvd. SE, Suite C-2, Albuquerque, NM 87106
USA

**Leibniz-Institut für Analytische Wissenschaften – ISAS – e.V. (2 months)**
Institute for Analytical Sciences
**Local Supervisors**: Dr. Jörg Lambert and Dr. Roland Hergenröder
Institute Material Analysis
Bunsen-Kirchhoff-Str. 11, 44139 Dortmund
Germany

# Acknowledgements

I would like to thank all persons who provided support and encouragement throughout the pursuit of this project. In particular:

First and foremost, I would like to thank my home supervisor Prof. Dr. Carla Vogt for the continuous support of my study and research.

My sincere thanks also go to my LLNL local supervisors Dr. Gregory L. Klunder and Dr. Kristl L. Adams for offering me the opportunities to work at LLNL, for their patience, motivation, enthusiasm and inspiring discussions.

My special thanks are dedicated to Dr. Andrew McDowell at ABQMR for his technical advice and tremendous help with the experimental work, for his encouragement, insightful comments, and excellent support in every sense. Furthermore, I would like to deeply thank and acknowledge Dr. Eiichi Fukushima to give me the opportunity to work at his research facility and for his helpful conversations.

Special thanks to Dr. Roland Hergenröder, Dr. Jörg Lambert, and Dr. Ahmad Telfah from the ISAS institute, who gave me the opportunity to work with microslot NMR probeheads.

I would like to thank Prof. Dr. Helmut Duddeck for being my second supervisor and introducing me to NMR.

Furthermore, I thank the German Academic Exchange Service (DAAD) as well as the DFG (Vo 579/19-1) for the financial support; Dipl.-Ing. Thorleif Hentrop, Burghard Probst, and F. Rebentrost for the technical support. Thanks to Bob Lown for his help with the magnet and to Marian Buszko for his tremendous support with the portable NMR.

Thanks to my master and bachelor students for their passionate participation in different parts of this project.

Special thanks to my friends and colleagues of the “AK Analytik” for the joyful time that we have spent together and their encouragement and help in a lot of different ways.

Finally, I would like to thank my family and friends for the encouragement during my studies and supporting me spiritually throughout my life.

# Abstract

Miniaturizing analytical techniques for chemical analysis is one of the major focal points in research. A portable capillary electrophoresis (CE) coupled to a miniaturized nuclear magnetic resonance (NMR) instrument provides several advantages for applications in analytical chemistry, pharmaceutical industries, and academia. This analytical system requires nanoliter to microliter sample volumes, and has reduced instrument and operating costs, small laboratory footprint, and minimal instrument maintenance. Hyphenating CE with the non-destructive, microcoil NMR detection system provides the ability to identify components in a complex mixture by first separating the compounds chemically and then providing on-line structural identification of the analytes.

This work demonstrates the development of a miniaturized, custom-built CE-NMR device based on a portable CE and a briefcase-sized microcoil NMR system with a small 1.6 T permanent magnet as well as integrated shim coils that achieves 0.2-0.02 ppm $^{1}H$ and $^{19}F$ NMR resolution and detects analytes at sub-molar concentrations. Several technical challenges and design solutions were encountered in the development of this portable, coupled CE-NMR system, which are described in detail. Chemical structural determination via NMR requires concentrated samples in the range of 500 mM, yet concentrated mixtures are difficult to separate via CE; electrophoretic chemical preconcentration of long chain perfluorinated carbonic acids is demonstrated using various stacking techniques along with simultaneous separation of these concentrated sample mixtures. $^{19}F$ and $^{1}H$ NMR spectra of numerous weak organic acids, such substances of environmental and medical concern, are presented. Further, a custom flow cell capillary is utilized to increase the NMR detector volume. Weak signal peaks tend to disappear with magnet temperature drifts; magnet insulation and temperature drift post processing are employed to counter environmental temperature drifts. NMR line broadening due to CE current effects is resolved by incorporating a simple calculated shim adjustment based on the value of the CE current. This important result allows continuous current-flow CE-NMR measurements in the portable device without applying any further hardware developments.

Individual system hardware design, instrumental setup, operating parameters, methodological developments, and system integration are discussed separately with representative data and calculations. Results demonstrate the successful development of a new, unique portable CE-NMR technology which achieves sample component separation via CE and uses NMR as the information-rich detector for structural elucidation.

**Keywords:** Portable NMR, Custom-Built CE, Microcoils, Hyphenated CE-NMR System

# Zusammenfassung

Die Miniaturisierung von analytischen Messmethoden für die chemische Analyse ist ein wichtiger Bereich in der Wissenschaft. Eine portable Kapillarelektrophorese (CE), welche an ein miniaturisiertes Kernspinresonanz-Spektrometer (NMR) gekoppelt ist, bietet einige Vorteile für die Anwendungen in der analytischen Chemie, der pharmazeutischen Industrie sowie im Hochschulbereich. In diesem analytischen Messinstrument werden Nanoliter bis Mikroliter Probenvolumen benutzt, wobei die Instrument- und Bedienungskosten, die Laborstandfläche und die Wartungsarbeiten reduziert sind. Die Kopplung von CE mit dem zerstörungsfreien, Mikrospulen NMR Detektor ermöglicht die Identifikation von Komponenten in einem komplexen Gemisch, wobei erst die Substanzen chemisch aufgetrennt werden und dann eine on-line Strukturidentifikation der Analyten erfolgt.

Die vorliegende Arbeit präsentiert die Entwicklung eines miniaturisierten, eigens angefertigten CE-NMR Gerätes, welches auf einer tragbaren CE und einem Aktenkoffer-großen Mikrospulen NMR System, mit sowohl einem kleinen 1,6 T Permanentmagneten als auch integrierten Korrekturspulen, basiert. Das Gerät erreicht für $^{1}H$ und $^{19}F$ NMR Auflösungen von 0,2-0,02 ppm und Analyten im unteren molaren Konzentrationsbereich können detektiert werden. Mehrere technische Herausforderungen und Designlösungen mussten während der Entwicklung dieses tragbaren, gekoppelten CE-NMR Systems überwunden werden, wie im Detail beschrieben wird. Chemische Strukturaufklärung via NMR erfordert Probenkonzentrationen im Bereich von 500 mM, jedoch sind diese konzentrierten Gemische sehr schwer mit Hilfe der CE zu trennen. Eine elektrophoretische Aufkonzentrierung von langkettigen, per-fluorierten Carbonsäuren wird präsentiert, wobei verschiedene Stacking-Techniken zusammen mit einer simultanen Trennung der hoch konzentrierten Probengemische verwendet werden. Von zahlreichen, schwachen organischen Säuren, die ökologisch oder medizinisch bedenklich sind, wurden $^{19}F$ und $^{1}H$ NMR Spektren aufgenommen. Des Weiteren wird eine eigens hergestellte Durchfluss-Kapillare benutzt, um das NMR Detektionsvolumen zu vergrößern. Da schwache NMR Signale dazu neigen mit den Temperaturveränderungen des Magneten zu verschwinden, wurden Magnetisolierungen und Datennachbearbeitungen in Abhängigkeit von der Temperatur-veränderung benutzt. Die NMR Signalverbreiterung auf Grund des CE Stroms wurde mit Hilfe einer integrierten Berechnung über die Korrekturspulen, basierend auf dem jeweiligen Stromwert, minimiert. Die Lösung dieses fundamentalen Problems erlaubt kontinuierliche CE-NMR Messungen in dem portablen Gerät, wobei der CE Strom nicht zwischenzeitlich für die NMR Messungen abgeschaltet werden muss und keine weiteren Hardware Entwicklungen nötig sind.

Individuelles Hardware-Design des Instruments, Gerätekonfigurationen, Bedienparameter, methodische Entwicklungen sowie Systemintegrationen werden separat mit repräsentativen Ergebnissen und Berechnungen in den einzelnen Kapiteln diskutiert. Die Ergebnisse zeigen die erfolgreiche Entwicklung einer neuen, innovativen und tragbaren CE-NMR Technologie, die Probenbestandteile mit Hilfe der CE auftrennt und mit dem informationsreichen NMR Detektor Strukturaufklärungen durchführt.

**Schlagwörter:** Portable NMR, Eigenbau CE, Mikrospulen, gekoppeltes CE-NMR System

# Table of Contents

**LIST OF SYMBOLS AND ABBREVIATIONS** ..... **III**

**AIMS AND CONCEPT** ..... **1**

**1 MOTIVATION AND INTRODUCTION** ..... **2**

**2 HARDWARE DEVELOPMENT** ..... **7**

**2.1 PORTABLE CE** ..... **7**
2.1.1 Instrument Setup ..... 7
2.1.2 High Voltage Power Supply ..... 8
2.1.3 UV/Vis Detection ..... 9
2.1.3.1 Smoothing Algorithms ..... 9
2.1.3.2 Comparison of Portable Spectrometers ..... 12
2.1.3.3 Comparison of Portable CE and Lab-Scale CE Spectrometers ..... 13
2.1.4 Injection Technique ..... 15
2.1.4.1 Validation of Siphoning Injection Technique ..... 16
2.1.5 Capillary Temperature Control ..... 17
2.1.5.1 Ohm's Law Plots ..... 18
2.1.5.2 Long-Term Voltage Experiments ..... 19
2.1.6 CE Separation, Characterization and Quantification on Commercial CE System ..... 20
2.1.6.1 Glycyl-Glycin and TFA Separation ..... 20
2.1.6.2 PFPA and TFA Separation ..... 21
2.1.6.3 Quantification of High Concentrated Sample Mixtures ..... 22
2.1.7 CE Separation on Portable CE System ..... 23
2.1.8 Preconcentration Techniques on Commercial CE System ..... 24
2.1.8.1 tITP-CE Method ..... 24
2.1.8.2 LVSEP Method ..... 27
**2.2 PORTABLE NMR** ..... **29**
2.2.1 Instrument Setup and Experimental Parameters ..... 29
2.2.2 Microcoil Probehead ..... 30
2.2.2.1 Challenges in the Microcoil Design for the CE-NMR Integration ..... 31
2.2.2.2 Slotted Microcoil Assembly ..... 32
2.2.2.3 Solenoidal Microcoil Assembly ..... 35
2.2.3 NMR Magnet ..... 38
2.2.3.1 Magnet Construction and Shim Coils ..... 38
2.2.3.2 Magnet Insulation ..... 41
2.2.4 Temperature Influence on NMR Detection ..... 42
2.2.4.1 Temperature Drift Performance of Insulated Magnet ..... 43
2.2.4.2 Comparison to Non Insulated and Temperature Compensated Magnets ..... 45
2.2.5 Nutation Curve – Pulse Width Determination ..... 47
2.2.6 Sensitivity and Resolution in $^{1}H$ and $^{19}F$ NMR ..... 48
2.2.6.1 $^{19}F$ NMR Results ..... 49
2.2.6.2 $^{1}H$ NMR Results ..... 50
2.2.6.3 NMR Peak Shape ..... 53
**2.3 FLOW CELL CAPILLARY** ..... **54**
2.3.1 Chemical HF Etching Technique ..... 55
2.3.1.1 Experimental Setup ..... 55
2.3.1.2 Characteristics of the Flow Cell ..... 56
2.3.2 Mechanical Gluing Technique ..... 57
2.3.2.1 Experimental Setup ..... 58
2.3.2.2 Characteristics of the Flow Cell ..... 58
2.3.2.3 Migration Characterization of Glued Flow Cell Capillary ..... 59
2.3.3 NMR and CE Performance of Glued Flow Cell Capillary ..... 61
2.3.3.1 NMR Performance of Flow Cell Capillary ..... 61
2.3.3.2 CE Performance of Flow Cell Capillary ..... 63

**3 INTEGRATED PORTABLE CE-NMR SYSTEM ..... 66**

**3.1 COMMERCIAL CE COUPLED TO PORTABLE MICROCOIL NMR ..... 66**
3.1.1 Declaration of my Contribution ..... 66
3.1.2 Abstract ..... 66
**3.2 PORTABLE CE-NMR SYSTEM ..... 67**
3.2.1 Portable CE-NMR Instrument Setup ..... 67
3.2.2 CE Current Effects on NMR Performance ..... 68
3.2.3 Continuous On-line CE-NMR ..... 71
**3.3 FURTHER APPLICATIONS ..... 75**

**4 SUMMARY AND OUTLOOK ..... 77**

**5 REFERENCES ..... 82**

**6 APPENDIX ..... 89**

**6.1 PUBLICATION LIST ..... 89**
**6.2 CURRICULUM VITAE ..... 90**

**7 ERKLÄRUNG ZUR DISSERTATION ..... 91**

# List of Symbols and Abbreviations

| | |
|---|---|
| AWG | American wire gauge |
| $B_0$ | static magnetic field |
| $B_1$ | induced magnetic field by RF coil |
| $B_2$ | induced magnetic field by CE current |
| $B(a)$ | magnetic field created in the capillary at an arbitrary point |
| capLC | capillary liquid chromatography |
| CE | capillary electrophoresis |
| cITP | capillary isotachophoresis |
| $d_{\mathrm{coil}}$ | coil diameter |
| DMSO | dimethyl sulfoxide |
| DNBA | dinitrobenzoic acid |
| EEC | Electron Energy Corporation |
| EOF | electroosmotic flow |
| $\Delta f$ | line broadening in frequency domain |
| $f$ | filling factor |
| $F$ | electrophoretic flow rate |
| FC-43 | perfluorotributylamine |
| FID | free induction decay |
| FWHM | full width at half maximum |
| $\gamma$ | gyromagnetic ratio |
| $g$ | gravity factor |
| $\Delta h$ | height difference |
| $I$ | current |
| i.d. | inner diameter |
| IPA | isopropyl alcohol |
| IR | infrared |
| $\kappa$ | electrolyte conductivity |
| L | leading electrolyte |
| $L$ | capillary length |
| $L_{\mathrm{DW}}$ | capillary length to detection window |
| LOD | limit of detection |
| LVSEP | large-volume stacking using the electroosmotic flow pump |
| MIBK | methyl isobutyl ketone |
| MS | mass spectrometry |
| $\eta$ | viscosity |
| $n$ | refractive index |
| NMR | nuclear magnetic resonance |
| o.d. | outer diameter |

| | |
|---|---|
| P | arbitrary point in capillary |
| PCB | printed circuit board |
| PFA | perfluorinated carbonic acids |
| PFDA | perfluorodecanoic acid |
| PFHA | perfluoroheptanoic acid |
| PFNA | perfluorononanoic acid |
| PFOA | perfluorooctanoic acid |
| PFPA | perfluoropentanoic acid |
| PMMA | poly(methyl methacrylate) |
| $\rho$ | density |
| $r$ | capillary radius |
| $R$ | electric resistance |
| $R_{\text{total}}$ | total electric resistance |
| $R^2$ | correlation coefficients |
| RF | radio frequency |
| RMS | root mean square |
| RSD | relative standard deviation |
| RTC | reversible temperature coefficient |
| S | sample plug |
| SE | supporting electrolyte for CE |
| SMA | Sub Miniature Version A |
| $Sm_2Co_{17}$ | samarium cobalt |
| SNR | signal-to-noise ratio |
| $t_{\text{calculated}}$ | calculated injection time |
| $t_{\text{i}}$ | injection time |
| T | terminating electrolyte |
| TC | temperature compensated |
| TC 1 / TC 2 | thermocouple 1 / thermocouple 2 |
| TFA | trifluoroacetic acid |
| tITP | transient isotachophoresis |
| TRIS | tris(hydroxymethyl)aminomethane |
| $U$ | voltage |
| UV/Vis | ultraviolet/visible |
| $\mu_{\text{obs}}$ | observed electrophoretic mobility |
| $\mu_0$ | magnetic constant |
| $v$ | velocity |
| $V_{\text{i}}$ | injection volume |
| $V_{\text{observ}}$ | observable sample volume |
| $V_{\text{s}}$ | sample volume |
| $\omega_0$ | Larmor frequency |
| $W$ | heat |

# Aims and Concept

Developing a unique on-line coupled miniaturized capillary electrophoresis (CE)-nuclear magnetic resonance (NMR) instrument for CE separations and nano-volume $^{1}H$ and $^{19}F$ NMR analysis was the goal of this cutting-edge research presented in this work. Thanks go to my collaboration partners: Dr. Gregory L. Klunder and Dr. Kristl L. Adams from Lawrence Livermore National Laboratory, USA, Dr. Andrew McDowell from ABQMR, USA, and Dr. Jörg Lambert and Dr. Roland Hergenröder from ISAS-Institute for Analytical Sciences in Germany. Without the immense help and knowledge of these collaboration partners, this project would not have been manageable during the last three years. Special thanks for the funding of this research project go to the DFG (Vo 579/19-1) and the German Academic Exchange Service (DAAD) for the stays abroad.

The following research work is divided into three main chapters "Motivation and Introduction", "Hardware Development" and "Integrated Portable CE-NMR System". After a brief introduction to the custom-built CE-NMR instrument and its challenges, the three main parts of the CE-NMR device are described in detail in the second chapter, including 1) the portable CE system, 2) the miniaturized NMR instrument, and 3) the flow cell capillary as interface connection. The final integrated CE-NMR system and its applications are demonstrated in the third chapter.

The second chapter covers hardware information of the instrument construction, for CE and NMR, including detailed explanations of the key features in each system, *e.g.* the injection mechanism in the CE system and temperature effects during NMR measurements. In the CE instrument section basic concepts and method developments for CE separations of various sample mixtures and different approaches for sample preconcentration are explained. A variety of research approaches and accompanying technologies are developed to optimize the NMR system. These include two microcoil designs and three different magnet setups, the details and reasons for each approach are presented and experimental results are compared. The last section of the second chapter focuses on the flow cell capillary, the interface between the CE and the NMR instruments. Two different construction techniques are explored, chemical HF etching and mechanical gluing, and flow cell performances in the CE and the NMR system are compared.

The third chapter summarizes the results of this unique miniaturized on-line CE-NMR system using a glued flow cell capillary. The challenge and developed solution to CE current effects during on-line NMR data acquisition is described theoretically and verified experimentally. Continuous flow, on-line CE-NMR measurements are demonstrated. Further instrument applications are described, including alternate sample substances and areas of research interest for possible future developments.

# 1 Motivation and Introduction

The driving forces to develop miniaturized and portable analytical instruments for chemical, pharmaceutical, and environmental analysis are the needs for devices which can be taken out of the lab to remote locations to get quick answers for sample analysis, which are low-cost and have lower maintenance requirements, and which can be located in smaller spaces than conventional analytical instruments [1]. The small footprints of these instruments also readily allows them to be coupled with each other so that multidimensional on-line analyses can be achieved, which may include spectral, mass and stereochemically structural information of the sample as well as the separation of a complex mixture of interest. One such portable instrument is the integrated capillary electrophoresis (CE)-nuclear magnetic resonance (NMR) system (see Figure 1.1), which is the focus of this cutting-edge research work. CE-NMR has the potential of creating unique analytical solutions for a wide range of industrial, technological, and educational scientific problems [2][3][4][5].

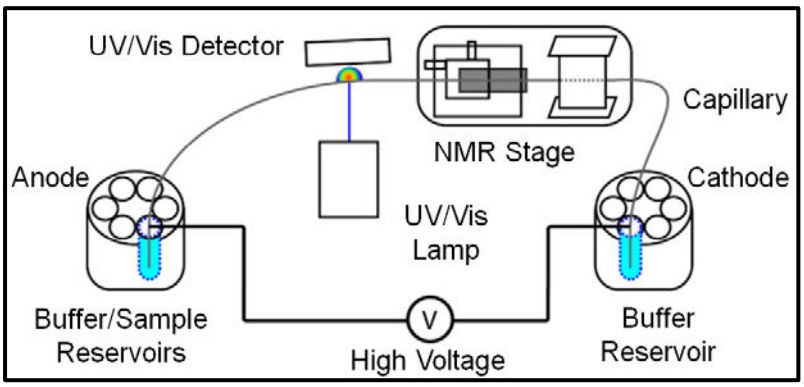


**Figure 1.1** Schematic of the custom-built, portable CE-NMR instrument

CE is a high efficiency separation system, which simplifies complex mixtures into spatially separated sample zones in narrow-bore fused-silica capillaries, typically 50-75 µm inner diameter (i.d.) and 360 µm outer diameter (o.d.), using high voltages. The sample substances are separated due to their different electrophoretic mobilities, which depend on the substance mass, charge, and spatial structure. Respectively, the migration times of the individual substances are different. A significant advantage of the CE separation technique, in contrast to liquid chromatography, is its ability to preconcentrate the sample in the CE capillary during the experiment, so that no additional off-line treatments are necessary (see Chapter 2.1.8) [6].

In addition, NMR spectroscopy is by far one of the most powerful and invaluable spectroscopic tools to acquire detailed structural and chemical specificity information on a variety of nuclei (*e.g.* $^{1}H$, $^{13}C$, $^{19}F$) in organic or inorganic molecules without destroying the samples. However, there are two significant drawbacks of this information-rich analytical technique: 1) the inherent lack of sensitivity compared to other popular spectroscopic

techniques, such as fluorescence or mass spectrometry, and 2) the fact that structure elucidation of mixtures with unknown compounds and overlapping NMR signals is difficult [7][8].

To improve the intrinsically low sensitivity of NMR a variety of different strategies have been developed over the last years. Considering these different approaches by which the sensitivity can be enhanced, it is necessary to understand the factors contributing to the signal-to-noise ratio (SNR), which is a quantitative measure for the sensitivity in NMR (see Equation 1.1):

$$SNR \propto \frac{\omega_0^2 \cdot \frac{B_1}{I} \cdot V_s}{Noise} \qquad \text{Equation 1.1}$$

The equation defines the SNR for an NMR experiment being proportional to the Larmor frequency ($\omega_0$), the magnitude of the oscillating magnetic field ($B_1$) induced by the radio frequency (RF) coil per unit of current ($I$), the sample volume ($V_s$) and reciprocally proportional to the total thermal noise produced in the receiver coil and the sample. The term $B_1/I$ defines the RF coil sensitivity, referring to the quality of the NMR probe, and is directly related to the geometry and size of the coil [9][10].
Equation 1.1 highlights the variables, which can be manipulated to help heighten the sensitivity of NMR. Traditionally and most commonly higher-strength static magnetic fields ($B_0$), which linearly increase $\omega_0$, are used. The disadvantage of this approach is the almost exponential increase in the price of the NMR instrument associated with those high-field superconducting magnets. Especially for the development of portable NMR instruments this approach is not recommended due to the enormous size of these superconducting magnets with high $B_0$ fields. Another possibility of achieving SNR improvements of factors 2-4 is the use of cryoprobes, which reduce the temperature of the probe and the preamplifiers, resulting in a decreasing thermal noise contribution to the denominator [11][12]. Even though cryoprobes are more cost effective than the usage of magnets with higher magnetic field strength, their installation and ongoing maintenance costs are still significant [13].
A further suggested strategy to help the goal of enhancing the NMR sensitivity is the use of microcoil probes with reduced RF coil diameter ($d_{\text{coil}}$) sizes. A common geometry for these microcoil probes is the solenoidal coil and the slotted microcoil is gaining popularity, too (see Chapter 2.2.2) [13]. The NMR sensitivity improvement of those microcoils increases as $d_{\text{coil}}$ is reduced (see Equation 1.2). Peck et al. [14] demonstrated that this relationship holds for microcoil diameters as low as 100 µm.

$$SNR \propto \frac{B_1}{I} \propto \frac{1}{d_{coil}} \qquad \text{Equation 1.2}$$

Increasing NMR sensitivity with decreasing $d_{\text{coil}}$ is the fundamental idea for the microcoil NMR probe technology development and essential for NMR measurements of mass-limited samples; providing that the entire sample is soluble in the small volume interrogated by the microcoil [15].

In addition to the three above-mentioned strategies for improving the SNR of the NMR experiment, the fourth idea is to increase the sample volume size and/or the concentration of the analyte in the active NMR coil volume. These aspects are important, especially for the hyphenation of NMR with CE and can be illustrated as a balancing act between the NMR sensitivity and the CE resolution (see Figure 1.2).

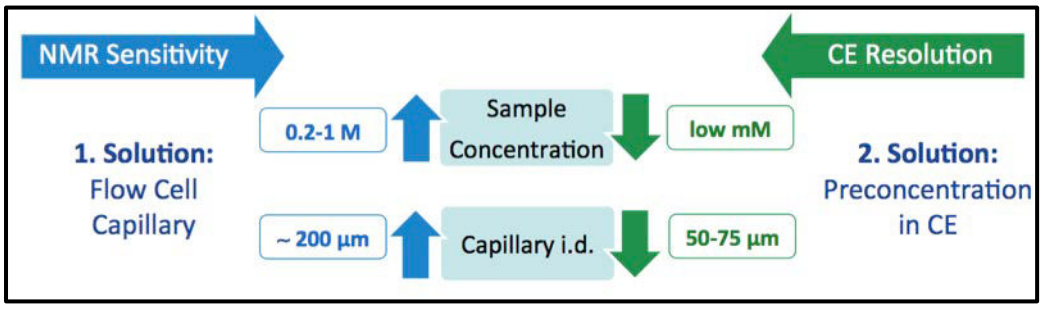


**Figure 1.2** Balancing act between NMR sensitivity and CE resolution in a CE-NMR instrument

Regarding the sample size, hence the capillary i.d., two different approaches can be used. The simplest method to increase the NMR sample volume is the use of larger i.d. sample capillaries (*e.g.* 200 µm i.d. [16]) which are inserted in the microcoil. However, this method is not recommended for coupled CE-NMR systems, which need small i.d. (50-75 µm) sample capillaries for an efficient CE separation. To increase the sample volume in this hyphenated technique, a flow cell can be etched or glued into the capillary to fill the active volume of the NMR coil more effectively by maintaining the overall small i.d. of the separation part of the CE capillary (see Chapter 2.3).
The other critical aspect refers to the sample concentration. Due to the relative low sensitivity of the NMR spectroscopy, as stated above, high concentrated sample substances (*e.g.* 0.7-0.8 M [18]) have to be used to acquire sufficient NMR spectra. For a typical CE separation, working in the low or sub mM-range these high sample concentrations are very challenging. One possible solution to solve this problem is the use of the unique, on-line preconcentration characteristics of the CE instrument (see Chapter 2.1.8) [17].

Besides the above stated disadvantage of the inherent lack of NMR sensitivity, the second drawback of NMR detection is the difficult structure elucidation of unknown sample mixtures and overlapping signals in NMR spectra. To reduce this signal convolution of complex samples, a chemical microseparation technique, *e.g.* CE, is often needed prior to the NMR detection. CE allows easy coupling to microcoil NMR detection due to the similar amount of sample volume needed for the NMR as well as the CE separation, and the plug flow CE profile [19]. In 1988 Johnson et al. introduced high resolution electrophoretic NMR based on pulsed field gradient Fourier Transform NMR for the first time [20]. The feasibility of the CE-NMR coupled technique in commercial, laboratory scale instruments was later demonstrated by Sweedler et al. [18][21][22] and Albert et al. [23][24] more than 15 years ago and relied on the developments of a flow-through NMR probe and solenoidal RF microcoils wound around the separation capillary. However, during those CE-NMR experiments the researchers noted

one major challenge. The electrical CE current that flowed through the buffer in the capillary during the experiment created an inhomogeneous magnetic field ($B_2$) in the NMR detector coil, degrading the spectral NMR resolution (see Figure 1.3 and Chapter 2.2.2.1) [25].

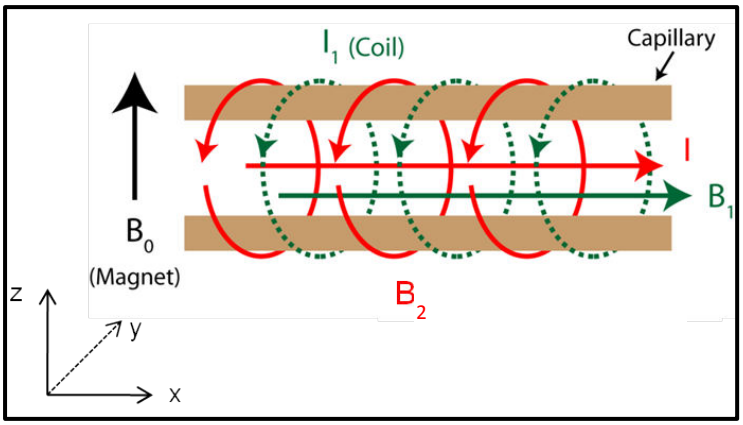


**Figure 1.3** Schematic of a CE capillary in a magnet with a perpendicular $B_0$; CE current $I$ running through the capillary, inducing the circular magnetic field $B_2$ (red) around the capillary, and the current $I_1$ running through the solenoidal coil around the capillary inducing $B_1$

Subsequent work often used saddle coils [19] or slotted microcoils [26] resonators to address this problem, normally at the expense of signal sensitivity. Continuous-flow techniques, including those with multiple flow paths through multiple NMR detectors, have also been employed to avoid having CE current flowing through the NMR coil during NMR signal detection [27].

Researchers have also taken steps to mate the much larger NMR apparatus (in particular, the magnet [28]) to the smaller CE capillary length scale. Care was taken to minimize the exposure of the NMR magnet and electronics to the high voltage applied to the CE capillary. Either a somewhat long capillary was used [29], or the entire CE capillary and electrode vials were mounted to fit into the magnet [30]. In the latter case, the CE sample injection occurred with the NMR probe out of the magnet, with subsequent insertion of the probe into the operating position. In many cases, the NMR coil was mounted directly to the CE capillary, to increase the filling factor ($f$) ($f$ = (i.d. sample tube/i.d. NMR coil)$^2$) of the NMR detection coil and thereby increase its sensitivity. This is not optimal from the CE point of view, since capillaries are somewhat fragile, prone to clogging, and difficult to clean. CE capillaries are frequently replaced in standard practice. Thus, due to several issues, the combination of CE and NMR has proven to be awkward.

Recently new developments on portable liquid state microcoil NMR [31][32][33] were published and Diekmann et al. [16] demonstrated the first coupled commercial CE instrument to a portable microcoil NMR system (see Figure 1.4 and Chapter 3.1). However, the signal-to-noise and resolution performance of that device needed improvement, due largely to the inhomogeneous magnetic field, and temperature drift of the permanent magnet's field strength. A number of improvements were required before a practical, totally

unique, miniaturized CE-NMR instrument could be built, as demonstrated in this work (see Figure 1.4).

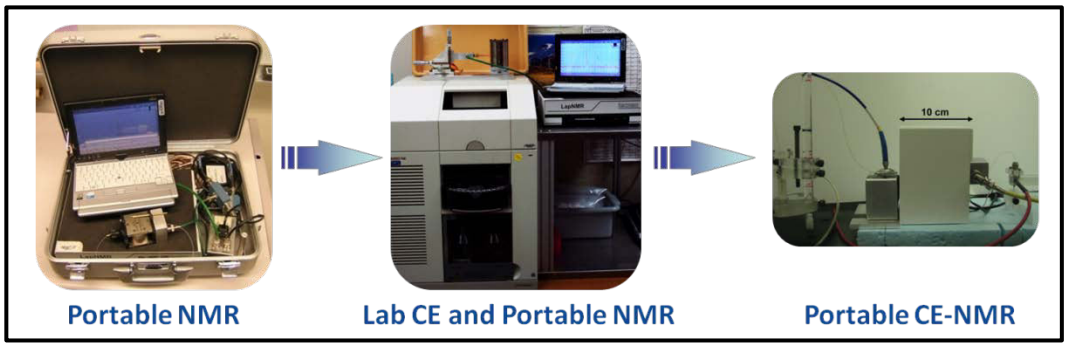


**Figure 1.4** Pictures of the instrumental development during this project: Starting with the portable NMR [31], developing the hyphenated commercial CE-portable NMR system [16], and presenting the fully integrated portable CE-NMR instrument in this research work

The hyphenated analytical technique presented in this current work demonstrates the second generation of small footprint CE-NMR coupled devices, using a miniaturized microcoil NMR system for the on-line detection and structure elucidation [33] and a custom-built portable CE system for simple rapid chemical separation and preconcentration. The new CE-NMR setup includes an improved 1.6 T magnet system with first and second order shim coils for field homogeneity and better thermal stabilization, homemade flow cell capillaries that provide a larger observable volume in the NMR coil while leaving the CE separation capillary at typical sizes (75 µm i.d.), and a new probe design. In addition, the CE current effects on the NMR resolution can be understood quantitatively and corrected through the use of the shim coils, removing the barrier for simultaneous CE and NMR operation. The small size of the device allows both the CE and the NMR to be operated in a conventional manner, with no difficulty posed by the high voltage. Resolution and sensitivity measurements are performed with weak carbonic and perfluorinated organic acids looking at $^{1}H$ and $^{19}F$ NMR, as well as continuous flow CE-NMR detections and preconcentration measurements on the CE system.

# 2 Hardware Development

## 2.1 Portable CE

The following chapter presents the hardware development of the portable CE instrument used for the integration with the miniaturized microcoil NMR system (see Chapter 2.2). The individual sections cover hardware information for the instrument construction, including detailed explanations of the key features in the CE system, *e.g.* the data acquisition and analysis, the injection mechanism, and basic concepts and method developments for various CE separations of diverse sample mixtures. Furthermore, different approaches for sample preconcentration are explained. In the last section of this chapter, CE separations on the custom-built CE instrument are demonstrated.

### 2.1.1 Instrument Setup

The portable, custom-built CE instrument had a footprint of 30 x 30 x 20 cm. The CE basic parts included (see Figure 2.1): a low pressure ultraviolet/visible (UV/Vis) Hg(Ar) light source (6035, Oriel Instruments, Irvine, CA, USA) connected to a fiber optic (QP450-1-XSR, Ocean Optics, Dunedin, FL, USA), a hand-held USB2000+ UV/Vis spectrometer (Ocean Optics, Dunedin, FL, USA), CE inlet and outlet vial holders with variable heights for buffer and sample vials, two ring Pt-electrodes (G7100-60007, Agilent Technologies, Santa Clara, CA, USA), a high voltage power supply (CZE2000, Spellman, Hauppauge, NY, USA), a syringe assembly to flush the capillary when necessary, and two PC ventilators to cool the capillary and the lamp region. SpectraSuite spectrometer operating software (Rev. 2.0.154) was used for CE data collection and processing. The uncoated fused-silica CE separation capillaries (Polymicro Technologies Inc., Phoenix, AZ, USA) had a 75 µm i.d. (360 µm o.d.) and a 5 mm long detection window at 38 cm (total length = 65 cm).

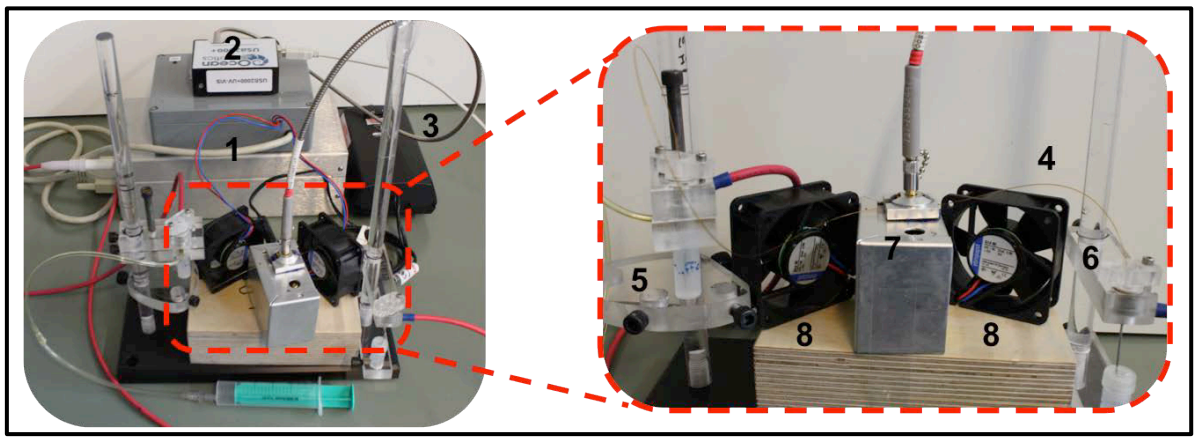


**Figure 2.1** Portable CE instrument: 1) high voltage power supply, 2) UV/Vis spectrometer, 3) UV/Vis light source power supply, 4) CE separation capillary, 5) CE inlet vial with high voltage cable and Pt-electrode, 6) CE outlet vial with ground and Pt-electrode, 7) UV/Vis light source with optical fiber, and 8) PC ventilators

The vial holders were assembled on a 10 x 25 x 2 cm rigid plastic base with two 30 cm long poly(methyl methacrylate) (PMMA) supports (o.d. 1.2 cm) on each side. The two vial holders, also PMMA, were positioned on the supports with a screw, to enable height adjustments. During CE separations, the inlet and outlet vial were leveled to equal height. An aluminum box (4 x 5 x 7 cm) was used to contain the light source and the capillary alignment interface which was connected to the UV/Vis fiber optic cable with a Sub Miniature Version A (SMA) connector. The interface focused the UV/Vis light in the optical fiber after traveling through the capillary and the aluminum box decreased stray light effects.
The experimental parameters of the portable CE instrument are summarized in Table 2.1.

**Table 2.1** Characteristic experimental parameters for the portable CE instrument

| | |
|---|---|
| Voltage | 0 to ± 30 kV |
| Current | 0-300 µA |
| UV/Vis detection | 200-850 nm (variable filter) |
| Emission line of light source | 254 nm |
| Optical fiber | 1 m long and 450 µm i.d. |
| Capillary interface alignment slit | 75 µm i.d. |
| Injection mode | hydrodynamic |
| Vials | 1 or 2 mL (polypropylene or glass) |
| Pressure flow | 20 mL syringe |

Specific instrument parameters and setups for different experiments are explained and discussed in the following chapters.

### 2.1.2 High Voltage Power Supply

The high voltage power supply, providing regulated direct current, was one of the limiting factors to fabricate a small footprint system. In order to specifically meet the needs for the research demonstrated in this work, the high voltage power supply CZE2000 (Spellman, Hauppauge, NY, USA) was not chosen because of its size (9 x 13 x 25 cm) and weight (2.8 kg), since smaller high voltage power supplies with less control and voltage range are available; but for the ability to quickly reverse the output polarity via software control. Furthermore, the high voltage power supply has fully adjustable voltage/current outputs referenced to ground via remote software control [34].
To operate the high voltage power supply remotely from the computer the Electromechanical Shop at the Leibniz University Hanover manufactured an electronic interface box (Meilhaus Electronic GmbH, Puchheim, Germany) with USB connection (see Figure 2.2). This control interface unit was connected to the high voltage power supply by the 25 pin male D connector and required a 24 V power supply. The interface was controlled by the Meilhaus Electronics RedLab software (Rev. 3.0) which enabled the operator to switch the voltage polarity, as well as set and monitor the current/voltage during an experiment, by sending

remote current/voltage values to the high voltage supply, which then gave responds about the actual current/voltage output values. All data was stored in .TXT files, for easy data processing.

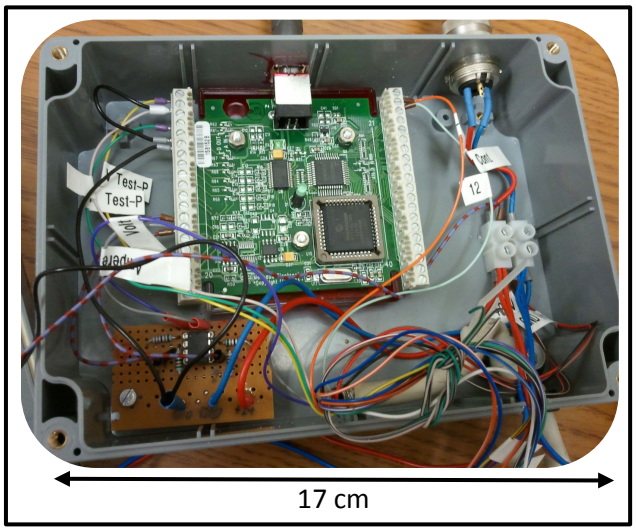


**Figure 2.2** Inside of the control box which operates the high voltage power supply

### 2.1.3 UV/Vis Detection

The most routinely used on-capillary detection methods in CE are UV/Vis absorption and fluorescence spectroscopy, which detect the presence of an analyte with different absorption or fluorescence characteristics than the buffer solution. The Lambert-Beer law is used to quantify the absorption measurements based on the linear relationship between the sample concentration and the absorbance [6][35]. Due to the wider range of detectable samples, UV/Vis spectroscopy was used in this portable CE setup. The following chapter describes methods for UV/Vis data post-processing using smoothing algorithms, and compares different spectrometer hardware setups with each other as well as to a commercial CE UV/Vis spectrometer.

#### 2.1.3.1 Smoothing Algorithms

To detect sample signals of the individual substances with the UV/Vis spectrometer during CE separations the baseline, which is random noise caused *e.g.* by stray light or electrical power fluctuations, and the appropriate signal peak have to be distinguished from each other. These random errors of unpredictable variations in the measurements from run to run are acquired even with sophisticated modern instruments. Different smoothing algorithms are commonly used to reduce this random noise in spectral measurements during post-processing data analysis. In smoothing, the data points of a signal are modified and manipulated so that individual points that are higher than the immediately adjacent points, presumably because of noise, are reduced, and points that are lower than the adjacent points are increased, leading to a smoother signal [36].

In the following comparison (see Figure 2.3) three algorithms with different parameters were used with the USB2000 UV/Vis spectrometer: 1) Moving Averages, 2) Savitzky-Golay, and 3) Median / Spike Elimination.

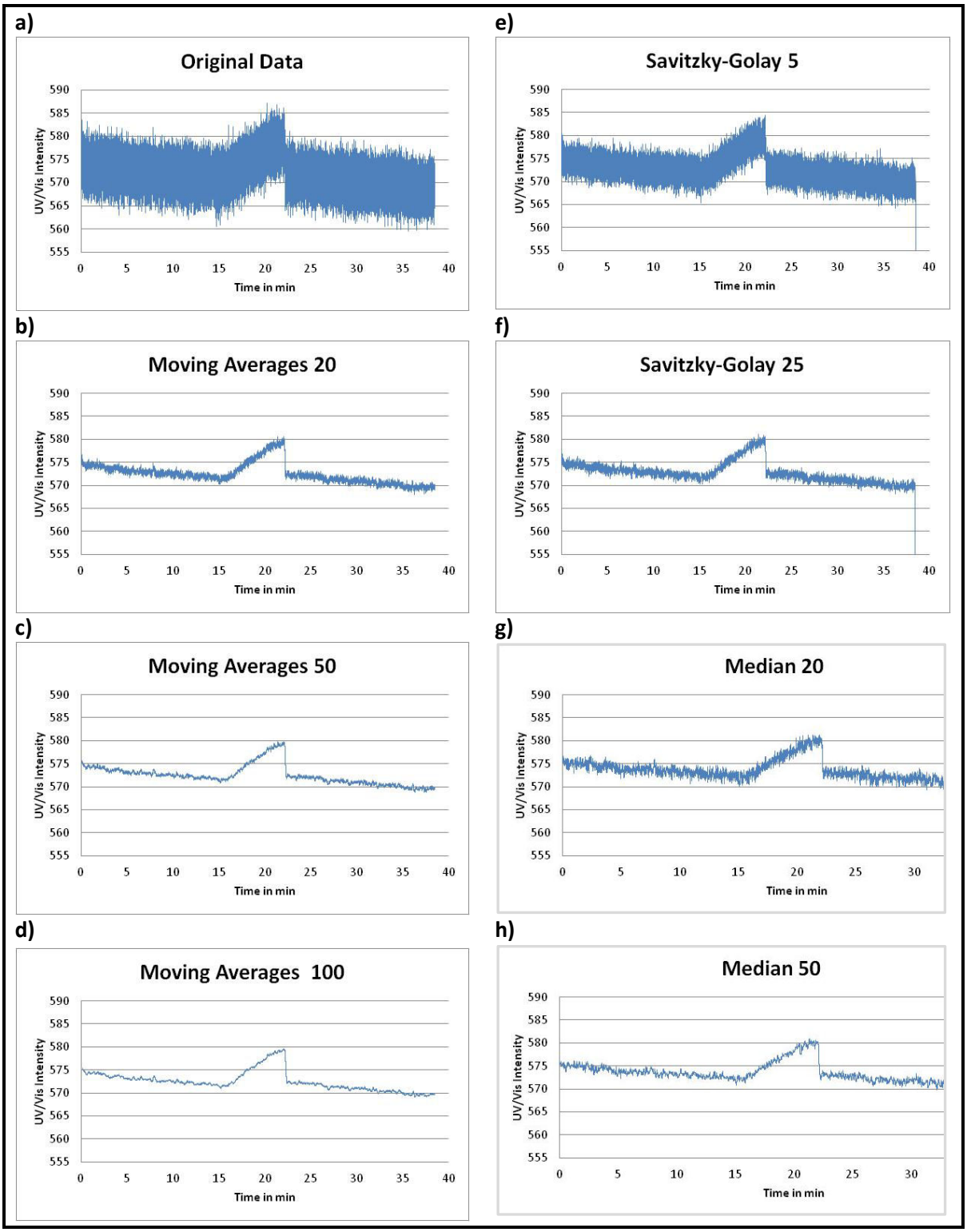


**Figure 2.3** Electropherograms measured with the USB2000 UV/Vis spectrometer of 0.25 M TFA showing **a)** the original data, **b-d)** using Moving Averages smoothing algorithm with 20, 50, and 100 averages, **e-f)** using Savitzky-Golay smoothing algorithm with 5th and 25th degree polynomials, and **g-h)** using Median / Spike Elimination smoothing algorithms with a median of 20 and 50

Figure 2.3 a shows the original data which is very noisy and the signal peak is obscured. The electropherograms using the simplest Moving Average smoothing algorithm, which replaces data points with the average of a number adjacent points, *e.g.* 20, 50 and 100, improves the spectral data significantly. It is important that the post-processing smoothing filters do not significantly alter the line shape, including the peak height and width. Therefore, larger amounts of points are not used, so that the peak width is not manipulated. The Savitzky-Golay smooth algorithm averages the points in a data set, after multiplying each point by a weighting factor, which are derived from polynomials, giving the most emphasize to the center point of the data set. Even though this smoothing filter was originally developed for spectroscopy, the improvements achieved with the simple averaging method are more significant and much less time consuming. The Median / Spike Elimination smoothing filter is used to eliminate outliers, such that every point is replaced by its median rather than the average. By comparing the electropherograms of "Median 20" and "Moving Averages 20" as well as "Median 50" and "Moving Averages 50" it can be seen that the Moving Averages algorithm is much more efficient than the Median / Spike Elimination.

To compare these results of the different smoothing algorithms more quantitatively, the quality of the signal, expressed as the SNR, which is the ratio of the signal height to the standard deviation of the noise, can be used [36]. Figure 2.4 shows the calculated SNR values of the trifluoroacetic acid (TFA) signal peak presented in Figure 2.3 for each smoothing algorithm.

**Figure 2.4** Calculated SNR values of the TFA peak (see Figure 2.3) with the different applied smoothing algorithms using the same time interval for the baseline noise determination and the corresponding peak height (S.-Go. = Savitzky-Golay, M. Av. = Moving Averages)

It is noticeable that the SNR increases with more data points used for each smoothing, regardless of the type of algorithm. The "Moving Averages 50 and 100" achieve a 8 to 9 times increase of the SNR compared to the original data and significantly reduce the noise in the measurement. Therefore, "Moving Averages 100" was used for post-processing data analysis.

### 2.1.3.2 Comparison of Portable Spectrometers

An important consideration during the development of a portable CE system is power consumption, since the system is intended to be battery operated. Two different UV/Vis spectrometers from Ocean Optics with varying detectors and power consumptions were tested (see Table 2.2).

**Table 2.2** Spectroscopic and electronic features of the two Ocean Optics UV/Vis spectrometers

| Parameter | USB2000 | USB2000+ |
|---|---|---|
| Detector | Sony ILX511A | Sony ILX511B |
| Power consumption | 90 mA @ 5 V DC | 250 mA @ 5 V DC |

Due to the almost three times lower energy consumption, the USB2000 spectrometer was tested first. As can be seen in the electropherogram in Figure 2.5 a, the resulting electropherogram of the different substances (NaOH, water , and phthalic acid) is very noisy, resulting in a SNR of 12 for the NaOH signal. Using the USB2000+ spectrometer with the same acquisition parameters and substances a much smoother spectrum with an SNR of 65 for the NaOH signal was acquired (see Figure 2.5 b).

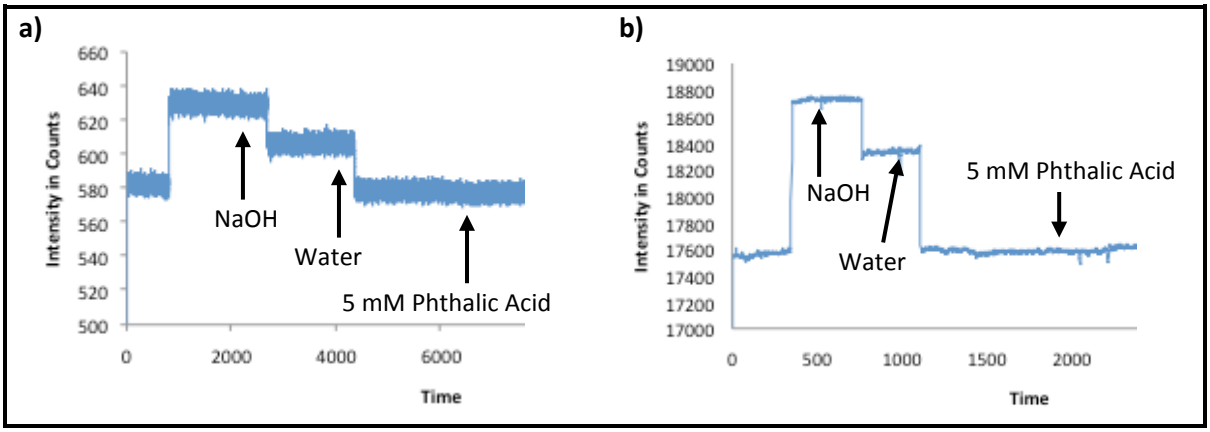


**Figure 2.5** Electropherograms of different sample analytes acquired with **a)** the USB2000 (SNR = 12) and **b)** the USB2000+ (SNR = 65) spectrometer from Ocean Optics

These two electropherograms show that with the USB2000+ spectrometer, which has the Sony ILX511B detector, a 5 times higher SNR was acquired, resulting in more sensitive spectra. In addition, the USB2000+ spectrometer is just one year old, compared to the eight years old USB2000 spectrometer. The older USB2000 device might have dust contaminations on the entrance slit, the optical filters, or the collimating and focusing mirrors in the spectrometer. These dust contaminations can reduce the light intensity and add excess noise to the spectrum, resulting in less sensitive spectra.

The results show, that with the new USB2000+ spectrometer data post-processing methods, *e.g.* Moving Averages, do not have to be applied during further experiments, presented in this research work.

#### 2.1.3.3 Comparison of Portable CE and Lab-Scale CE Spectrometers

During the process of validating the UV/Vis spectrometer in the portable system (portable UV/Vis), an important experiment was the comparison to the UV/Vis spectrometer in a commercial, lab-scale CE system (commercial UV/Vis). Therefore, the portable UV/Vis spectrometer (USB2000) was inserted in-line with a fully automated commercial CE instrument and spectrometer (see Figure 2.6). This lab-scale instrument consisted of an automated HP$^{3D}$CE (Agilent Technologies, Santa Clara, CA, USA) capillary electrophoresis unit equipped with a built-in photodiode array UV/Vis detector (200 to 280 nm), an automatic pressure and electrokinetic sample injector, an autosampler, an air-cooled capillary cartridge and a 30 kV high-voltage supply. The CE separation of the 50 mM TFA and 50 mM perfluoropentanoic acid (PFPA) sample mixture, with a 5 mM phthalic acid buffer (pH 4.3) was run in a 70 cm long capillary (i.d./o.d. = 75/360 µm). The portable UV/Vis USB2000 spectrometer was integrated in the lab-scale system and the detection window was located 30 cm behind the sample inlet (see Figure 2.6).

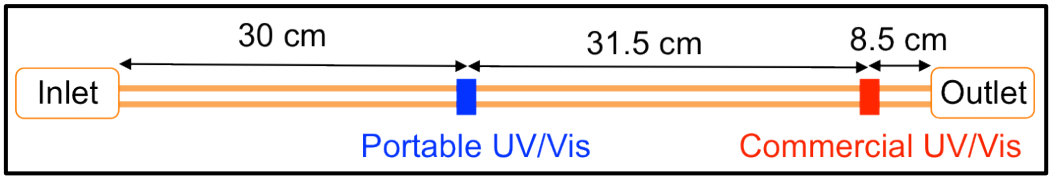


**Figure 2.6:** Schematic setup of the CE separation capillary with the integrated portable UV/Vis spectrometer and the lab-scale CE system with the commercial UV/Vis spectrometer

The CE separation of the two chemicals was monitored using both UV/Vis detectors simultaneously, acquiring data from the same run (see Figure 2.7). The portable UV/Vis spectrometer obtained the data in intensity counts, whereas the commercial UV/Vis spectrometer obtained absorbance data.

Due to the molar absorptivity of the phthalic acid buffer at the detection wavelength, less light was absorbed when the two sample substances passed the detection window, such as higher intensity counts were detected and positive peaks were visible in the portable UV/Vis spectrometer. The commercial UV/Vis spectrometer showed a reverse behavior. Therefore, less absorption was seen as the fluorinated substances were detected, resulting in negative peaks.

Both electropherograms show comparable results of the individual peaks and the characteristic asymmetric shapes. The TFA peaks show strong frontings, whereas the PFPA peaks show strong tailing effects. These peak asymmetries can be explained due to the higher (fronting) or lower (tailing) electrophoretic mobilities of the sample substances, in comparison to the bulk electroosmotic flow (EOF) of the separation buffer solution. These differences are caused by the high sample concentrations (50 mM) in comparison to the low buffer concentration of 5 mM, resulting in significant differences in the electric field strength between the substances and the buffer. Those major dissimilarities in concentrations lead to electrodispersion causing fronting and tailing effects and not a Gaussian peak shape. PFPA has a lower mobility than the buffer, resulting in a lower conductivity and therefore higher

electrical field strength. The first part of the peak is sharp, whereas the second part of the peak starts tailing because once the PFPA ions diffuse into the buffer they are slowed down by the lower electrical field strength [6][37]. The visible baseline increase in the commercial UV/Vis spectrum starting at around 30 min is due to a pH change in the outlet buffer vial, caused by the highly concentrated TFA sample reaching the outlet vial at this time.

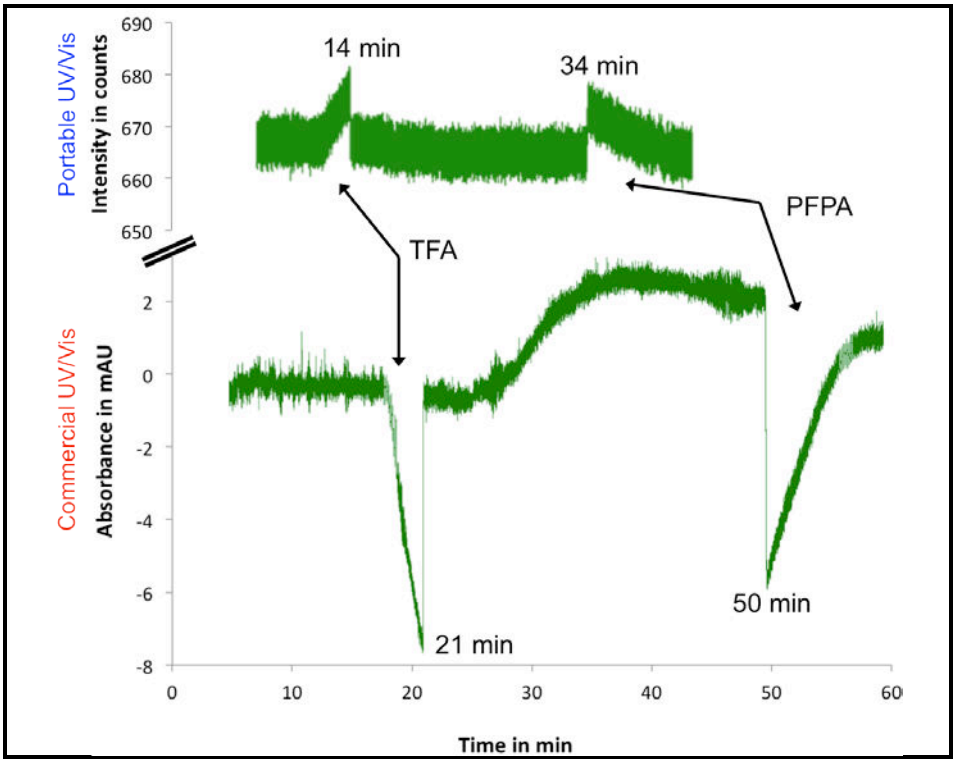


**Figure 2.7:** Electropherograms of a CE separation taken consecutively with the portable (USB2000) and the commercial UV/Vis spectrometer for the same run (sample mixture: 50 mM TFA and 50 mM PFPA), 5 mM phthalic acid buffer (pH 4.3), 70 cm long capillary, i.d./o.d. = 75/360 µm, 20 s injection with 40 mbar (4000 Pa), -25 kV, 254 nm, no smoothing algorithms)

In addition, the peak widths of the two acquired TFA and PFPA signals were compared, to identify potential diffusion effects during the CE separation. The peak widths were on a scale of 3 to 5 minutes and no significant increase was noticeable between the beginning of the separation at 30 cm and at the end of the run at 61.5 cm. For further data analysis the same run as shown in Figure 2.7 was reproduced five times (electropherograms not shown) but using a slightly lower separation voltage of -15 kV. Table 2.3 summarizes the calculated individual velocities ($v$) and the observed electrophoretic mobilities ($\mu_{obs}$) of both substances in the capillary at each detection window.

The calculated $\mu_{obs}$ were similar between the two runs at -15 kV and -25 kV, which is expected as electrophoretic mobility is substance dependent and should not be effected by the experimental parameters. It was noticeable that during all runs the velocities measured at the portable UV/Vis detection window were a factor 1.3 to 1.4 lower than those calculated for the commercial UV/Vis detection window, regardless of the applied voltage. This means the substance appears to get faster throughout the run. During the injection process, 89 nL of

sample were injected which took up a length of about 2 cm of the capillary. Therefore, during the first cm of the run, the sample seems to have a slower velocity because the substance zones have to be formed and all sample components have a uniform field.

**Table 2.3** Calculated $v$ and $\mu_{obs}$ of the individual substance peaks when passing the portable and the commercial UV/Vis spectrometer (capillary length = 70 cm)

| Substance | UV/Vis Spectrometer | $v$ in cm/min (single run, -25 kV) | $\mu_{obs}$ in $10^{-3}$ cm²/V min | $v$ in cm/min (average n = 5, -15 kV) | $\mu_{obs}$ in $10^{-3}$ cm²/V min |
|---|---|---|---|---|---|
| TFA | Portable | 2.1 | 5.88 | 1.3 ± 0.1 | 6.07 |
| | Commercial | 2.9 (x 1.4) | 8.12 | 1.7 ± 0.1 (x 1.3) | 7.93 |
| PFPA | Portable | 0.9 | 2.52 | 0.6 ± 0.1 | 2.80 |
| | Commercial | 1.2 (x 1.3) | 3.36 | 1.0 ± 0.1 (x 1.4) | 3.67 |

These experiments prove the equality of the portable UV/Vis spectrometer in the custom-built CE system to the commercial CE spectrometer, such that the portable CE instrument can be used for further experiments in the following sections. For a complete evaluation of the two UV/Vis spectrometers the limit of detection (LOD) values should be considered. However, due to the hyphenation of the portable CE instrument to the NMR system which requires high concentrations of the sample substances, these LOD measurements are not needed at this time.

### 2.1.4 Injection Technique

One of the characteristics during CE experiments is the use of small sample volumes in the nL-range. Three accepted methods are established to accomplish accurate and reproducible sample introduction into the separation capillary: 1) siphoning (gravity effect), 2) hydrostatically (pressurizing the inlet sample vial or applying vacuum to the outlet vial), and 3) electrokinetically (low voltage is applied across the capillary). The latter injection technique is based on the characteristic electrophoretic mobilities of the substances and leads to a biased injection plug [38]. In this work, the siphoning technique was used to inject sample, which is a common method to use in non-commercial CE systems, because no additional equipment, *e.g.* a pump, is required and the sample solution is not biased. The inlet end of the capillary is dipped into the analyte solution and elevated relative to the outlet end, such that the sample is injected due to the gravity flow (see Figure 2.8) [39].
The total injected volume ($V_i$) can be calculated using Equation 2.1, with the sample density ($\rho$), the gravity factor ($g$), the capillary radius ($r$), the height difference ($\Delta h$), the injection time ($t_i$), the viscosity ($\eta$), and the capillary length ($L$) [40].

$$V_i = \frac{\rho \cdot g \cdot \pi \cdot r^4 \cdot \Delta h \cdot t_i}{8 \cdot \eta \cdot L} \qquad \text{Equation 2.1}$$

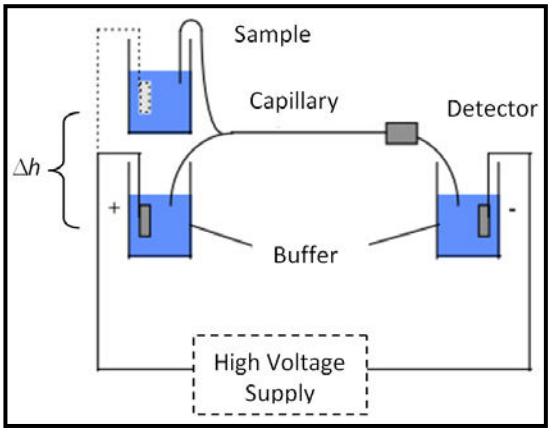


**Figure 2.8:** Schematic diagram of the siphoning injection technique in CE instruments [41]

The equation demonstrates that $V_i$ depends only on $\Delta h$ and $t_i$ (marked green in Equation 2.1) for similar samples and capillary dimensions. To demonstrate this linear behavior of the injection volume dependency on $\Delta h$ and $t_i$ in the custom-built CE system the sampling technique is validated.

#### 2.1.4.1 Validation of Siphoning Injection Technique

For reproducible CE experiments it is crucial that every injection is identical (relative standard deviation (RSD) ≤ 3 %) to each other [40]. Note, for pharmaceutical industries working with commercial CE instruments RSD values below 1 % are tolerable. However, for the CE-NMR application in this work, an RSD ≤ 3 % is acceptable, due to the large injection volumes used. Therefore, it was important to carefully validate the siphoning injection technique in the portable CE instrument, because the whole injection process was based on manual procedures. One way to control the sampling technique is to monitor break-through measurements. In doing so, the injection time is chosen to be long enough such that the UV/Vis active sample flows to the UV/Vis detection window and an absorption difference is measured with the spectrometer. Knowing the sample characteristics, the length of the capillary, and the height difference, the UV/Vis signal should always appear after comparable injection times during multiple runs with the same parameters [40].

A 5 mM phthalic acid buffer was the UV/Vis active sample and the capillary was flushed with water, which has a different spectroscopic behavior. Different injection heights (7.5 to 12.5 cm), detection window positions (capillary length to detection window ($L_{DW}$) = 20 to 25 cm), and capillary lengths (40 to 50 cm) were used to test the reproducibility of the injection technique. Table 2.4 summarizes the averaged results for the different parameter settings; each experiment was run five times [42].

The table shows that the RSD values of the individual runs are between 0.9 and 1.8 %. These results demonstrate good reproducibility of this injection technique and they compare well to literature values of less than 3 % [40]. Longer injection times (No. 2 and 4) provided the lowest RSD values, at around 1 % indicating that low injection heights requiring longer injection times are preferable.

**Table 2.4** Experimental results of the break-through measurements using different parameters, and the calculated injection times ($t_{calculated}$) for the defined injection volumes [42]

| No. | $\Delta h$ in cm | $L$ in cm | $L_{DW}$ in cm | $V_i$ in nL | $t_i$ in s | RSD of $t_i$ in % | $t_{calculated}$ in s | Deviation of $t_i$ to $t_{calculated}$ in % |
|---|---|---|---|---|---|---|---|---|
| 1 | 10 | 40 | 25 | 1104 | 514 ± 9 | 1.8 | 581 | 11.5 |
| 2 | 10 | 50 | 25 | 1104 | 645 ± 6 | 1.0 | 726 | 12.2 |
| 3 | 10 | 50 | 20 | 884 | 533 ± 9 | 1.7 | 581 | 8.3 |
| 4 | 7.5 | 50 | 20 | 884 | 737 ± 7 | 0.9 | 774 | 4.8 |
| 5 | 12.5 | 50 | 20 | 884 | 405 ± 7 | 1.8 | 464 | 12.8 |

Note, the experimental time, needed to lift and adjust the buffer vials to the correct heights for the siphoning injection technique, should be equal in all experiments, disregarding the height difference of the final setup.

Table 2.4 also compares the experimental injection times with the calculations using Equation 2.1. On average the measured injection times during the experimental runs were about 10 % lower, than the calculated values. The capillary itself could cause these variations. In the calculations an ideal capillary is assumed with an i.d. of 75 µm, however the i.d. of the capillary varies 75 ± 3 µm [43] due to the manufacturing process, resulting in varying capillary injection volumes up to 17 %. Runs No. 1, 2, and 5, deviating approximately 12 % from the calculated value, were all acquired with the same capillary and the systematic error is apparent. Runs No. 3 and 4 were monitored with two different capillaries, and other deviations were observed.

These results show that the simple siphoning injection technique is well suited for the custom-built portable CE instrument. The sample introduction into the capillary is reproducible and comparable with theoretical calculations. However, the injection has to be accomplished carefully, since this is a manual procedure.

### 2.1.5 Capillary Temperature Control

In CE, capillary cooling is an important issue, because changing temperatures affect the reproducibility of the CE separations, the migration times and lead to peak broadening. Inside the separation capillary, heat ($W$) is generated by current passing through the buffer as expressed in Equation 2.2, known as Joule heating [38].

$$W \propto \frac{I^2}{(\pi r^2)^2} \qquad \text{Equation 2.2}$$

Reducing $I$ or increasing the cross-sectional area of the capillary can achieve a decrease of the heat production [38]. However, both strategies are not desired, because less current means *e.g.* using lower voltages ($U$) or buffers with reduced ionic strengths. The square root of high voltage is proportional to the CE separation efficiency, causing the CE to be less efficient when lower voltages are used. On the other hand, increasing the capillary i.d. results in a reduction of the surface-to-volume ratio, leading to less effective heat dissipation.

Liquid cooling of the capillary is the preferred and most efficient method in terms of heat dissipation and capillary temperature control [44]. However, this method involves excessive hardware and is not feasible when the CE system is coupled to an NMR instrument, which is the goal of this research. Consequently, air cooling of the whole capillary and the lamp region is performed by using two small low power PC ventilators.

A simple method to determine the efficiency of the cooling system and the maximum voltage that can be utilized during a CE separation is the Ohm's Law Plot experiment, which was described by Nelson et al. [45]. An Ohm's Law Plot is a graph of the current vs. voltage which is dependent on the capillary i.d., the capillary length, the buffer concentration and its ionic strength, the temperature of the system and thus, the efficiency of the cooling system. Linearity in the resulting plot indicates that the capillary temperature is being adequately maintained, such that the generated Joule heating is not a disturbing factor and the system is conforming the Ohm's Law (see Equation 2.3), with the electrical resistance ($R$):

$$U = R \cdot I \qquad \text{Equation 2.3}$$

At the point where linearity is lost, the heat controlling capacity of the system has been exceeded [38]. Due to the increased temperature in the buffer solution, $R$ decreases, such that higher currents are monitored to maintain the constant voltage.

#### 2.1.5.1 Ohm's Law Plots

In this chapter, the portable CE instrument (with and without PC ventilators) and the commercial CE system are compared with each other. As stated above the custom-built CE system consisted of two PC ventilators to cool the capillary region with air. The commercial CE system was a P/ACE MDQ (Beckman Coulter, Fullerton, CA, USA) configured with a selectable-wavelength UV/VIS (200, 214, 254 and 280 nm filters) detector, an automatic pressure or electrokinetic sample injector, an autosampler, a liquid cooled capillary cartridge and a 30 kV high voltage supply. Ohm's Law Plots were generated using a 25 mM phosphate buffer (pH 2.5), a very common CE buffer solution, and identical capillary dimensions.

Figure 2.9 a compares both Ohm's Law Plots of the portable CE with the commercial CE instrument. For voltages up to 10 kV linear behaviors were acquired with both portable CE systems, resulting in comparable current values for all three setups. In the commercial system this linearity between the current and the voltage was maintained up to 25 kV, demonstrating the merits of a very efficient liquid capillary cooling system. In contrast, using the PC ventilator cooled portable CE linearity began to deviate at voltages exceeding 15 kV, and exceeding 10 kV for the portable CE system without PC ventilators, due to excess heat generation. These Ohm's Law Plots illustrate the limited applicability of the PC ventilator cooled portable CE system, using this specific buffer and these capillary dimensions.

As described earlier, buffers with less ionic strength decrease the separation current. Therefore, a 5 mM phthalic acid buffer was used with the same capillary dimensions and the Ohm's Law Plot was measured. Figure 2.9 b shows the acquired graphs of the portable CE with and without PC ventilator cooling. Because of less ionic strength in the buffer, the

resulting currents are much lower even at voltages up to 25 kV, leading to a linear current-voltage behavior on the portable CE even without ventilator cooling. Even though both experiments show a linear plot, 20 % higher currents are monitored when the PC ventilators were not turned on; meaning that more heat is generated during the non-ventilation experiment (see Equation 2.2).

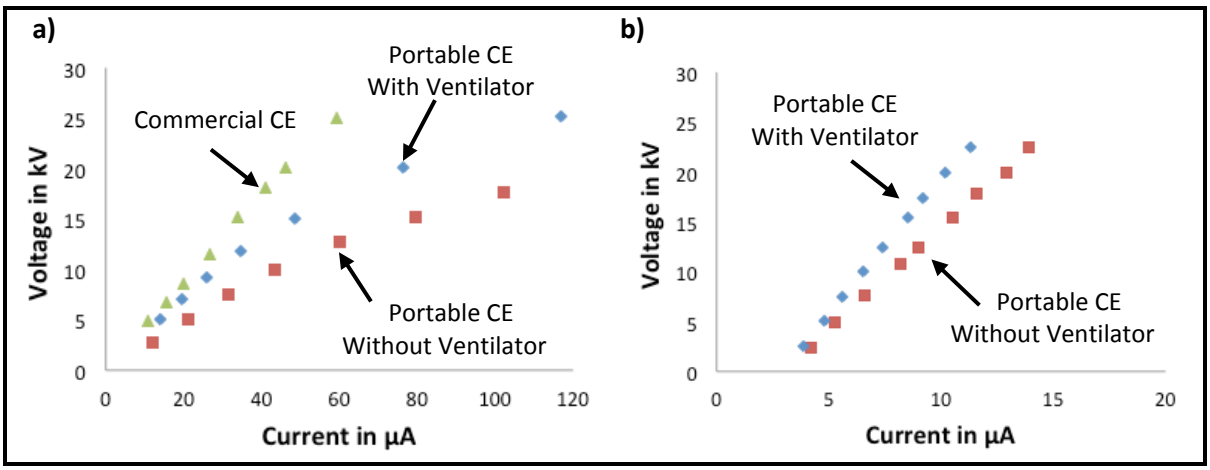


**Figure 2.9:** Ohm's Law Plots of **a)** 25 mM phosphate buffer (pH 2.5) measured in the liquid cooled commercial CE (green), the PC ventilator cooled portable CE (blue), and the portable CE without PC ventilators (red) [42] and **b)** 5 mM phthalic acid buffer (pH 4.3) measured in the portable CE system using PC ventilators (blue) and without PC ventilators (red) (56 cm long fused-silica capillary, i.d./o.d. = 75/360 µm)

These experiments show the effect of different buffer solutions and heating when working with the portable CE system, such that further experiments were carried out in the linear region of the Ohm's Law Plot. Furthermore, the results demonstrate the importance of turning on the PC ventilators when CE separations were performed.

#### 2.1.5.2 Long-Term Voltage Experiments

The previous experiments were all performed during limited time intervals of the order of a few minutes. However, CE separations might take up to 1 h (see Chapter 2.1.3.3). Therefore, this chapter demonstrates a long-term voltage and current measurement for the portable CE setup with and without PC ventilators. The same capillary as in the previous chapter was used and filled with 5 mM phthalic acid buffer. The voltage was set to -20 kV and the current was measured for 1 h (see Table 2.5).

**Table 2.5** Experimental results of the long-term voltage and current measurement for the portable CE system with and without PC ventilators using 5 mM phthalic acid buffer (56 cm long fused-silica capillary, i.d./o.d. = 75/360 µm)

| PC Ventilator | Average *U* in kV | RSD of *U* in % | Average *I* in µA | RSD of *I* in % |
|---|---|---|---|---|
| on | 20.3 | 5 | 10.4 | 3 |
| off | 20.0 | 5 | 12.8 | 4 |

These long-term experiments demonstrate that both runs were very smooth over the measured time period and the high voltage supply produced constant voltage. However, using the portable CE system without the PC ventilators 19 % higher currents and therefore more heat were produced; compare to results presented in Chapter 2.1.5.1.

### 2.1.6 CE Separation, Characterization and Quantification on Commercial CE System

In the previous chapters, the portable CE system was built and demonstrated. However, before sample separations were performed on the custom-built CE system, the different methods were developed on a commercial CE system. For these experiments the P/ACE MDQ (Beckman Coulter, Fullerton, CA, USA) was used, configured with a selectable-wavelength UV/VIS (200, 214, 254 and 280 nm filters) detector acquiring at 4 Hz, an automatic pressure or electrokinetic sample injector, an autosampler, a liquid-cooled capillary cartridge and a 30 kV high-voltage supply. The following sections illustrate two different sample mixtures (1) glycyl-glycin and TFA, as well as (2) PFPA and TFA at various concentration levels.

#### 2.1.6.1 Glycyl-Glycin and TFA Separation

The first sample mixture consisted of the amino acid peptide glycyl-glycin and TFA (see Figure 2.10). These two compounds were chosen due to their high solubility in aqueous solutions, their difference in electrophoretic mobility and their simple NMR spectra; three important requirements for the CE-NMR coupling, the goal of this research work.

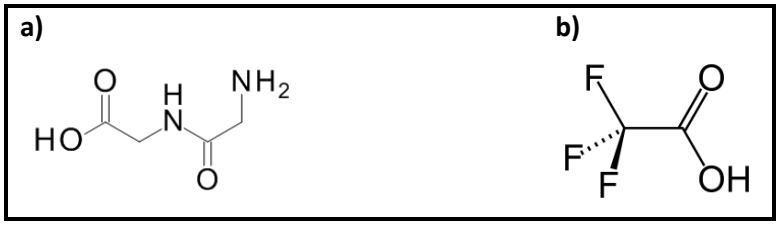


**Figure 2.10:** Structural formula of **a)** glycyl-glycin and **b)** TFA

Before the experiments were started, the CE separation was developed theoretically based on the acid dissociation constants of the two substances, such that ideal parameters for the buffer pH were calculated [42]. The electropherograms in Figure 2.11 show the optimized separation of the two compounds at relatively low concentrations (5 mM glycyl-glycin and 100 mM TFA) and at high concentrations (500 mM glycyl-glycin and 500 mM TFA).
Both runs had well resolved sample peaks with baseline resolution. However, using 500 mM sample concentration the peak shapes, especially of the glycyl-glycin peak, are unsymmetrical and do not appear Gaussian. The glycyl-glycin signal shows an 8 min wide baseline peakwidth and the maximum of the peak shows a plateau, indicating signal saturation. These results were satisfying, considering the 100-fold increase in sample concentration, compared to conventional CE experiments.

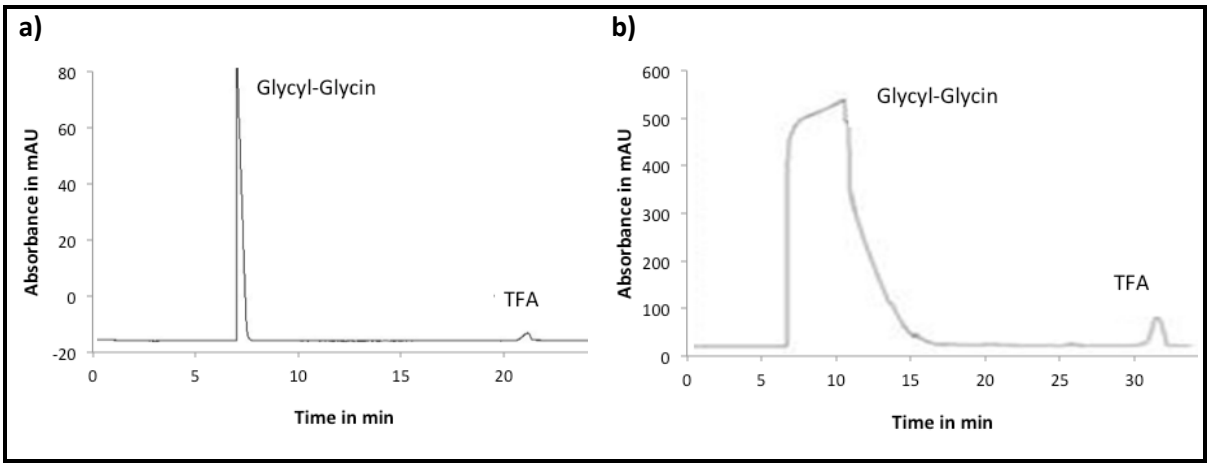


**Figure 2.11:** Electropherograms of glycyl-glycin and TFA acquired with the commercial P/ACE MDQ CE system at **a)** 5 mM glycyl-glycin and 100 mM TFA and **b)** 500 mM glycyl-glycin and 500 mM TFA (25 mM phosphate buffer (pH 2.5), 56 cm long capillary, 48 cm to detector, i.d./o.d. = 75/360 µm, 5 s injection with 34.5 mbar (3447 Pa), 20 kV, 200 nm) [42]

These CE results and the Ohm's Law Plots in Chapter 2.1.5.1 show that using this sample mixture and the phosphate buffer is not a suitable experiment for the portable CE system.

### 2.1.6.2 PFPA and TFA Separation

The other sample mixture consisted of PFPA and TFA, two fluorinated compounds, which were easily detectable with the NMR instrument (see Chapter 2.2). Before the separation was run on the lab-scale, commercial CE, the CE separation was developed theoretically based on the acid dissociation constants of the two substances, such that ideal parameters for the buffer pH were calculated [46].

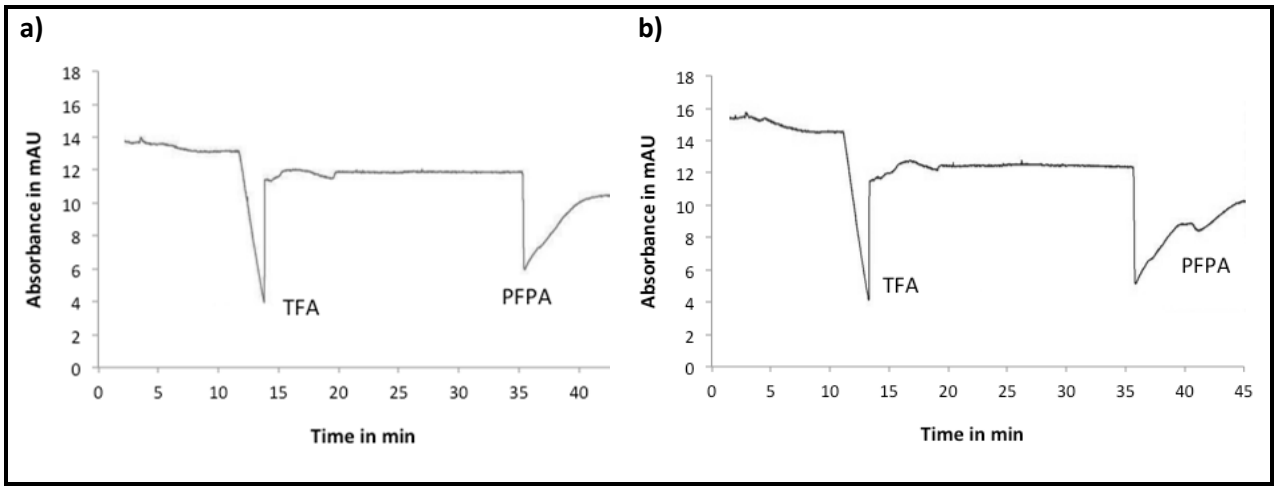


**Figure 2.12:** Electropherograms of PFPA and TFA acquired with the commercial P/ACE MDQ CE system at **a)** 100 mM PFPA and 100 mM TFA and **b)** 500 mM PFPA and 500 mM TFA (5 mM phthalic acid buffer (pH 4.3), 56 cm long capillary, 48 cm to detector, i.d./o.d. = 75/360 µm, 5 s injection with 34.5 mbar (3447 Pa), -20 kV, 254 nm) [46]

The electropherograms in Figure 2.12 show the optimized separation of the two compounds at moderate concentrations (100 mM PFPA and 100 mM TFA) and at higher concentrations (500 mM PFPA and 500 mM TFA). Even though, Figure 2.12 b shows the electropherogram of the 500 mM sample mixture, the peak areas do not seem to be 5 times larger, compared to the electropherogram of the 100 mM sample mixture. These results were due to the saturation effect caused by the high sample concentrations, such that the area increase is not linear proportional to the concentration increase (see Chapter 2.1.6.3).
During these CE experiments an indirect UV/Vis detection method was used, whereas the phthalic acid buffer had a high UV/Vis absorption at 254 nm. Therefore, PFPA and TFA appeared as negative absorption peaks in the electropherogram. The signals show comparable asymmetrical peak characteristics with fronting and tailing, as already explained in Chapter 2.1.3.3. The experiments were reproducible even at high concentrations, as demonstrated in [46], and the two substances were separated well with a time gap of about 20 min between them. A further important characteristic of these separations was the low current of 10 µA running through the system.
Due to the satisfying behavior of the PFPA and TFA sample mixture, these analytes were used in the coupled CE-NMR system and characterized more in the following chapter.

### 2.1.6.3 Quantification of High Concentrated Sample Mixtures

In the previous chapter the TFA and PFPA sample mixture was separated at different concentrations. To investigate the reproducibility of the CE separation, each sample concentration was measured three times [46]. This data was used to quantify the separation and calibrate the system. In CE two different peak parameters can be used for quantification, the height or the area of the signal, which are proportional to the concentration of the analyte. However, working with very high concentrations, as required in this research work for CE-NMR experiments, peak height and peak area can lead to different quantification results, due to asymmetric peak shapes [40]. Therefore, the peak areas of the PFPA and TFA signals of three consecutive runs at three different concentrations (100 mM, 250 mM, and 500 mM) were measured (see Table 2.6).

**Table 2.6** Averages of TFA and PFPA peak areas from three consecutive separations acquired comparable to Figure 2.12 at different concentrations [46]

| Concentration in mM | TFA peak area average in $\cdot 10^5$ | RSD of peak area in % | PFPA peak area average in $\cdot 10^5$ | RSD of peak area in % |
|---|---|---|---|---|
| 100 | 4.4 | 3.3 | 8.5 | 2.7 |
| 250 | 5.5 | 6.5 | 11.0 | 3.5 |
| 500 | 7.4 | 4.2 | 16.5 | 6.3 |

The RSD values indicate that the quantification of each separated signal was reproducible with deviations between the runs less than 7 %. High RSD values indicate the difficult analysis of very asymmetric signals. For such signals the beginning and the end of the peak

were hard to define. Using the data points from Table 2.6 linear calibration curves, without including the origin as a data point, can be achieved with correlation coefficients ($R^2$) of $R^2 > 0.99$ (see Table 2.7) [46]. Including the origin to the calibration curve would lead to a significant bend in the lower part of the calibration, due to the high absorptivity level of the baseline [86].

**Table 2.7** Parameters of the calibration using the peak areas of PFPA and TFA from Table 2.6 [46]

| Substance | Equation ($y$ = peak area) $x$ in mM | $R^2$ |
|---|---|---|
| TFA | $y = 751x + 363878$ | 0.99991 |
| PFPA | $y = 2020x + 627551$ | 0.995 |

The table indicates that linear calibration is possible when the values of the peak areas are used for quantifications, even at high concentrations up to 500 mM.

### 2.1.7 CE Separation on Portable CE System

In the previous section, separations of highly concentrated sample mixtures were demonstrated on a commercial CE system. This section shows the separation of a 250 mM TFA and 250 mM PFPA sample mixture, as optimized in Chapter 2.1.6, performed on the custom-built CE instrument.

The electropherogram in Figure 2.13 shows the characteristic peak shapes with a significant fronting and tailing of the TFA and the PFPA, respectively. A total sample volume of 70 nL was injected using the hydrodynamic siphoning technique for 50 s at a height difference of 10 cm. The separation ran at -6 µA, comparable to the above acquired currents on the commercial CE instrument. Both peaks were well separated from each other and no significant differences to the separations on the commercial CE instrument can be detected.

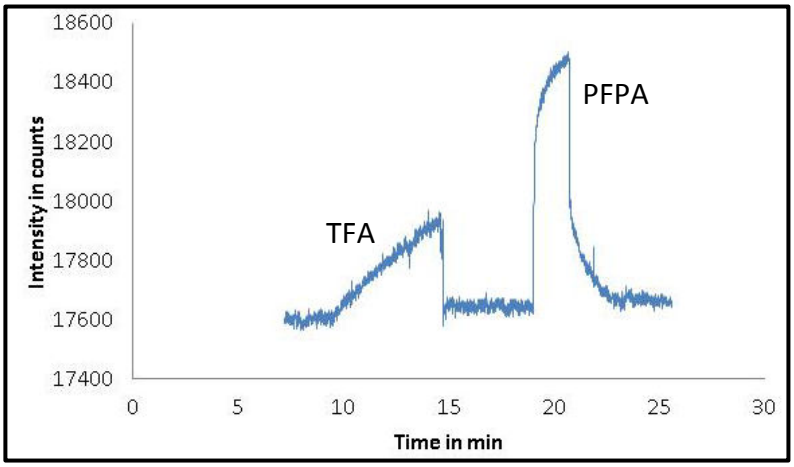


**Figure 2.13:** Electropherogram of a CE separation taken with the portable CE (sample mixture: 250 mM TFA and 250 mM PFPA, 5 mM phthalic acid buffer (pH 4.3), 55 cm long capillary, 30 cm to detector, i.d./o.d. = 75/360 µm, 70 nL injection volume, -15 kV, 254 ± 3 nm, no smoothing algorithms)

This result shows the separation capability of the portable CE instrument, which is necessary for the integration with the portable NMR detector in this research work.

### 2.1.8 Preconcentration Techniques on Commercial CE System

As already stated in the introduction, the sample concentration for a CE-NMR experiment should be around 100-500 mM in order to acquire significant NMR data, due to the low sensitivity of the NMR instrument. This chapter demonstrates the advantage of using CE in this research work instead of other liquid chromatography technologies, because of its availability of on-line sample preconcentration. Various methods are known to compress the analyte into a narrow sample zone with higher concentration prior to the NMR analysis, including transient isotachophoresis (tITP), electrostacking and large-volume stacking using the electroosmotic flow pump (LVSEP) [6][92][93].

The following two chapters show experimental results on the tITP and LVSEP preconcentration methods for five perfluorinated carbonic acids (PFA) using the commercial CE instrument (P/ACE MDQ, Beckman Coulter, Fullerton, CA, USA): 1) PFPA (C5), 2) perfluoroheptanoic acid (PFHA, C7), 3) perfluorooctanoic acid (PFOA, C8), 4) perfluorononanoic acid (PFNA, C9), and 5) perfluorodecanoic acid (PFDA, C10) (see Figure 2.14).

**1) PFPA (C5):**

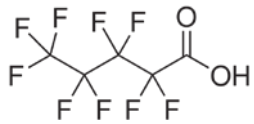

**2) PFHA (C7):**

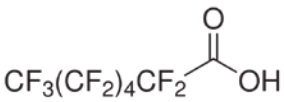


**3) PFOA (C8):**

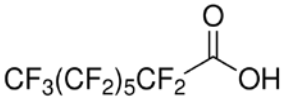


**4) PFNA (C9):**

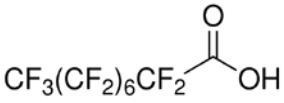


**5) PFDA (C10):**

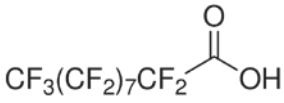


**Figure 2.14:** Structural formulas of PFAs

#### 2.1.8.1 tITP-CE Method

Conventional tITP-CE separations are achieved using a discontinuous buffer system to concentrate charged, diluted sample analytes while also effecting a separation based on differences in the electrophoretic mobilities. During those experiments the supporting electrolyte (SE) for the CE separation is filled in the capillary before the sample plug (S) is bracketed between the leading electrolyte (L), with higher mobility than the sample

components, and the terminating electrolyte (T), with lower ionic mobility. The analyte ions are sandwiched by the respective mobilities of the ions between the leading and terminating buffer, such that they are isotachophoretically concentrated and separated. In the case of higher sample analyte mobility than that of the SE, the T is not necessary, since the ions in the SE act as the T (see Mode 1 in Figure 2.15 a). Correspondingly, when the mobility of the sample ions is lower than that of the ions in the L, this electrolyte is not required (see Mode 2 in Figure 2.15 a). All these methods are applicable with samples consisting of a mobility which is above the mobility of T and below the mobility of L [6][37][47][48].

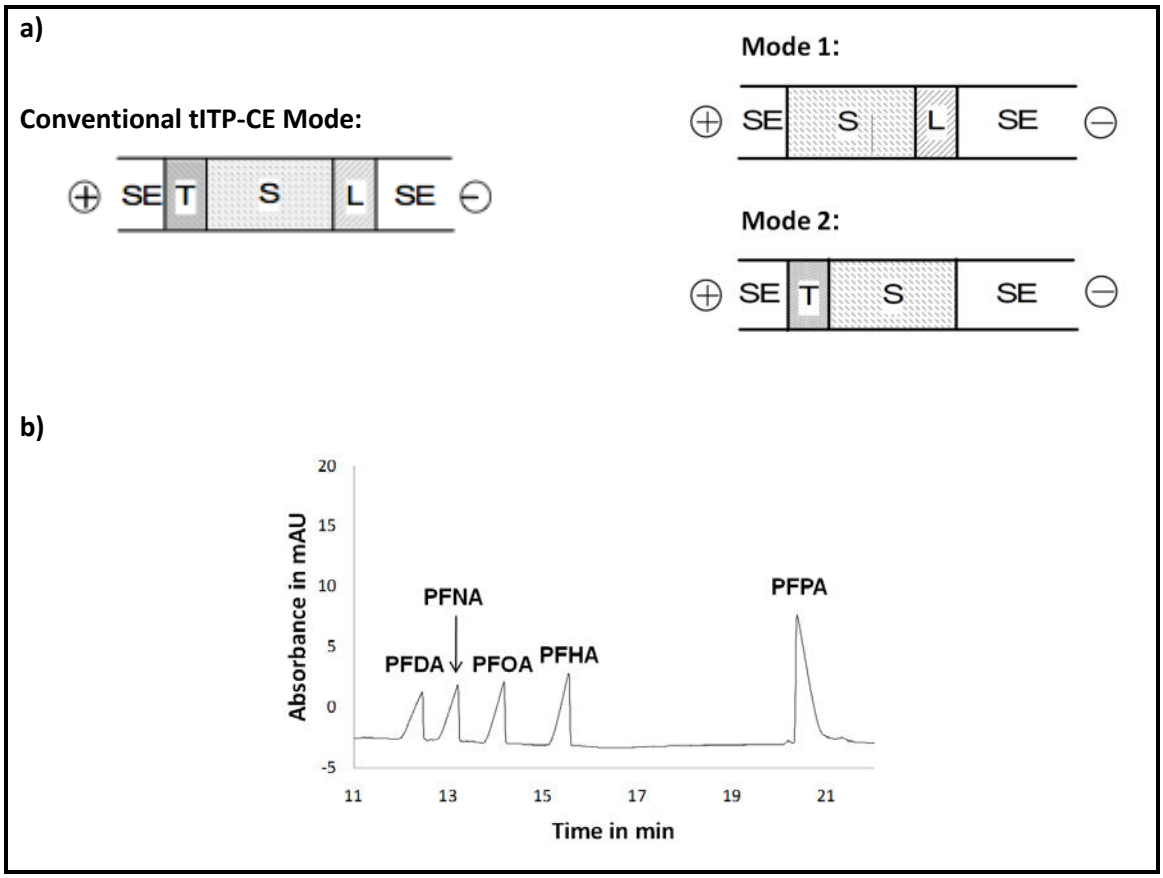


**Figure 2.15:** **a)** Schematics of the different operational modes of tITP-CE (SE = supporting electrolyte for CE, S = sample plug; L = leading electrolyte, T = terminating electrolyte) [47] and **b)** Electropherogram of a CE separation taken with the commercial P/ACE MDQ CE system (PFA sample mixture: 1 mM PFDA, 1 mM PFNA, 1 mM PFOA, 1 mM PFHA and 2 mM PFPA, 50 mM tris(hydroxymethyl)aminomethane (TRIS) buffer with 7 mM 3,5-dinitrobenzoic acid (DNBA) and 60 % methanol (pH 8), 50 cm long capillary, 42 cm to detector, i.d./o.d. = 50/360 µm, 3 s injection with 34.5 mbar (3447 Pa), 25 kV, 254 ± 3 nm)

For a successful tITP-CE experiment, the CE separation had to be optimized at first; see [49]. Figure 2.15 b shows a CE separation of the sample mixture based on [49], which contained five PFA substances on a fused-silica capillary using an indirect UV/Vis detection method. The electropherogram shows a well resolved and separated PFA sample mixture which took around 20 min. The four longer PFAs (PFHA-PFDA) show peak frontings due to higher electrophoretic mobilities compared to the EOF of the buffer. In contrast, PFPA shows peak

tailing, because of a slower electrophoretic mobility. Due to these differences in the electrophoretic mobilities of the individual sample components, the two modified versions (see Figure 2.15 a) of the above-described conventional tITP-CE mode were tested. Based on the optimized CE separation for the PFA sample mixture, the following parameters were used for the tITP-CE experiments (see Table 2.8):

**Table 2.8** Parameters for the tITP-CE experiments [49]

| | |
|---|---|
| Voltage | 25 kV |
| Injection | 34.5 mbar (3447 Pa) for 3 s |
| Wavelength | 254 ± 3 nm |
| Capillary i.d./o.d. | 50/360 µm |
| Capillary length | 40/50 cm |
| Chromophore | 7 mM 3,5-DNBA |
| Organic solvent | 60 % methanol |
| SE and L in Mode 1 | 25 mM and 50 mM TRIS (pH 8) |
| SE and T in Mode 2 | 50 mM and 30 mM TRIS (pH 8) |

The two electropherograms in Figure 2.16 show the preconcentration effects of the two different tITP-CE modes. To compare the preconcentration effects, the time corrected peak areas were used; see [49]. The experiment in Mode 1 resulted in a faster separation and the corrected peak areas were 2-8 times higher than in the normal CE separation shown in Figure 2.15 b. Similar results were achieved with Mode 2. However, due to the slower migration times of the sample components, the resolution was better than in Mode 1. However, the preconcentration effect was less efficient. The sensitivity enhancement in Mode 2 had a factor of 1.6, compared to a factor of 2-8 in Mode 1.

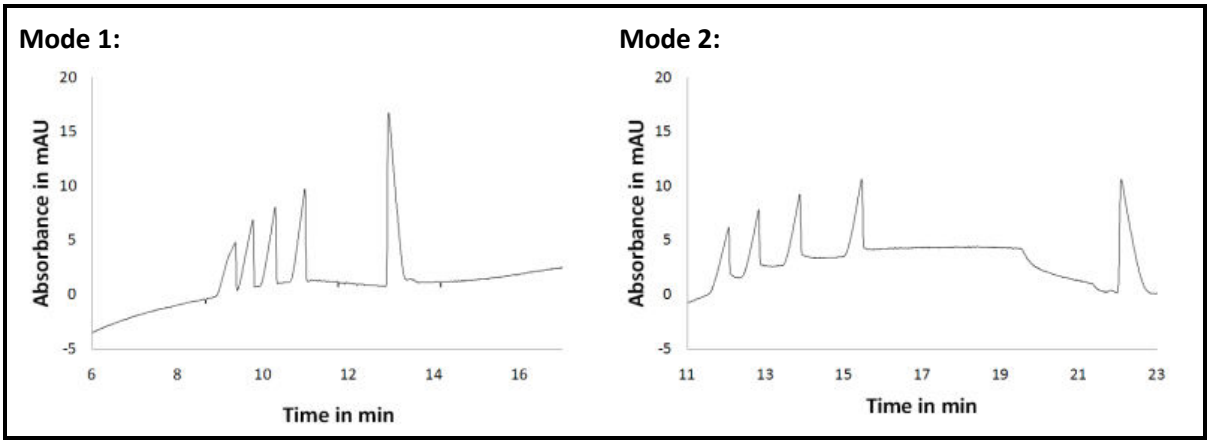


**Figure 2.16:** Electropherograms of the two Modes in tITP-CE taken with the commercial P/ACE MDQ CE system (PFA sample mixture: 1 mM PFDA, 1 mM PFNA, 1 mM PFOA, 1 mM PFHA and 2 mM PFPA) using the experimental parameters listed in Table 2.8

Comparing these first experimental attempts to other data *e.g.* [47][48], higher preconcentration effects up to 3 orders of magnitude were achieved in literature. These

results show the high capability of the tITP-CE experiment, which has to be further optimized for the above presented sample mixture.

#### 2.1.8.2 LVSEP Method

Another option for on-line sample preconcentration is the highly efficient LVSEP of weakly acidic organic compounds using methanol as the buffer solvent. During this CE experiment methanol provides appropriate suppression of the EOF in a bare fused-silica capillary and an increase in the electrophoretic mobilities of the anionic perfluorinated analytes compared to water. In 1992, Chien and Burgi [50] introduced this large-volume hydrodynamic injection which was followed by the removal of the low-conductivity sample matrix using polarity switching to enhance the CE sensitivity [51][52].

Initially, the whole capillary was flushed and filled with the sample analyte which was dissolved in methanol using the hydrodynamic injection (see (1) in Figure 2.17). Afterwards, the methanol was removed from the capillary into the inlet vial using the EOF pump while the anionic analytes were stacked under an electric field of reverse CE polarity. The applied high voltage was mainly distributed over the sample plug which had a low conductivity. The electric field in the remaining CE run buffer was very small. Therefore, the anionic sample analytes were stacked at this concentration boundary, which had been moving back to the inlet vial ((see (2) in Figure 2.17)). During this process, CE buffer of high conductivity from the outlet vial was filled in the capillary, such that the overall EOF in the capillary was further reduced due to the increased ionic strength. As soon as the EOF and the electrophoretic velocities of the sample analytes were balanced, the migration direction of the stacked analytes was switched toward the outlet vial (see (3) in Figure 2.17) [51][52].

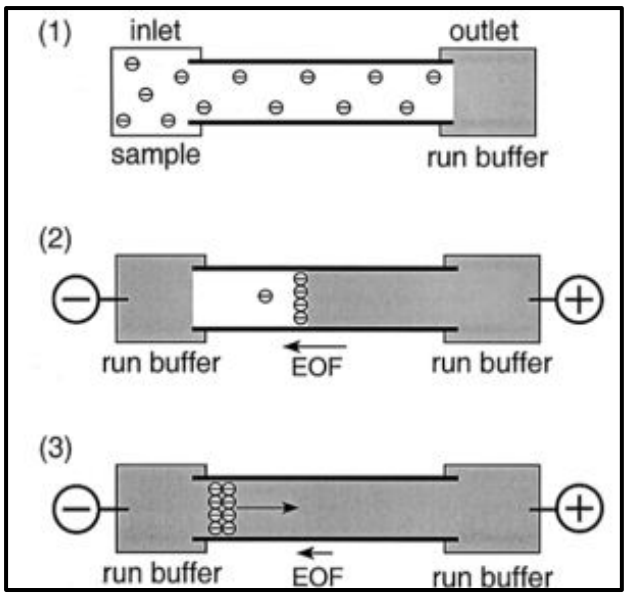


**Figure 2.17:** Schematic representation of the LVSEP mechanism: **1)** capillary filling with sample, **2)** removal of methanol during sample stacking under a reversed potential, and **3)** CE separation of stacked sample [51]

To demonstrate the preconcentration efficiency of this technique the PFA sample mixture with a concentration of 0.1 mM for each analyte was used and dimethyl sulfoxide (DMSO) was added as EOF marker. At first a conventional CE separation was monitored which took about 25 min and showed well resolved sample peaks of all five PFA substances (see Figure 2.18). Then the LVSEP method was run with a long hydrodynamic sample injection for 12 s at 900 mbar (90,000 Pa). 331 nL of perfluorinated sample were injected, resulting in a 17 cm long sample plug in the capillary. After this injection, high voltage was turned on with reverse polarity. The electropherogram in Figure 2.18 shows the LVSEP run with a roughly 100 fold sample concentration enhancement for all five PFA analytes. Even though the signal peaks are wider compered to the initial CE run, all substances are still well resolved and distinguishable.

In addition to the electropherograms, the currents were monitored during both runs. Figure 2.18 shows a constant current of -3.5 µA for the CE experiment. In contrast to that, the LVSEP method shows a significant increase of the current in the beginning. This is a characteristic behavior for this electrophoretic method, because with more and more buffer migrating into the capillary from the outlet vial, the current increases.

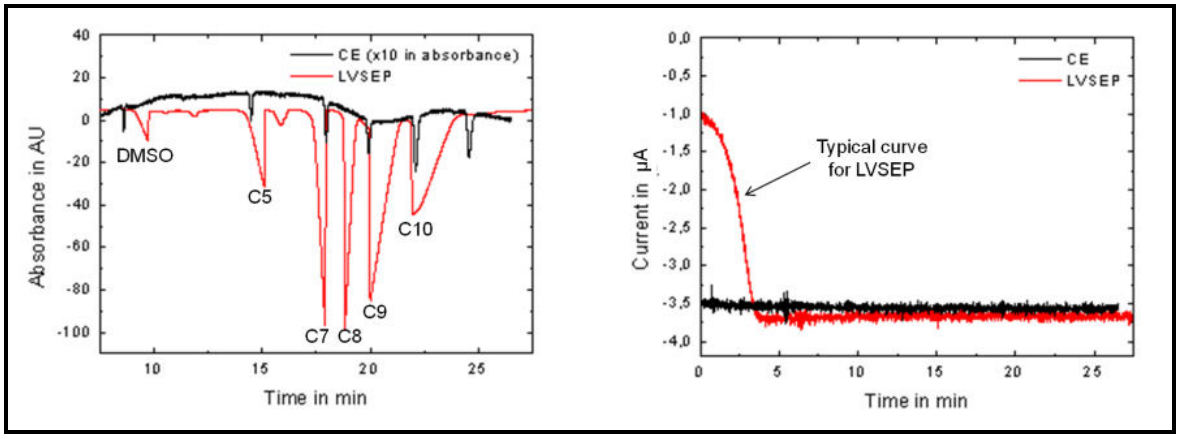


**Figure 2.18:** **Left:** Electropherograms of a CE separation (injection with 35 mbar (3447 Pa) for 3 s; 3 nL) and a LVSEP (injection with 900 mbar (90,000 Pa) for 12 s; 331 nL) taken with the commercial P/ACE MDQ CE system (PFA sample mixture: 0.1 mM PFDA, 0.1 mM PFNA, 0.1 mM PFOA, 0.1 mM PFHA, 0.1 mM PFPA, and 0.1 mM DMSO) (50 mM TRIS buffer with 7 mM 2,4-DNBA in methanol (pH 8), 50 cm long capillary, 42 cm to detector, i.d./o.d. = 50/360 µm, -25 kV, 254 ± 3 nm). **Right:** Detected currents during the CE separation and the LVSEP.

These experiments show a significant on-line sample preconcentration of approximately 2 orders of magnitude for a 0.1 mM sample mixture. For CE-NMR experiments this technique is recommended, due to its high sensitivity enhancement. Further optimization of the experimental parameters might lead to satisfying results which are transferable to CE-NMR runs.

## 2.2 Portable NMR

The following chapter presents the hardware development of the portable microcoil NMR instrument used for the integration with the custom-built CE system. The individual sections cover hardware information for the instrument construction, including the two key devices in the NMR, the magnet and the microcoil probehead, and show the basic concepts as well as method developments. To get an idea for the appropriate technologies which would perform best in the NMR system, a variety of research approaches, including two microcoil designs and three different magnet setups, are presented and compared to each other. Basic concepts and developed methods are demonstrated, emphasizing the temperature effects on the NMR experiments and the resolution and sensitivity performance of the NMR system.

### 2.2.1 Instrument Setup and Experimental Parameters

The portable microcoil NMR instrument and the operating software were developed at ABQMR (Albuquerque, NM, USA) in collaboration with Dr. Andrew McDowell [33] and included a small permanent magnet (Aster Enterprise, Inc., Acton, MA, USA) with integrated 1st and 2nd order shim coils, manual shim control electronics, a single-board NMR spectrometer (RadioProcessor™, SpinCore Technologies, Inc., Gainesville, FL, USA), a micro probehead with a hand-wound microcoil, a temperature control unit and a laptop computer (see Figure 2.19). The individual parts of this NMR instrument are explained and discussed in the sections below.

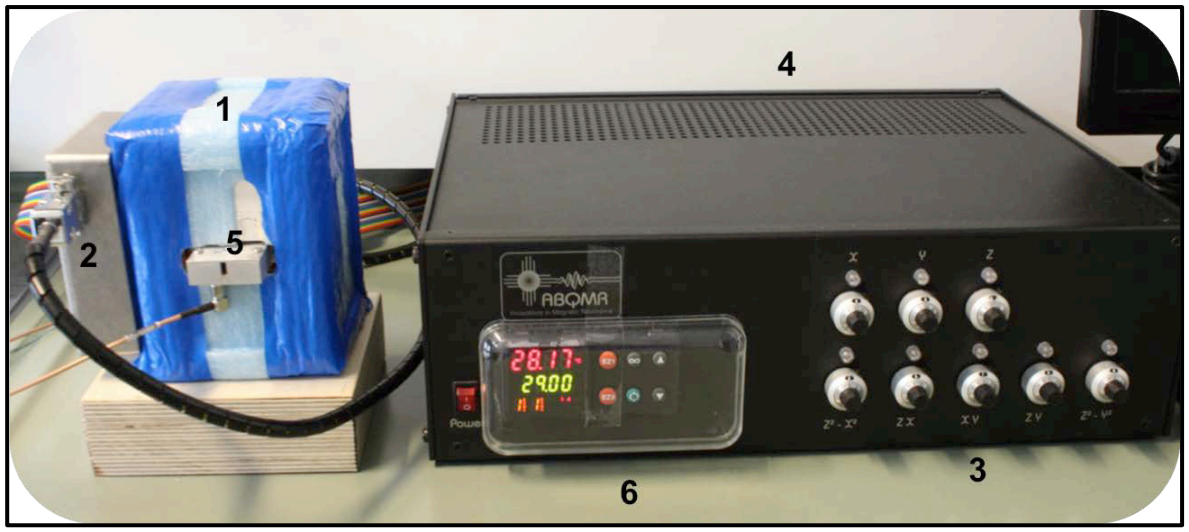


**Figure 2.19** Portable NMR instrument: 1) 1.6 T permanent magnet, 2) control for heater pads and shims, 3) shim control electronics, 4) radio processor, 5) tuning/matching circuit box with microprobe, and 6) temperature control unit

Typically the following experimental parameters (see Table 2.9) were used to acquire NMR data.

**Table 2.9** Typical experimental parameters for the portable NMR instrument

| | |
|---|---|
| Pulse sequence | 90° one-pulse excitation |
| $^{1}$H frequency | 70.9 MHz |
| $^{19}$F frequency | 66.7 MHz |
| Acquired points | 512 |
| Spectral width | 4 or 16 kHz |
| Acquisition time | 16 to 64 ms |
| Pulse width | 24 µs |
| Pulse transmitter power | 2.5 mW |
| Scan delay time | 1 to 2 s |

Usually, the results were detected as single scan experiments with an acquisition time in the low millisecond range. However, scan averaging over a few seconds time interval was possible and used in some cases, especially when lower sample concentrations were present. The NMR spectra were calculated using a Fourier Transform from the free induction decays (FID) with 0$^{th}$ and 1$^{st}$ order phase corrections applied. For static experiments 10 cm long, sealed synthetic fused-silica or borosilicate glass sample capillaries (CV4055s and CV4055, VitroCom, Mountain Lakes, NJ, USA) of 400 µm i.d. and 550 µm o.d. were inserted into the NMR microcoil probehead, which is explained in the following Chapter 2.2.2.

### 2.2.2 Microcoil Probehead

A miniaturized NMR instrument with a small permanent magnet requires a small (2.5 x 10 mm) NMR probehead, so that it can be accommodated in the narrow magnet bore. This also means a reduced-volume RF receiver coil must be used. Assuming a concentrated analyte, these smaller RF coils lead to an enhanced mass-sensitivity, measured in terms of the ability to detect low masses of analyte. To quantify this NMR sensitivity the SNR is used, given as the peak signal height divided by twice the root mean square (RMS) of the baseline noise, which is proportional to the sensitivity.

$$\mathrm{SNR} = \frac{\text{Peak Signal}}{2 \times \text{RMS Noise}} \propto \frac{1}{d_{\mathrm{coil}}} \qquad \text{Equation 2.4}$$

As shown in Equation 2.4 and Equation 1.2 the SNR is inversely proportional to $d_{\mathrm{coil}}$ of the RF coil [9][14]. This means, using smaller RF coil diameters ($d_{\mathrm{coil}}$ = µm range), the SNR is increased, benefitting the intrinsically poor NMR sensitivity, such that smaller sample amounts (nL range) can be analyzed with these miniaturized RF coils yielding higher sensitivities compared to typical lab-scale NMR coils ($d_{\mathrm{coil}}$ = cm range) [53][54].

The development of these smaller active coil volumes in NMR spectroscopy led to a wide range of applications using RF microcoil NMR combined with microseparation techniques, *e.g.* capillary liquid chromatography (capLC) [55][91], CE [21][25][29][56], and capillary isotachophoresis (cITP) [57], during the last 20 years [19]. Very essential for these on-line couplings of a microseparation technique, such as CE, to NMR is the size of the microcoils (see Chapter 2.2.2.3).

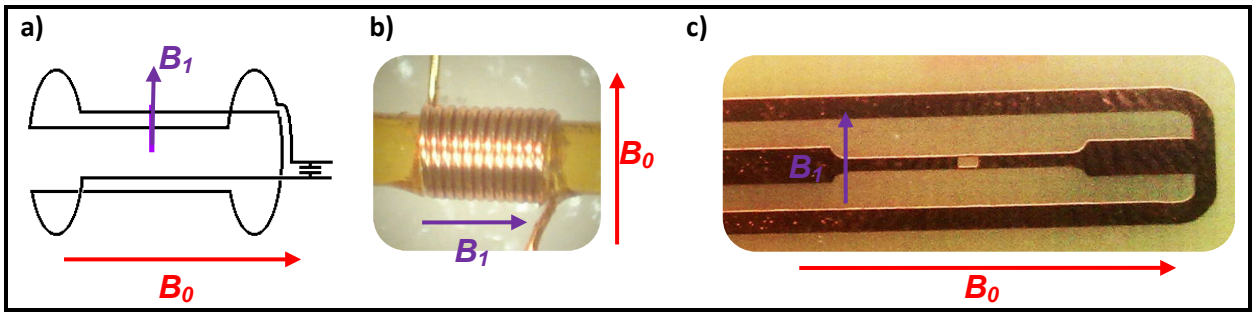


**Figure 2.20 a)** Schematic of saddle coil [58] and pictures of **b)** solenoidal, and **c)** slotted coil

Different coil geometries have also been used to couple chemical separation techniques with NMR. The typical NMR coil geometry is the saddle coil (see Figure 2.20 a), oriented such that $B_0$ is parallel to the long axis. Alternative RF coil designs include solenoidal (see Figure 2.20 b) and slotted microcoils (see Figure 2.20 c), where $B_0$ is oriented as shown. These coils and their applications in the coupled instruments are described in the next chapters.

#### 2.2.2.1 Challenges in the Microcoil Design for the CE-NMR Integration

The coupling of CE with microcoil NMR presents several challenges in the probe design. In lab-scale CE-NMR experiments solenoidal microcoils are used, such that the CE capillary has to run through the microcoil located in the center of the magnet, which leads to an perpendicular orientation of the CE capillary and the external $B_0$ (see Figure 2.21 a). Ampère's Law states that when the sample liquid within the capillary carries electrical current, $B_2$ will be created, which circles around the capillary. These radial induced $B_2$ gradients may substantially interfere with the $B_0$ of the permanent magnet causing asymmetrical line broadening of the NMR signals [25]. This degradation in the NMR signals will lead to a sensitivity decrease and lower spectral resolution such that the obtained structural information will be severely limited. Therefore, this induced $B_2$ must be counteracted when solenoidal microcoils are used to avoid the detrimental line broadening effect (see Chapter 3.2.2).

A promising coil design alternative, for the solution of the electrophoretic current induced line broadening problems, are slotted microcoils [13][26][59]. These microslot NMR probes use a thin metal strip positioned parallel to $B_0$ to produce the perpendicular $B_1$ magnetic field and detect the NMR signal (see Figure 2.20 c). This design can be compared to a Cu wire that produces a magnetic field which encircles it when current is applied. The $B_1$ magnetic field lines produced by the strip run parallel to the surface and a small, rectangular hole is cut into the microstrip waveguide to create a homogeneous $B_1$. In addition, this planar slotted microcoil design offers the possibility to orient the CE separation capillary parallel to $B_0$ (see Figure 2.21 b). Additional magnetic $B_2$ fields, induced by the CE separation current, will then be perpendicular to $B_0$, so that no additional line broadening from electrophoretic flow should be expected [13]. This means that the spectral resolution can be enhanced during the CE-NMR experiment. The probe design used in this research work extends the approach of Maguire et al. [59] who used a small microslot in a microstrip waveguide to create a homogeneous $B_1$.

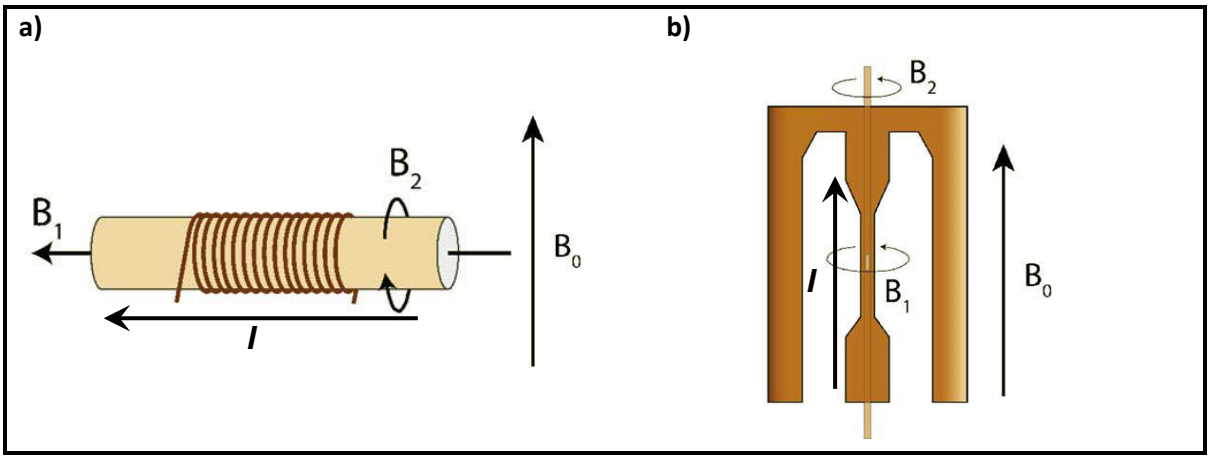


**Figure 2.21** Schematic illustration of the **a)** solenoidal microcoil, and **b)** slotted microcoil showing the direction of the magnetic fields created by the coil/slot ($B_1$), $I$ running through the capillary, the current induced magnetic field ($B_2$) and the static magnetic field ($B_0$) [13]

We investigated both microcoil designs, slotted and solenoidal, to determine which is most appropriate for the CE-NMR hyphenation.

#### 2.2.2.2 Slotted Microcoil Assembly

One advantage of the slotted microstrip is the easy accommodation of different sample geometries and volumes which is only limited by the range of the induced $B_1$ magnetic field homogeneity. Tubes or capillaries with varying i.d. and o.d. can be used without switching the probehead. Using this planar configuration the sample can even be dropped on top of the coil, such that no sample container is needed, however, the probe tuning must be adjusted.
Additionally, as previously stated, the slotted microstrip avoids NMR linebroadening due to the capillary current, because the electrophoretic current is parallel to the static magnetic field $B_0$ (see Chapter 2.2.2.1).
The sensitivity of this slotted microstrip must be investigated in more detail, when used in a low field magnet, since this is one of the most critical aspects for choosing the ideal microcoil design. A disadvantage of the microslot coil design is the time-consuming micro-fabrication, necessary to produce them (see Table 2.10), in contrast to the easily wound solenoidal microcoils (see Chapter 2.2.2.3).

**Table 2.10** Photolithographic process for the slotted microcoil construction

| | | |
|---|---|---|
| Cleaning & polishing of circuit board | Isopropyl alcohol is used to clean the copper surface of the circuit board; abrasive paper with different grain sizes is used to polish it; then the board is dried under infrared (IR)-lamp (10 min). | 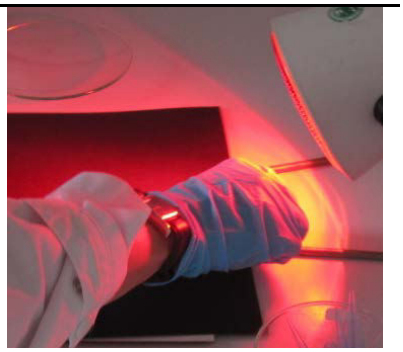 |

| | | |
|---|---|---|
| Photoresist application | Cover surface uniformly with thin film (1-2 drops) of photoresist (AR-U 4040 Alresist) using brush and roller; cover the board with a sheet of black paper and dry it under IR-lamp (30 min). | |
| Exposure | Optical mask for microslit and support structure is laid on top of the photoresist covered board and the UV-light is switched on for 25 s in a vacuum chamber. | 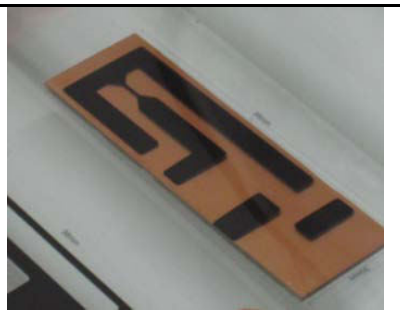 |
| Developing | Board is laid into NaOH solution (7 g/L) for 10 s to remove exposed photoresist, then rinse with water. | |
| Etching | Board is immersed in etching bath filled with sodium persulfate for 20 min to remove copper. | 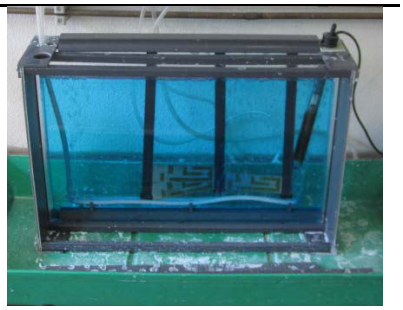 |
| Cleaning | Slotted microcoil is examined with microscope to mechanically remove any further unwanted copper parts. | |

The microslot coil and circuit board fabrication was performed as follows. First, the RF circuit board (Rogers RT 5880, Advanced Circuit Materials Division, Chandler, AZ, USA) was cut into the desired size, which depended on the geometry of the magnet bore. Second, the photolithographic process, developed at the ISAS institute [26] (see Table 2.10), was used to chemically etch the microstrip and the support structure for soldering of the capacitors and the cables on one side of the circuit board, using an optical mask (see Figure 2.22).

**Figure 2.22** Optical mask to fabricate the slotted microcoils using photolithography

The slit size of the microcoil was chosen to be 0.4 x 0.9 mm, so that it matched the sample capillary dimensions (400 µm i.d.). The inductance of this slotted microcoil was 11 nH, about 5 times smaller than the solenoidal coil with similar dimensions (see Chapter 2.2.2.3) which lead to disadvantages for the tuning and matching procedure in the NMR, discussed later.
To demonstrate the avoidance of the line broadening effect during the CE-NMR experiment (see Chapter 2.2.2.1) with these slotted microcoils, the custom-built probehead was integrated in a fully shimmed 500 MHz (11.7 T) Bruker Avance NMR System and coupled to a self-fabricated CE system. The schematic of the probehead circuit and a picture, using variable, nonmagnetic trimmer capacitors (Voltronics Corporation, Salisbury, MD, USA) with a range of 1-16 pF are displayed in Figure 2.23.

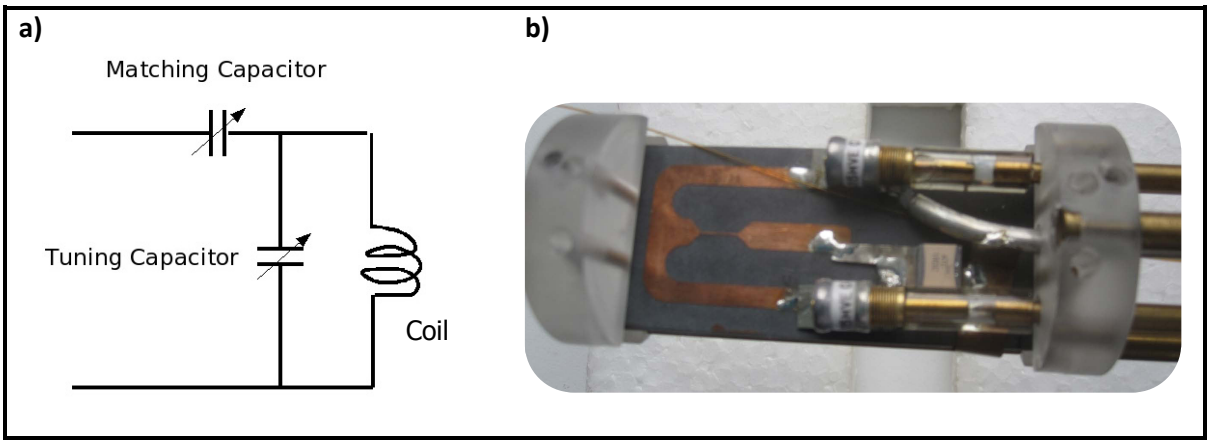


**Figure 2.23** Electrical circuit of the custom-built probehead for the slotted microcoil: **a)** schematic [60] and **b)** picture

Figure 2.24 shows the full width at half maximum (FWHM) of the $^{1}H$ NMR linewidth for the $H_2O$ signal in a 50 mM phosphate buffer (pH 3) as a function of the applied current in the CE capillary. During these experiments all NMR parameters, including the shim settings, were held constant in order to compare the results.
No changes were detected in the linewidth, meaning that there is no linewidth dependence on the CE current, even at electrophoretic currents as high as 55 µA. The line shifts observed with electrophoretic currents of more than 20 µA were due to Joule heating effects occurring in the CE capillary. The temperature in the experiment changed because of the buffer heating, resulting in a total frequency drift of 5 Hz (= 0.01 ppm), corresponding to 0.14 Hz/µA (= 0.00029 ppm/µA) for currents above 20 µA. However, these temperature dependent drifts were minor (compare to Chapter 2.2.4), and no further improvements were deemed necessary.

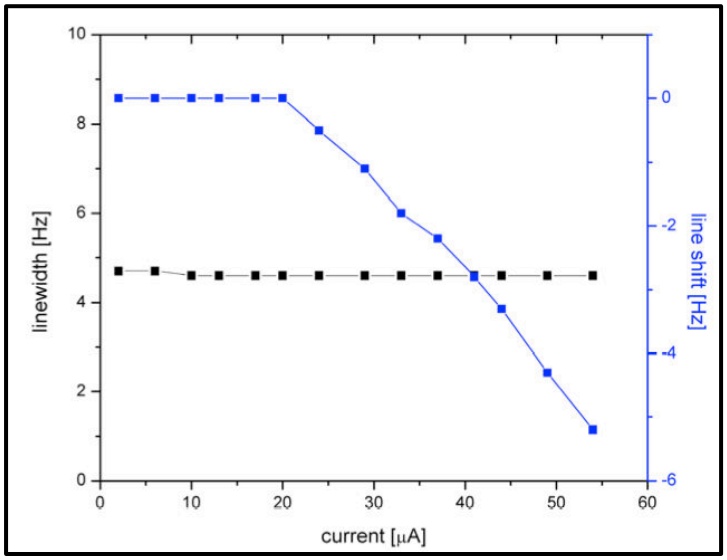


**Figure 2.24** FWHM linewidth (black) and line shift (blue) of the $H_2O$ signal in a 50 mM phosphate buffer as a function of electrophoretic current, obtained with a slotted microcoil detector during an on-line CE-NMR experiment [61]

Although slotted microcoils have demonstrated good sensitivity and resolution in lab-scale NMR instruments [13][26][59], a few major challenges remain before moving these microcoils to a portable CE-NMR system. The biggest of which is the slotted microcoil as designed will not fit in the 1.6 T box magnet used in this research work. The bore of the magnet is too small and cannot accommodate the microslot in the proper orientation. An alternative portable permanent magnet (SpinCore Technologies, Inc., Gainesville, FL, USA) with a magnetic field of 0.5 T (21 MHz) and a magnet bore of 3 cm, large enough to fit the slotted microcoil probehead, was tested. However, due to the small inductance of the coil (inductance = 11 nH) it was challenging to resonate the microcoil at a frequency as low as 21 MHz. Even applying the method for tuning and matching extremely small sample coils with very low inductance by adding a tuning inductor, described by McDowell [62], did not improve the performance of the microcoil. Therefore, this microcoil design could not be used in this research work to show NMR spectra in the portable NMR instrument, because either the permanent magnet bore was too small or the magnetic field of the magnet was too low. Further miniaturization of the microslot design would essentially lead to a successful use in the 1.6 T portable NMR magnet , however, at this point, this is not possible.
The CE-NMR performance of this slotted microcoil seems promising; however, there are still challenges for future developments, such that another coil design, *e.g.* the solenoidal microcoil, has to be used.

#### 2.2.2.3 Solenoidal Microcoil Assembly

The particular advantage of solenoidal microcoils is the increase in sensitivity by a factor of two to three compared to the saddle coil design, leading to an increase in the SNR, especially for small volume samples. Furthermore, this design is easy to fabricate, even at the very small dimensions necessary for the coupling of CE with microcoil NMR [87].

As stated earlier, the size of the microcoil is essential, especially in a hyphenated CE-NMR system with concentration-limited samples, such that the optimal RF coil size must be determined. To provide enough observable volume for these concentration-limited samples in the NMR coil and to match the sample peak dimensions of the CE separations, the coils have to accommodate CE capillaries hundreds of µm in size. In contrast, typical CE separations work with 50-75 µm i.d. capillaries and sample volumes of 1-20 nL, yet 100-150 nL (capillary i.d. = 350-450 µm) must be used in the coupled CE-NMR device to allow enough atoms in the RF coil to be measureable by the relatively low sensitivity NMR spectroscopy (see Chapter 2.3). The following description of the solenoidal microcoil assembly was chosen as a compromise between enclosing enough sample volume in the NMR coil to provide adequate SNR performance and the capillary dimensions which yield a high active volume in the RF coil for ideal results.

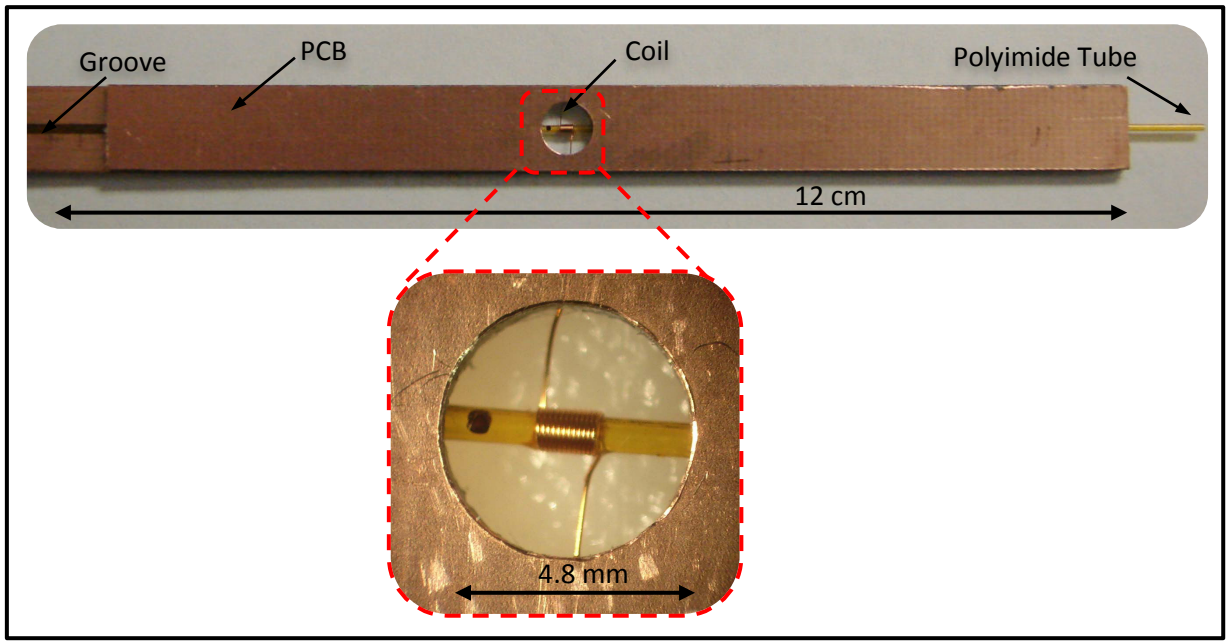


**Figure 2.25** Picture of microcoil probe (blow-up: solenoidal microcoil hand-wound onto polyimide tube)

The design of the solenoid microcoil NMR probe is as follows (see Figure 2.25). The NMR probe support structure was constructed from two layers of FR-4 printed circuit board (PCB). Both layers were 0.8 mm thick; one piece had copper cladding (37 µm thickness) on both sides, while the other piece was copper clad only on one side. The multiple Cu claddings were necessary to serve as electrical grounding, shielding and electrical connections to the coil, depending on its location in the probehead assembly. The pieces were cut 9 mm wide and 12-13 cm long. A groove was milled in the center along the length of both of the PCB pieces. The groove was sized so that when the two PCB boards were held together, a square passageway was created, large enough to accept the polyimide tubing that would hold the sample capillaries up to an o.d. of 550 µm. Those sample capillaries with an o.d. of 550 µm and an i.d. of 400 µm were chosen for this research work, because the resulting observable NMR coil volume of 125 nL was ideal for further CE-NMR applications. The groove on the single-sided

PCB was milled on the non-clad side. When the two pieces were assembled (using adhesive transfer tape, 3M 9461P), they formed a structure of 1.6 mm thickness, with three copper layers separated by insulating circuit board material (FR-4). A 4.8 mm hole was cut through the PCBs to provide clearance for the NMR coil.

The coil was hand-wound onto a thin-walled 10 cm long polyimide tube of 690 µm o.d. (640 µm i.d.) (Small Parts, Inc., Seattle, WA, USA), similar to the capillary-in-capillary design, presented in Diekmann [63]. The coil was held in place using small amounts of epoxy adhesive placed at either end of the coil. The polyimide tube was glued into the groove on the double-sided PCB and the ends of the coil wire were soldered to the copper on either side of the groove. Cuts were made in the copper using a razor blade in order to form the correct circuit connectivity. The single-sided PCB was cut shorter to provide clearance for the capacitors and then attached to the top of the double-sided PCB, enclosing the polyimide tube and the NMR coil. The two outside layers of copper (the top and the bottom) were electrically connected to ground to provide RF shielding for the NMR detector circuit, which resided on the middle layer of copper. Further microcoil parameters are listed in Table 2.11.

**Table 2.11** Characteristic parameters for the hand-wound microcoil

| | |
|---|---|
| Coil length | 960 µm |
| Cu wire diameter | 40 AWG (= 80 µm) |
| Turns | 12 (tight wound) |
| Coil i.d. | 690 µm |
| Polyimide sleeve i.d. | 640 µm |
| Resistance | 1 Ohm |
| Inductance | 53 nH |

Capacitors for tuning and matching the coil were soldered directly to the PCB opposite the coil, thus forming the NMR detector circuit. Tuning and matching electronics were encased in an aluminum box (2 x 3 cm), which was mounted to the magnet to hold the probehead in place (see Figure 2.26).

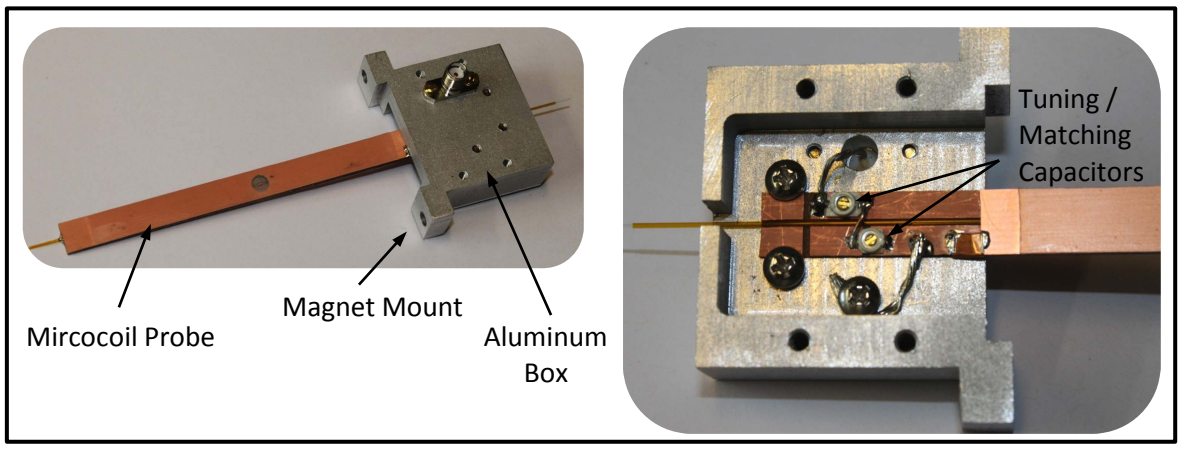


**Figure 2.26** **Left:** Picture of whole probehead including tuning / matching box and probe with microcoil. **Right:** Picture of inside-view in tuning / matching box.

This solenoidal microcoil design is used for the following research work and experimental results are shown in the next chapters. In Chapter 3.2.2 the CE current effect on the solenoidal coil performance in the coupled CE-NMR instrument is discussed in detail.

### 2.2.3 NMR Magnet

A main emphasis of this research was to build a portable NMR instrument; hence a small permanent magnet configuration was the key for this development. In lab-scale NMR systems, the magnetic field is typically generated by large superconducting magnets, which must be cryogenically cooled and weigh 500-1000 kg.

For portable NMR, permanent magnets, smaller versions of those used for NMR spectroscopy in the 1960s and 1970s, were used [32]. Over the past decade, several different small magnets using open and closed designs have been described in literature and some have been commercialized, *e.g.* the NMR-MOUSE [64][65]. However, for high resolution applications, *e.g.* NMR spectroscopy, closed magnet geometries that produce more uniform magnetic fields are preferred [66]. By reducing the sample detection volume, the required region of homogeneous magnetic fields can be decreased in size to mm-range. This allows the use of a smaller magnet.

A permanent magnet system based on a cylindrical pole configuration, similar to the one used in this research work was described by Demas et al. [31]. This box magnet shows optimal field homogeneity of less than 1 ppm/mm for each of the three *x*-, *y*-, and *z*-directions in the most homogeneous region of the magnet, at different magnetic field strengths of 1-2 T. Depending on the $B_0$ field it weighs 0.7-2.5 kg. The magnets have a 5 mm bore opening for the micro-liter sample insertion [67]. The following sections present more details on the magnet used in this research.

#### 2.2.3.1 Magnet Construction and Shim Coils

The permanent dipole magnet (SN007, Aster Enterprise, Inc., Acton, MA, USA) had a $B_0$ of 1.6 T, weighted 2.4 kg (see Figure 2.27 c), and was made from samarium cobalt ($Sm_2Co_{17}$). The housing material was made from nickel-plated low carbon steel and the poles were fabricated using Hiperco Alloy 50A (Fe-Co-V-alloy). The schematics in Figure 2.27 a and b show the side and top view of the magnet, with the 5 x 10 mm rectangular bore opening at the side. The magnet field points along the 5 mm direction, with the most uniform magnetic field spot at the nominal center of the magnet.

For acquiring NMR spectra it is very important to know the homogeneity of the $B_0$ distribution in the magnet. Figure 2.28 displays the magnetic field maps near the geometric center of the magnet as a function of position along the *x*- and *y*-axes. For each of those directions, field values are shown for $z = 0$ (center of the 5 mm opening), for $z > 0$ (0.3 mm above the center), and for $z < 0$ (0.3 mm below the center). The field values were acquired with an NMR field mapper and are plotted in ppm units, relative to the nominal 1.6 T magnetic field strength.

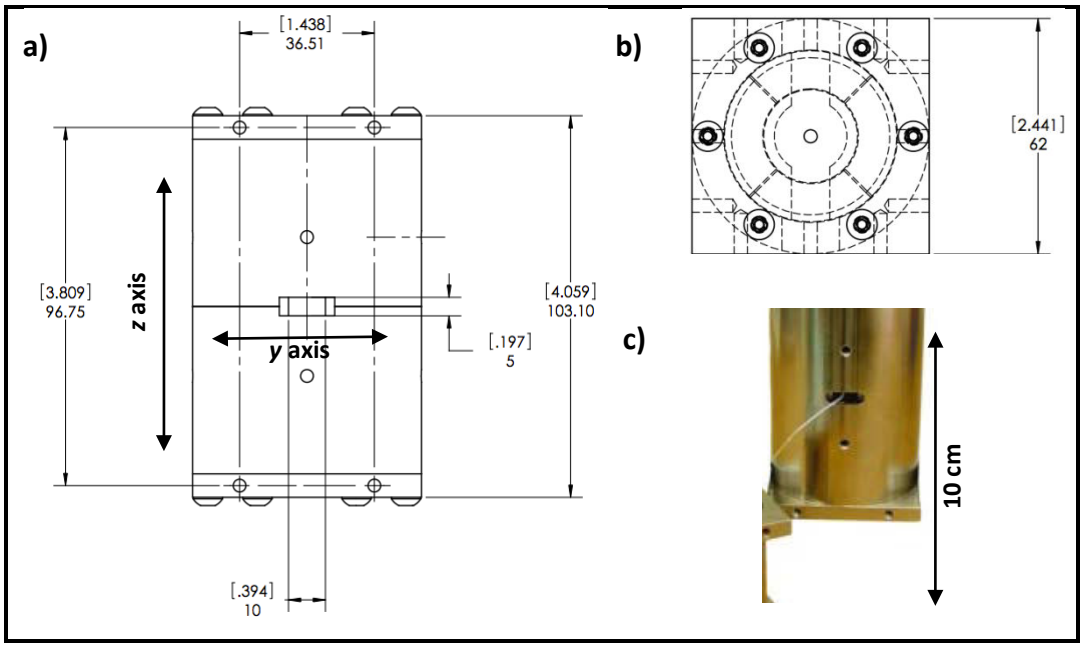


**Figure 2.27** $Sm_2Co_{17}$ pole magnet **a)** schematic of magnet side view with rectangular bore opening, **b)** magnet top view and **c)** picture of magnet side view (numbers in mm and [numbers] in inch)

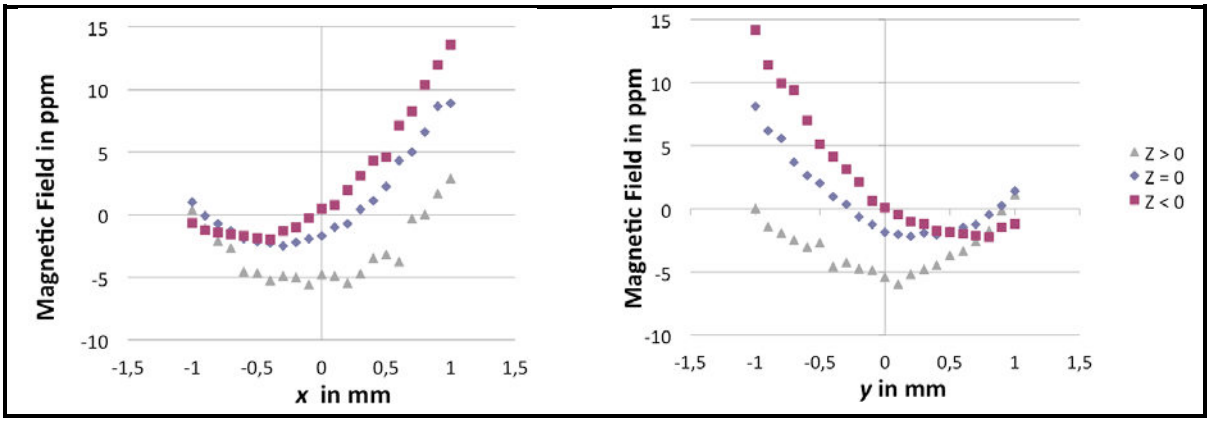


**Figure 2.28** Magnetic field maps of $B_0$ in ppm along the *x*- , *y*- , and *z*-axis in the 1.6 T $Sm_2Co_{17}$ magnet

For a specific sample size and location in the magnet, the $B_0$ maps, which are illustrated by the parabolas, allow an estimate of the magnetic field variations and therefore its homogeneity, over that sample volume. For example, for the 1 mm long, 0.4 mm diameter sample volume used in this research work (see Chapter 2.2.6) which would be located in the geometric center of the magnet, the fields vary from a low of -1.9 ppm at $x$ = -0.5 mm to a high of 2.3 ppm at $x$ = 0.5 ($\Delta$ = 4.2 ppm) along the middle plane ($z$ = 0) of the magnet. Similarly the variations in the *y*-axis, which span from -0.7 ppm at $y$ = -0.2 mm to -2.2 ppm at $y$ = 0.2 mm ($\Delta$ = 1.5 ppm) along $z$ = 0. The sample volume also covers the *z*-axis from -0.2 to 0.2 mm, which would add about 1.5 ppm to the total field variations. For the entire sample volume, one might estimate a total field variation of ~7 ppm, or perhaps even more, depending on the individual magnetic field interactions in all three directions.

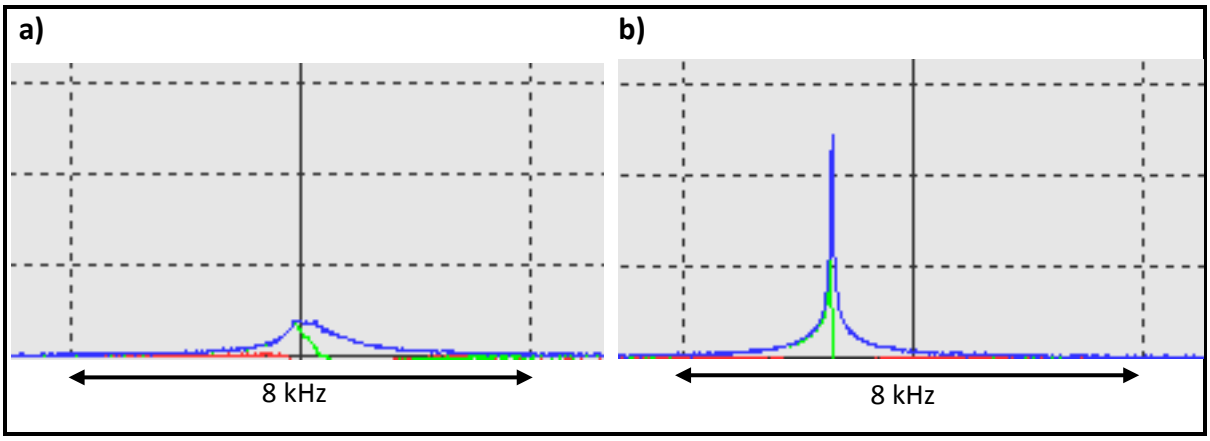


**Figure 2.29** $^{1}H$ NMR single scan spectra of $H_2O$ in a 400 µm i.d. sample tube **a)** taken in the 1.6 T $Sm_2Co_{17}$ magnet and **b)** taken in the shimmed 1.6 T $Sm_2Co_{17}$ magnet

To show the significant impact of these field variations in NMR spectroscopy, a $H_2O$ NMR spectrum is taken using the 1.6 T $Sm_2Co_{17}$ magnet (see Figure 2.29 a). The linewidth at FWHM of the $H_2O$ signal is ~1000 Hz (= ~14 ppm). Since the chemical shift range for $^{1}H$ NMR spectroscopy covers 18 ppm, these results show that this $Sm_2Co_{17}$ magnet, without any further improvements, is not capable of doing $^{1}H$ NMR spectroscopy.

To improve the magnet performance during this research work, compared to the previous studied systems of Diekmann [63], internally integrated 1st and 2nd order shim coils were used in the magnet. The currents in the shim coils were adjusted such that the coils created a magnetic field distribution that corrected the parabolic $B_0$ variations shown in Figure 2.28.

The 1st order shim coils produce a linear variation, which shifts the position of the parabola, while the 2nd order shim coils produce a quadratic variation of the magnetic field, which adjusts the nature of the parabola. During this shimming process the shim currents of the individual coils (three 1st order shim coils: $x$, $y$, $z$ and five 2nd order shim coils: $zy$, $xy$, $zx$, $z^2$-$x^2$, $z^2$-$y^2$) must be adjusted to cancel any field variations in the NMR sample as accurately as possible to obtain satisfactory NMR spectra.

Using those shim coils in the magnet, a 100 times more homogeneous magnetic field compared to the unshimmed magnet was achieved, producing a signal FWHM linewidth of 10 Hz (= 0.14 ppm) for the same $H_2O$ sample as used above (see Figure 2.29 b). In contrast to the raw magnet, this shimmed magnet is capable of doing $^{1}H$ NMR, due to the improvements in the NMR resolution. In addition, these results show that the more homogeneous $B_0$ increases the sensitivity, because the area under the curve is constant for both spectra.

The shim coils were constructed on two identical multi-layer PCBs following a proprietary pattern (information is held as a “trade secret”). The two PCB “paddles” were attached to the two pole faces of the magnet during magnet manufacture. Care was taken to minimize the thickness of the PCBs in order to maximize the remaining working volume inside the magnet. The electrical current in each of the eight independent shim coils was separately controlled by an 8-channel, current-feedback shim amplifier. Front panel potentiometers on the shim amplifier box allowed the user to adjust the currents of each coil in order to achieve the most homogeneous field and thereby the highest resolution.

#### 2.2.3.2 Magnet Insulation

The $Sm_2Co_{17}$ permanent magnet has a magnetic field whose strength varies with temperature by -350 to -400 ppm/°C. Since high resolution $^1H$ NMR requires a resolution of better than 1 ppm, thermal stabilization of the permanent magnet is important to minimize the temperature induced $B_0$ frequency shifts.

The thermal stabilization system (see Figure 2.30) of the permanent magnet consisted of two boxes made from 6.4 mm thick 6061 aluminum alloy, assembled with 4-40 steel screws. The magnet was mounted directly to the inner box, using four 8-32 steel screws. The magnet was mounted from one side so that only this side of the inner box contacted the magnet. Thus, the inner aluminum box forms an isothermal surface surrounding the magnet and the magnet is in nearly isotropic contact with this surface. In between the aluminum boxes two layers of thermal insulation Arlon 680-R3844R (Silicon Technologies, Bear, DE, USA) were placed.

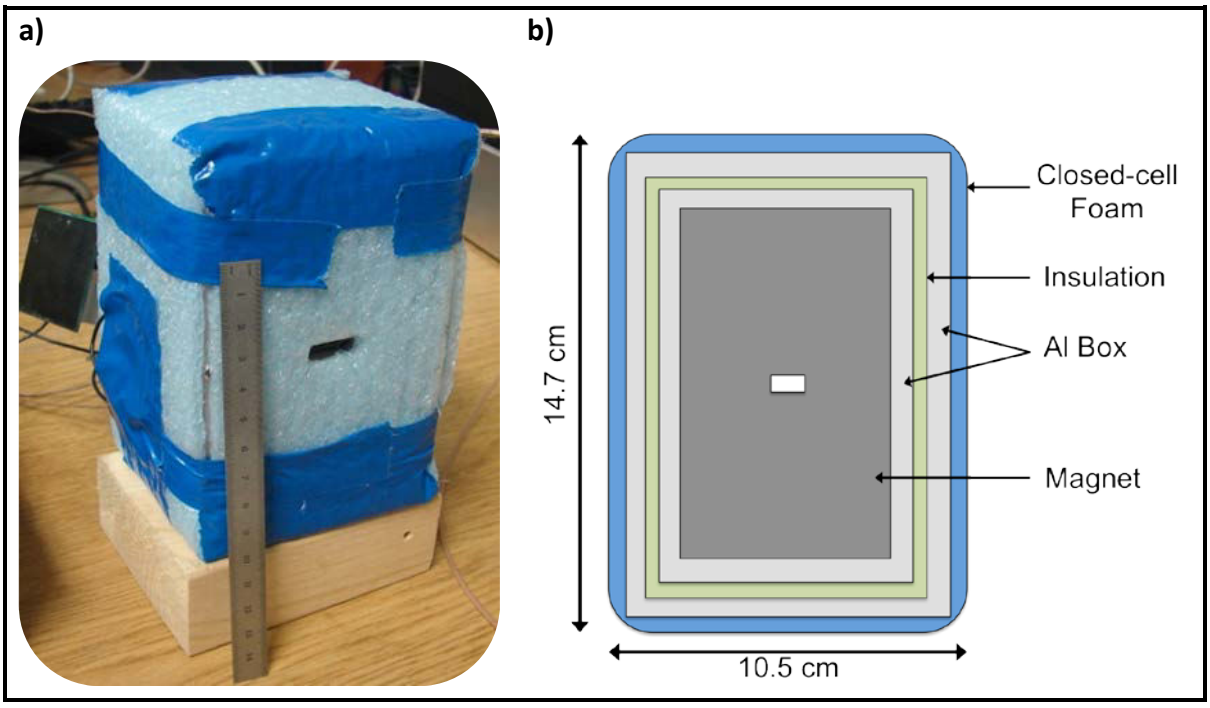


**Figure 2.30 a)** Picture with 15 cm silver ruler and **b)** schematic of thermally insulated magnet

The inner and outer boxes were independently heated using pairs of resistive heater pads. The inner box heaters were built on a polyimide substrate and provided a total of 10 W of heating power. The outer box heaters were encased in silicone rubber and provided 22.5 W. To control the heater pads Watlow EZ-Zone PM6C1KK-AAAAAAA (InstruMart, Carlsbad, CA, USA) temperature controllers were used. The inner box was held at 29°C and the outer box at 28°C. There was just enough space between the aluminum boxes to accommodate the insulation and the polyimide heaters. Additionally, there was a small amount of insulation on the outside of the magnet module consisting of ~5 mm thick pieces of blue closed-cell foam (see Figure 2.30). In this construction, the outer aluminum box forms a nearly stable, isothermal surface that shields the inner layer from the large variation in room temperature, thereby providing the inner layers a much more stable rate of heat loss.

After assembling this simple thermal insulation construction around the permanent magnet it needs to be validated and compared to other temperature stabilizing methods, as described in the following chapter, to prove its thermal stabilization performance.

### 2.2.4 Temperature Influence on NMR Detection

One of the key challenges in portable NMR technology is that portable systems are by their nature exposed to environments with changing temperatures. This means, varying ambient temperatures can change the $B_0$ strength, as stated by Curie's law, and thus the frequency, which shifts the NMR chemical signatures, as mentioned in the previous chapter. For concentrated samples and quick single pulse experiments these temperature influences might not be significant. But if the sample of interest is diluted, more scans have to be averaged over a long time period, so that frequency drifts due to temperature changes will counter the advantage of spectral accumulation by broadening and smearing spectral peaks.
In comparison to other classes of permanent magnets, *e.g.* ferrite magnets or neodymium iron boron magnets, the thermal characteristics of the $Sm_2Co_{17}$ permanent magnets are excellent, as shown by their reversible temperature coefficient (RTC) [68]. Also, the temperature dependence of the magnetic material is not linear, meaning that the RTC is temperature dependent. The manufacturer of the $Sm_2Co_{17}$ magnet quotes a RTC value between -350 to -400 ppm/°C, which is typical for a $Sm_2Co_{17}$ magnet. The negative RTC means that the magnetic $B_0$ field goes down as the temperature goes up. The stated temperature dependence is strong: the NMR peak would drift about 25 kHz within a 1°C change. This means a very large spectral width, which is the range of NMR frequencies being observed, of at least 50 kHz has to be used during the NMR acquisition. This results in lower SNR due to more electrical noise which will be captured in the larger spectral width region. Comparing to the regular spectral width, which was used in this research of 16 kHz, this is a factor of three higher.
Another approach to minimize the temperature influences of the permanent magnet is the use of different types of magnet material to decrease the RTC value, instead of using insulation material around the magnet. By adding paramagnetic metals such as gadolinium to the $Sm_2Co_{17}$ matrix the RTC can be reduced to -16 ppm/°C (Electron Energy Corporation (EEC) $Sm_2Co_{17}$ TC-16 material). This reduction in RTC is possible because the paramagnetic metal has a positive RTC which off-sets the $Sm_2Co_{17}$ negative RTC. However, adding gadolinium into the $Sm_2Co_{17}$ matrix also reduces the overall magnetic strength of the material when compared to a magnet with the same size: a pure $Sm_2Co_{17}$ magnet has a $B_0$ of 0.9 T, whereas the temperature compensated (TC) magnet of the same size has a $B_0$ of 0.76 T, $\sim$16 % smaller.
Instead of using different magnets to compensate the temperature dependent frequency drift, post-processing methods, such as the implementation of temperature calculated frequency drifts described in Diekmann [63] and Adams et al. [69], may be used. However, to apply this technique the precise magnet temperatures must be monitored during each NMR acquisition,

before NMR spectra can be averaged, thus NMR results which require scan averages cannot be obtained directly. Even though this post-processing method greatly improves the spectral resolution, and system sensitivity, it requires precise magnet temperature measurements and extensive post-processing analysis which is not convenient.

To illustrate these temperature induced frequency drifts, different magnet setups were used, including *e.g.* insulated magnets as described in the previous chapter or different magnetic materials, which are listed in Table 2.12.

**Table 2.12** Magnet setups for the temperature induced frequency drift study

| Setup | $B_0$ | Material | Insulation |
|---|---|---|---|
| A | 1.60 T | $Sm_2Co_{17}$ | yes |
| B | 0.76 T | TC-$Sm_2Co_{17}$ | no |
| C | 0.90 T | $Sm_2Co_{17}$ | no |

#### 2.2.4.1 Temperature Drift Performance of Insulated Magnet

To demonstrate the frequency drifts in the insulated, temperature-stabilized 1.6 T $Sm_2Co_{17}$ permanent magnet (Setup A), a data logging thermometer (HH306, Omegaette, Stamford, CT, USA) was used to monitor the temperature variations of the room and the magnet during two separate overnight runs. To detect the $^1H$ NMR frequency drifts, a 0.4 mm i.d. and 0.55 mm o.d. sample tube filled with $H_2O$ was used and 90° pulse experiments were run every 5 min (NMR parameters see Chapter 2.2.1).

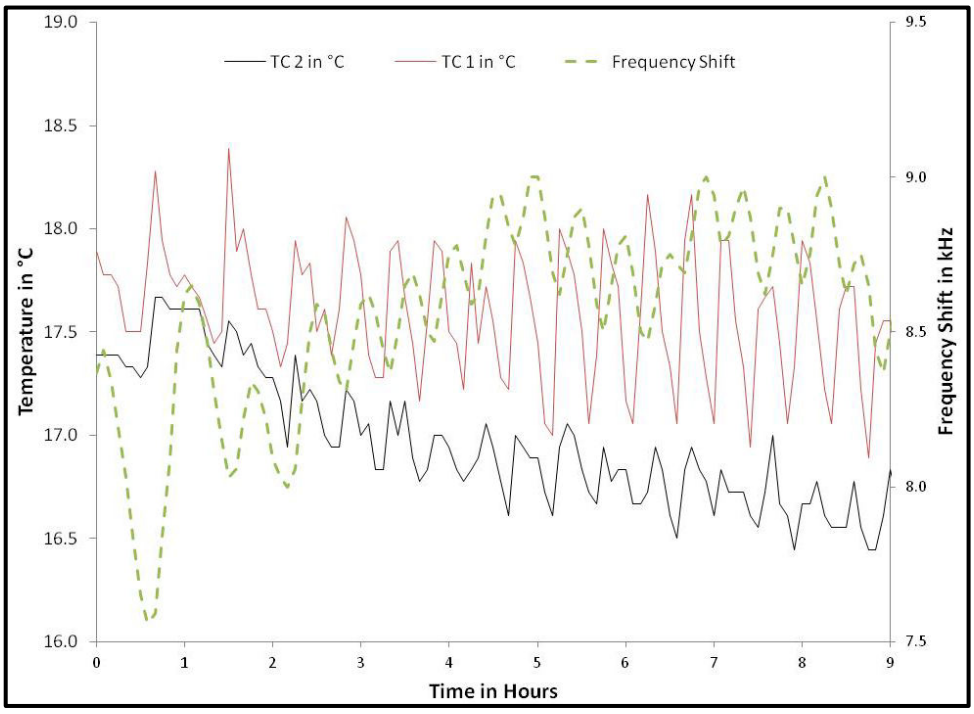


**Figure 2.31** Temperature variations in °C (blue = TC 2 mounted 1 m away from NMR; red = TC 1 mounted 1 m away from NMR but closer to room heating system) and NMR frequency shift in kHz (green) against time for the insulated 1.6 T $Sm_2Co_{17}$ magnet

In the first experiment, both thermocouples were approximately 1 m away from the NMR instrument, to show the room temperature variations. Thermocouple 1 (TC 1) was closer to the room heating system, than thermocouple 2 (TC 2), resulting in larger temperature changes.

Figure 2.31 shows the results of this 9 h run displaying the frequency shift in kHz on the right *y*-Axis and the temperature drifts in °C on the left *y*-Axis. It can be seen that the NMR frequency shifts to higher magnetic fields as the temperature drops. This dependence is expected from the negative RTC value of the permanent magnet material. The temperature oscillations detected throughout the run were a result of the interval cycles of the room heating system, which apparently turned on every 20 min.

Overall the temperature changes were -1.5°C at TC 1 and -1.3°C at TC 2. However, the frequency just drifted 21 ppm (= 1.5 kHz), resulting in a temperature dependent frequency drift of -14 to -16 ppm/°C. Compared to the RTC values of $Sm_2Co_{17}$ material the temperature-stabilized magnet shows an improvement by a factor of 16 to 20. This improvement is enough to allow the use of the desired narrow NMR detection spectral width (≤ 16 kHz) without adjusting the NMR spectrometer frequency.

In the second experiment, the same samples and parameters were used, however, the thermocouples were placed on the two aluminum insulation boxes. TC 1 was glued on the inner layer of the aluminum box next to the tuning and matching circuit box, and TC 2 was glued on the opposite side of the magnet on the outer layer of the aluminum box beneath the closed-cell foam. Figure 2.32 shows the results of this measurement (note the difference in scale compared to Figure 2.31).

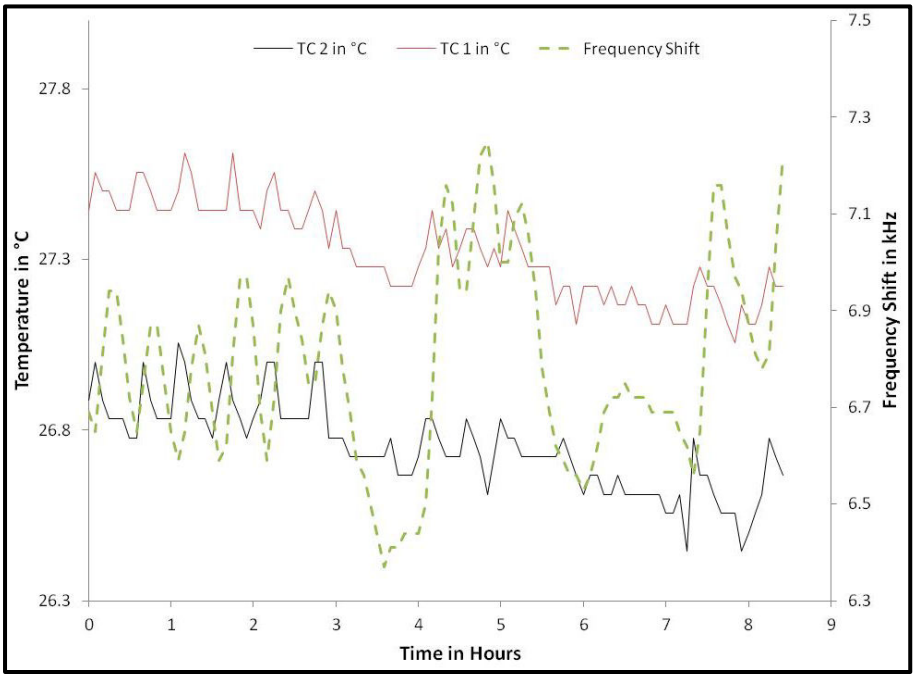


**Figure 2.32** Temperature variations in °C (blue = TC 2 outer aluminum layer; red = TC 1 inner aluminum layer) and NMR frequency shift in kHz (green) against time for the insulated 1.6 T $Sm_2Co_{17}$ magnet

The magnet temperatures measured at the aluminum boxes were much higher than the room temperatures, since the heaters were set to 29°C and 28°C for the inner and outer aluminum boxes, respectively. The temperature changes of the inner and the outer aluminum box layers corresponded to each other throughout the run, and were almost stable between 4 and 6 h after a significant temperature drop. However, the temperature changes (ΔTC 1 = -0.5°C and ΔTC 2 = -0.7°C) were approximately half the size of the variations in the room temperatures observed in the first experiment, because the thermal mass of the aluminum box reacted more slowly to the surrounding air temperature changes. The frequency drifts in this experiment of 13 ppm (= 0.9 kHz) resulted in a temperature dependent drift of -18 to -26 ppm/°C. The significant increase in the NMR frequency drift after 4 h was due to the rapid decrease in temperature at the same time. These results were about a factor 1.5 higher than those observed in the first experiment, which was presumably due to variables in the heating system.

The resulting temperature dependent frequency drifts of these two experiments (Setup A) show that the simple two-layer thermal stabilization system around the permanent magnet serves as an effective thermal barrier between the laboratory and magnet temperatures. The NMR frequency is stable to 1.5 kHz, which greatly enhances the usability of the portable NMR system in environments with changing temperatures.

#### 2.2.4.2 Comparison to Non Insulated and Temperature Compensated Magnets

Prior to the construction of the thermally stabilized 1.6 T magnet (Setup A) described above, the possibilities of using a magnet constructed from reduced RTC material (Setup B) and a normal $Sm_2Co_{17}$ magnet without thermal insulation (Setup C) were explored. Both of these studied magnets were smaller and had weaker fields than the 1.6 T $Sm_2Co_{17}$ magnet in Setup A, but the same design with equivalent form factors and weight of magnetic material for temperature stability. The TC magnet made from TC-$Sm_2Co_{17}$-based material ($Sm_2Co_{17}$ TC-16 material) had a stated RTC of -10 ppm/°C, which is about 35 to 40 times lower than the standard $Sm_2Co_{17}$ material. Neither of these two magnets (Setup B and C) had thermal insulation or temperature control.

The following experiments were conducted using the same HH306 thermometer data logger to observe the temperatures of the magnet at the bore opening and the room. Concentrated FC-43 (perfluorotributylamine; $CF_3(CF_2)_3)_3N$) was used as the NMR sample for these $^{19}F$ NMR experiments, and 16 scans were averaged every 5 min.

The NMR spectra in Figure 2.33 were obtained in a 5 h experiment during the day using Setup C. Also shown in Figure 2.33 are the temperatures of the magnet and the room. The NMR frequency drifts 550 ppm (21 kHz) while the temperature of the magnet and the room changed by -1.5°C. Due to the lack of thermal insulation, the magnet temperature followed the trend of the laboratory temperature. The NMR frequency changed as expected (RTC quoted by the manufacture = -350 to -400 ppm/°C), with a drift of -367 ppm/°C. Accommodating this -367 ppm/°C drift while maintaining maximum NMR signal detection

efficiency was difficult. Therefore, these results show that this uninsulated magnet is not suitable to use for a portable system which undergoes temperature changes in the environment.

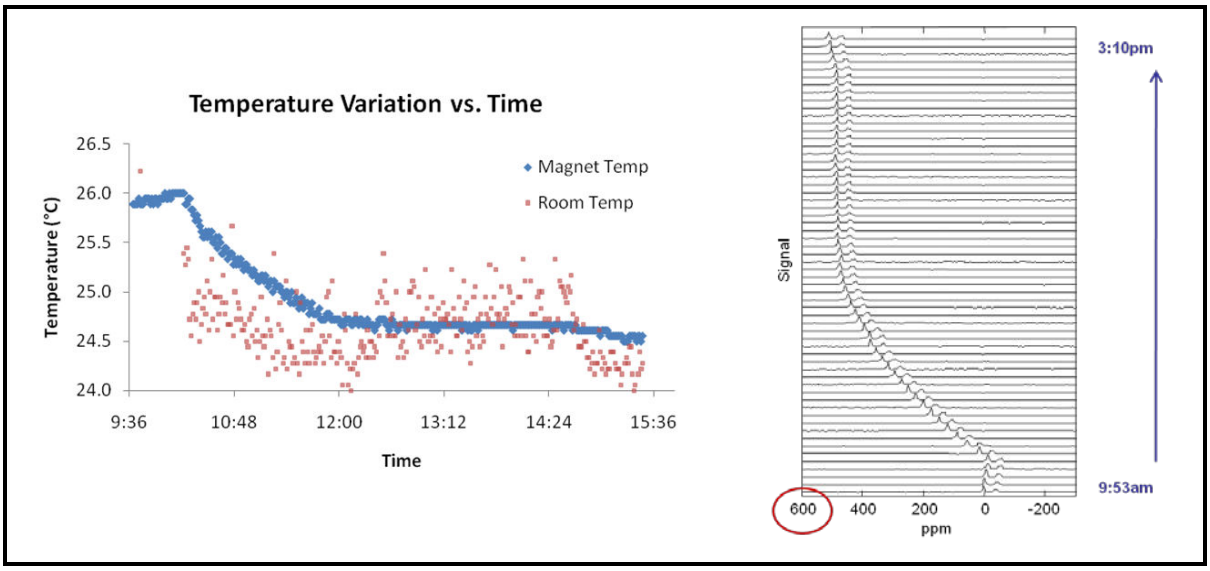


**Figure 2.33** **Left:** Temperature variations against time for the not insulated 0.9 T $Sm_2Co_{17}$ magnet (blue) due to variations in room temperature (red). **Right:** NMR spectra of FC-43 taken during a 5 h time interval showing corresponding frequency shifts caused by temperature fluctuations (Reproduced with permission from Adams et. al. [69])

As expected, the use of the reduced RTC magnet in Setup B greatly reduced the NMR frequency drift, as seen in Figure 2.34 (NMR parameters comparable to the above experiment). The temperature shifts, which are not shown in Figure 2.34, over this 10 h interval were -3.0°C, twice the temperature change observed in the previous experiment, while only a 70 ppm frequency shift (-23 ppm/°C) was observed.

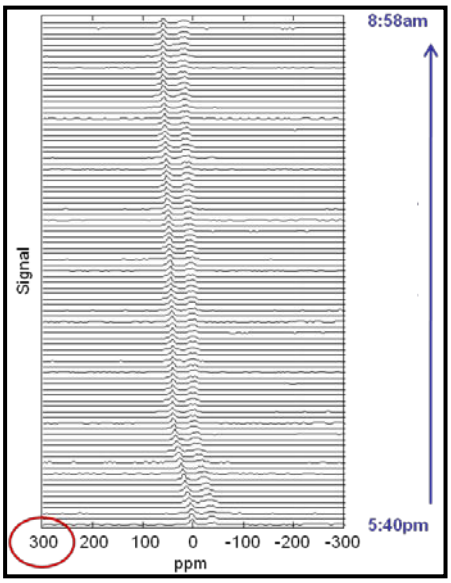


**Figure 2.34** NMR spectra of FC-43 taken during a 10 h time interval showing frequency drifts caused by environmental temperature changes over time in the 0.76 T $Sm_2Co_{17}$-TC magnet (Reproduced with permission from Adams et. al. [69])

This level of drift is easily managed in a high-sensitive NMR experiment, so the reduced RTC magnet is viable for portable applications. Comparing this result of the TC-magnet with the insulated $Sm_2Co_{17}$ magnet in the previous chapter it can be seen that similar values for the temperature dependence frequency shifts were observed.

This chapter shows the importance of either using a simple insulated $Sm_2Co_{17}$ magnet (Setup A) or to make use of a reduced RTC magnet (Setup B) when working with a portable NMR system which is affected by temperature variations. Using these types of magnets or magnet modifications, no additional post-processing techniques, as described earlier, were necessary. For further research work, the thermally insulated 1.6 T $Sm_2Co_{17}$ magnet (Setup A) was used, since its magnetic field was almost twice as high as that of the reduced-RTC magnet (Setup B).

### 2.2.5 Nutation Curve – Pulse Width Determination

Before acquiring data with the portable NMR system, the correct pulse width for the 90° exciting pulse had to be determined, because the NMR pulse length depends on the pulse power, and the probe tuning. Since the 90° pulse produces the maximum response from the analyte in the NMR coil, this excitation pulse is used for further experiments.

To determine this 90° pulse length a pure $H_2O$ sample in a sealed 0.4 mm i.d. and 0.55 mm o.d. glass tube was used. Then a series of experiments were performed using incrementally longer RF pulse widths for each experiment. The FIDs were Fourier transformed and the amplitudes for the $H_2O$ peaks were plotted as a function of pulse length (see Figure 2.35).

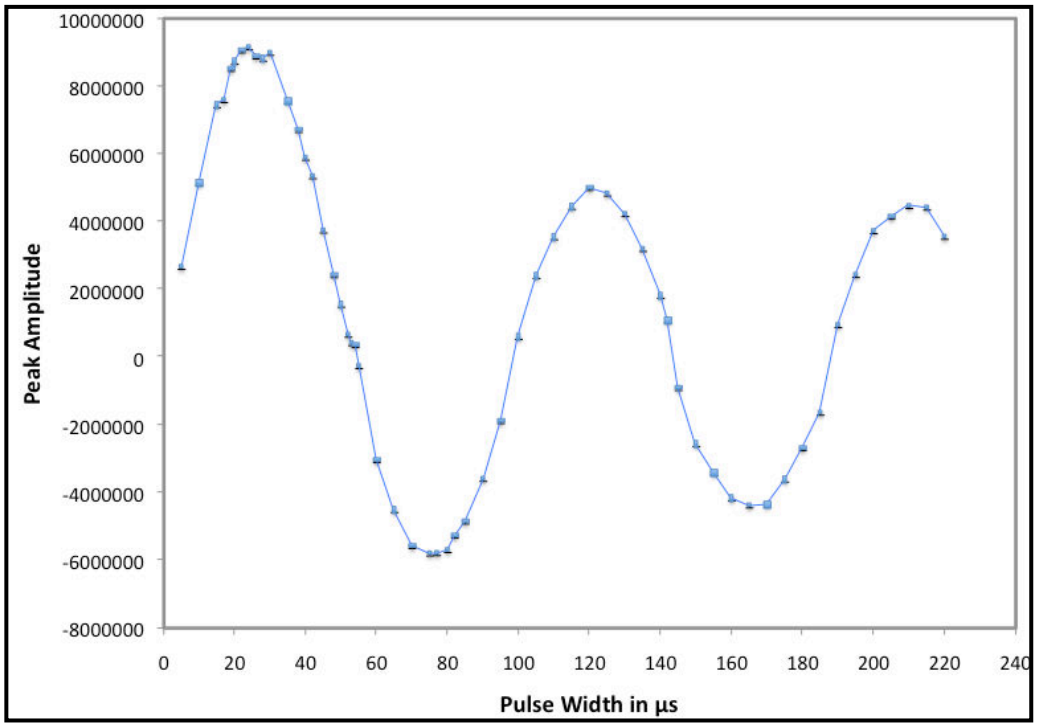


**Figure 2.35** The experimental nutation curve for a pure $H_2O$ sample with the peak amplitude plotted as a function of pulse width

The nutation curve shows that the peak amplitudes vary sinusoidally with pulse widths. The first maximum of the curve at around 24 ± 2 µs represents the 90° pulse and the zero crossing (twice the 90° pulse time) at 53 ± 2 µs the 180° pulse. Furthermore, a noticeable decrease between the amplitudes of each cycle is seen, even though same amplitude heights are expected. This effect is a result of $B_1$ inhomogeneities in the RF field strength in the detector coil, leading to a distribution of excitation pulses throughout the sample for any pulse power [58]. For all subsequent NMR experiments, a 90° pulse width of 24 µs is used to excite the sample.

### 2.2.6 Sensitivity and Resolution in $^{1}$H and $^{19}$F NMR

In the previous chapters the NMR instrument hardware was built and individual parts were tested. In this chapter, the sensitivity and resolution of this portable NMR is demonstrated, which is a critical aspect for miniaturized NMR.

It is a particular challenge for the portable instrument to achieve adequate sensitivity, in order to obtain NMR spectra from low concentrated samples, as well as sufficient resolution, to get structural information of the analyzed compound. The challenge is due to the miniaturized setup which has lower SNR of the NMR data than lab-scale NMR instruments because the magnetic field of the permanent magnet is comparatively weak. Furthermore, in order to achieve high NMR resolution, high magnetic field homogeneity (see Chapter 2.2.3) is required. This is of significant importance, because a homogeneous magnetic field also improves the sensitivity in the frequency spectrum.

Previous results for a portable NMR device, published in Diekmann et al. [16], achieved 2 ppm resolution which was not adequate for structural determination, and the low sensitivity required sample concentrations that were rather high.

In this improved NMR device using the 1$^{st}$ and 2$^{nd}$ order shim coils in the magnet, spectral resolutions of 0.02 ppm (1.5 Hz) were achieved using a 75 µm i.d. capillary as sample container (observable sample volume ($V_{observ}$) = 4 nL) and 0.2 ppm (15 Hz) using a 400 µm i.d. glass capillary to hold the sample ($V_{observ}$ = 125 nL). This improved resolution now enables access to structural information in $^{19}$F and $^{1}$H NMR spectra, while using the same probehead and coil, by just adjusting the circuit tuning to the respective observation frequency. Analytes at concentrations of 1 M and below are now routinely studied which are comparable to CE-NMR work based on traditional high-field NMR systems. This enhanced sensitivity allows the detection of samples with concentrations and volumes more compatible with CE.

The results show NMR spectra of various analytical compounds using $^{19}$F and $^{1}$H NMR which were studied in this work. The different sample solvents, used for the NMR detection, did not alter the NMR spectra, due to the high sample concentration and the NMR resolution of 0.2 ppm. For these experiments the NMR system explained in Chapter 2.2.1 was used consisting of the solenoidal microcoil and the thermal insulated 1.6 T $Sm_2Co_{17}$ permanent magnet.

### 2.2.6.1 $^{19}$F NMR Results

To study the $^{19}$F NMR performance of the NMR system, PFOA and PFPA (see Figure 2.36) were used. Both of these substances are of increasing environmental and health concerns, because of their bioaccumulation and persistence in the human body and the environment [88][90].

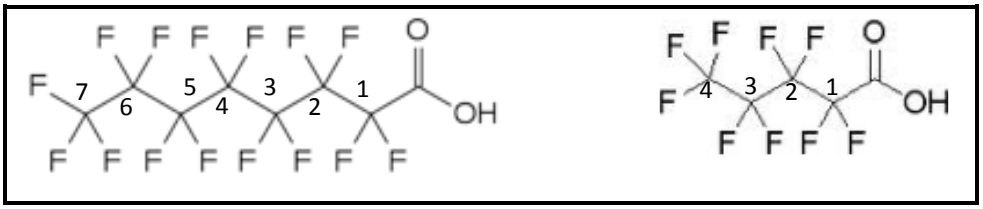


**Figure 2.36** Structural formula of PFOA (left) and PFPA (right)

Typical resolutions achievable with the NMR system are conveyed in Figure 2.37 a and b, which show two 4-scan averaged $^{19}$F NMR spectra of 0.5 M PFOA and 0.5 M PFPA, respectively, in a static 400 µm i.d. glass capillary. These $^{19}$F NMR spectra had a resolution of 0.2 ppm so that structural analysis was possible with the developed portable NMR system.
In the NMR spectrum of PFOA, the $CF_3$ peak (C7) at -84.5 ppm had a SNR value of 13 and the three $CF_2$ peaks (C1-C6) between -120 and -130 ppm had SNR values between 6 and 10. These SNR values were determined from the peak height and the RMS value of the variations in the baseline (see Equation 2.4). However, instead of detecting six individual $CF_2$ peaks, representing each $CF_2$ signal, just three $CF_2$ peaks can be distinguished. The peak at -120 ppm belongs to the $CF_2$ of C6, and the peak at -130 ppm presents the $CF_2$ signal of C1. The taller peak at -125 ppm is assigned to the four $CF_2$ peaks of C2-C5, as indicated by the increased peak area and the higher signal, because the amount of Fluorine atoms contributing to one peak is proportional to the peak area.

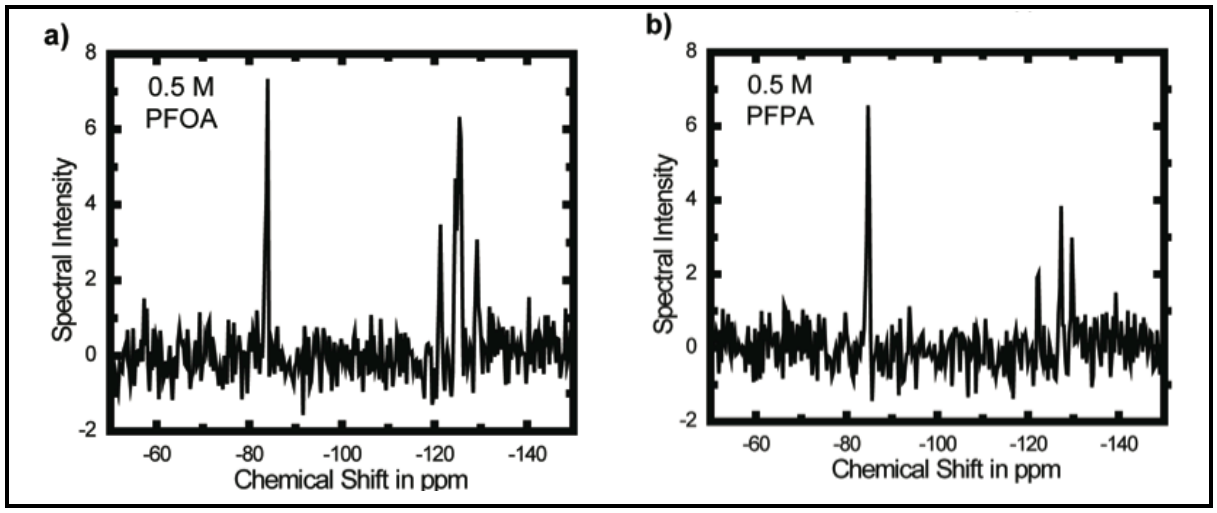


**Figure 2.37:** $^{19}$F NMR spectra using a 4 scan average of **a)** 0.5 M PFOA and **b)** 0.5 M PFPA; both samples were in a 400 µm i.d. tube (NMR parameters: 66.7 MHz, pulse width: 24 µs, points: 512, sweep width: 16 kHz, delay time: 1 s)

The PFPA NMR spectrum shows comparable results. The $CF_3$ peak (C4) at -84.5 ppm had a SNR value of 12 and the three $CF_2$ peaks (C1-3) between -120 and -130 ppm had SNR values between 4 and 7. All three individual signals of the $CF_2$ peaks were detected (C1 = -130 ppm; C2 = -127 ppm; C3 = -121 ppm), showing similar peak areas. Even though the peak at -121 ppm appears to have a lower signal height, due to the low SNR, the area is comparable to the two other peak areas at -130 ppm and -127 ppm.

Due to the structural differentiations between the $CF_2$ peaks both substances could be characterized and identified, so that a structural elucidation was possible.

To compare these portable NMR results to high field NMR spectra, the same sample substances were measured in a 500 MHz Bruker lab-scale NMR system, using 3 mm i.d. NMR tubes (see Figure 2.38).

The spectra of the portable NMR data provide comparable results to the high resolution NMR data even though the resolution is about 4 orders of magnitude better in the lab-scale system. These experiments demonstrate that the miniaturized NMR system is capable of performing $^{19}F$ NMR measurements of molecules containing different $^{19}F$ atoms at moderate concentrations for a structural elucidation.

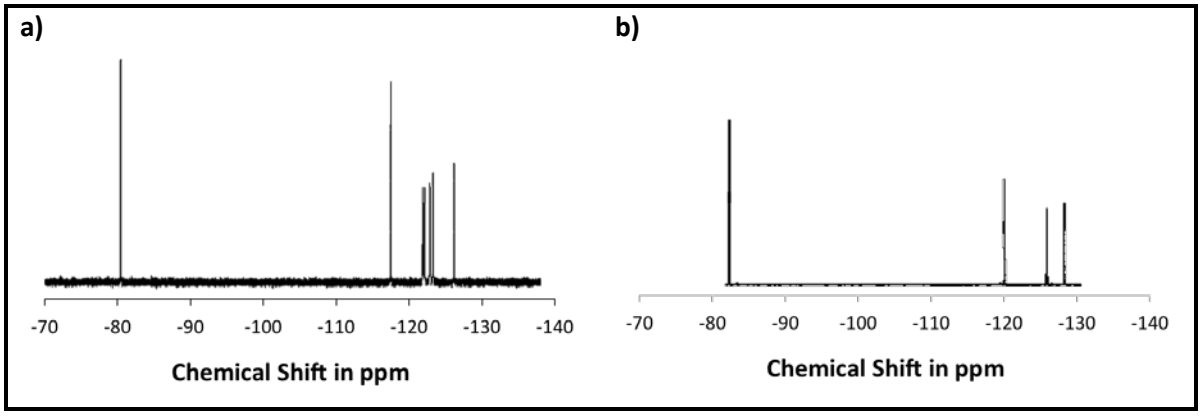


**Figure 2.38:** $^{19}F$ NMR spectra of **a)** 0.5 M PFOA and **b)** 0.5 M PFPA at 500 MHz, in a 3 mm i.d. NMR tube (internal reference: 2,2,2-trifluorethanol in acetone-$D_6$)

### 2.2.6.2 $^{1}H$ NMR Results

The improved spectral resolution demonstrated with the new miniaturized NMR system is sufficient for performing $^{1}H$ NMR spectroscopy, in contrast to the portable NMR presented in earlier research work [16][63].

Below, sample spectra of water, citric acid, acetic acid and ethanol, all having very good water solubility as well as no toxic concerns, are presented in different concentrations and sample capillary sizes. Due to the limited size of the homogeneous region in the magnet (see Chapter 2.2.3), the sample size in the capillary is expected to impact spectral resolution. Larger sample capillaries occupy a bigger region in the magnet and hence the sample substance is more sensitive to inhomogeneities in the field of the NMR magnet, but a stronger NMR signal is detected due to the larger amount of observable sample volume. Those inhomogeneities cause line broadening and so there is an upper limit on sample volume for

any desired level of NMR resolution. For higher resolution NMR spectra, smaller sample sizes have to be used which are less sensitive to the inhomogeneities in the magnetic field, but lead to weaker NMR signals.

In the beginning two different sample capillary sizes were used with $V_{observ}$ = 4 nL (capillary i.d. = 75 µm) and $V_{observ}$ = 125 nL (capillary i.d. = 400 µm) to investigate in the NMR resolution. Figure 2.39 shows the spectra of a pure $H_2O$ sample (55 M) measured in the 400 µm i.d. capillary and in the 75 µm i.d. capillary using the same RF coil (see Chapter 2.2.2.3). The secondary spectral features in the NMR spectrum with the 400 µm i.d. capillary are 60 Hz sidebands caused by ripple in the shim coil current.

The $^1$H NMR spectrum of the small sample in the 75 µm i.d. capillary has a narrow NMR signal with a FWHM of 1.5 Hz (0.02 ppm) and an approximately 50 fold lower peak height than in the larger sample. In contrast to that, the spectrum taken in the 400 µm i.d. capillary shows a resolution loss of 10 times (FWHM = 15 Hz and 0.2 ppm), due to the larger sample volume, so that some of the finer structures in the $^1$H spectra will not be resolved in the NMR data when multiple NMR signals are closer together. The sensitivity effect due to the use of different sample sizes is explained in Chapter 2.3.3.1.

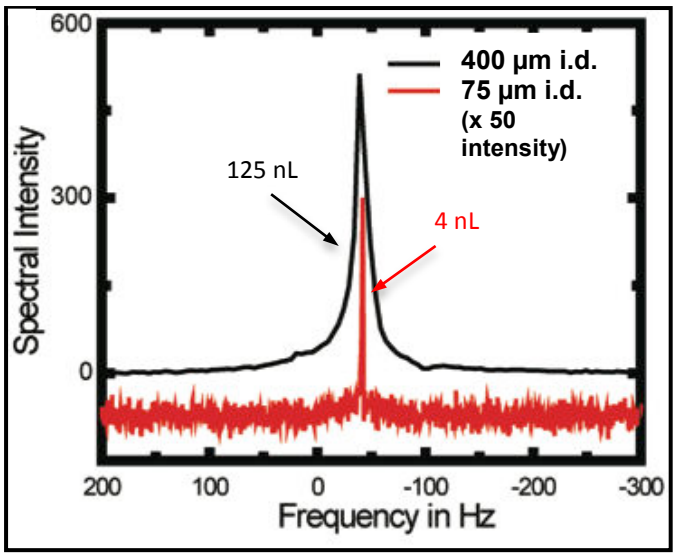


**Figure 2.39:** Overlay of two $^1$H NMR single scan spectra of pure $H_2O$ (55 M) taken in a 75 µm i.d. capillary (red; shifted vertically for clarity and multiplied by factor 50) and in a 400 µm i.d. capillary (black) (NMR parameters: 70.9 MHz, pulse width: 24 µs, points: 512, sweep width: 4 kHz)

These experiments show the resolution capability of the portable NMR system, even for large sample amounts (*e.g.* 125 nL). Since the larger i.d. capillaries will be used in the NMR system, it was important to prove that even these sample sizes will still allow sufficient $^1$H NMR spectroscopy.

All the above experiments were done using the highest possible sample concentration, which is an unrealistic situation for NMR spectroscopy of sample substances. Therefore, the following results show data taken on diluted samples and sample mixtures using the 400 µm i.d. capillary.

The first example of these diluted sample $^{1}H$ NMR spectra is shown in Figure 2.40 a using a 0.9 M acetic acid and 1 M citrate acid mixture. Both substances provide one single NMR peak in the resulting spectrum. The single scan NMR spectrum shows a complete baseline separation between the citrate peak and the $H_2O$ peak, which are 2.2 ppm apart. The resolution between the acetic acid and the citrate is enough to observe the two distinct peaks, which are 0.6 ppm apart. These two peaks have SNR values of 25 and 20, respectively. Furthermore, a 0.3 M (= 7 µg in 125 nL) citrate sample was detected in using a single scan NMR experiment to demonstrate the sensitivity of the portable NMR system (see Figure 2.40 b). However, the shim adjustment was not as optimized as for the 1 M $^{1}H$ spectrum, as evidenced by the increased width of the $H_2O$ peak, which shows intensity at the citrate frequency. Though, the experiment shows the enhancement in NMR sensitivity, comparing to the reported sensitivity by Diekmann of 0.4 to 0.8 M of a fluorinated sample with at least 32-scan averages [63].

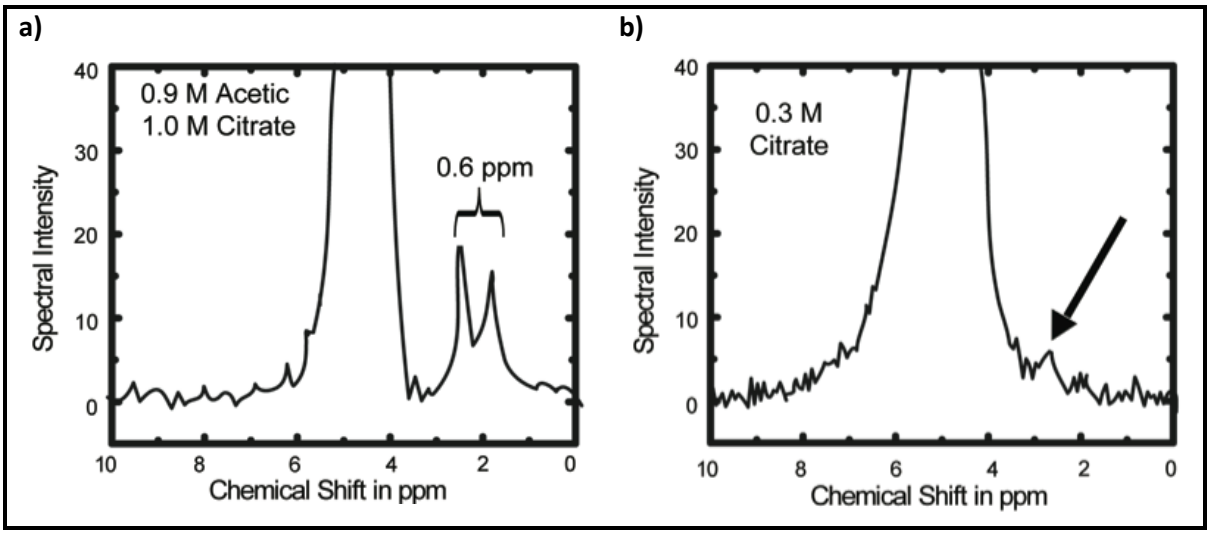


**Figure 2.40:** $^{1}H$ NMR single scan spectra of **a)** 0.9 M acetic acid / 1 M citrate acid mixture and **b)** 0.3 M citrate solution (see arrow) in a 400 µm i.d. capillary (NMR parameters: 70.9 MHz, pulse width: 24 µs, points: 512, sweep width: 4 kHz)

Furthermore, these results prove, that under optimized conditions, the use of common aqueous CE buffer solutions, in contrast to expensive deuterated CE buffers, is possible once the NMR is hyphenated to the CE system, if the loss of spectral information in the 3.8-5.8 ppm chemical shift (= $H_2O$ peak) range can be tolerated. Especially for the coupling experiments, this information is very important to know.

Figure 2.41 presents another example, a pure ethanol $^{1}H$ NMR spectrum taken in a 400 µm i.d. capillary. The spectrum almost shows baseline resolution for all three peaks and a resolution of 0.4 ppm (FWHM) is achieved on the $CH_3$ peak at 1.2 ppm. Due to the limited resolution achievable in the 400 µm sample container (see Figure 2.39), the ethanol *J*-couplings (5 to 10 Hz = 0.07 to 0.14 ppm) were not seen in this spectrum.

Although the $^{1}H$ and $^{19}F$ NMR results shown here and in the previous section are not as good as the spectra detected with traditional high-field systems (see $^{19}F$ NMR comparison), the NMR performance of the portable NMR has been improved.

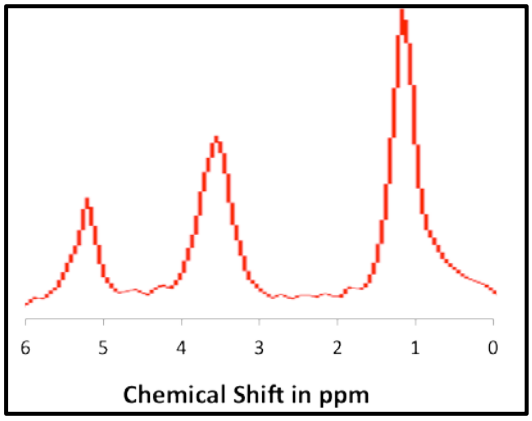


**Figure 2.41:** $^{1}H$ NMR single scan spectra of pure ethanol in a 400 µm i.d. capillary (NMR parameters: 70.9 MHz, pulse width: 24 µs, points: 512, sweep width: 4 kHz)

### 2.2.6.3 NMR Peak Shape

Besides NMR resolution and sensitivity, the peak shape is as well an important parameter in NMR spectroscopy. In an ideal case, the Fourier Transform of the FIDs will result in a Lorentzian peak shape, as would be expected in a liquid state NMR experiment. These Lorentzian line shapes can be expressed mathematically and consist of three parameters: 1) peak amplitude, 2) FWHM, and 3) peak position [71]. An example of this peak shape study is shown in Figure 2.42 using a pure $H_2O$ NMR signal, measured in a 400 µm i.d. capillary and analyzed using a Lorentzian peak fitting.

The diagram shows, that the Lorentzian peak profile can be fit to the $H_2O$ peak. Only the peak shoulders show slightly different curves. However, both signal peaks overlap to 90 % with a FWHM of 70 Hz. This result shows that the NMR peaks have good resolution and sensitivity as well as proper shapes.

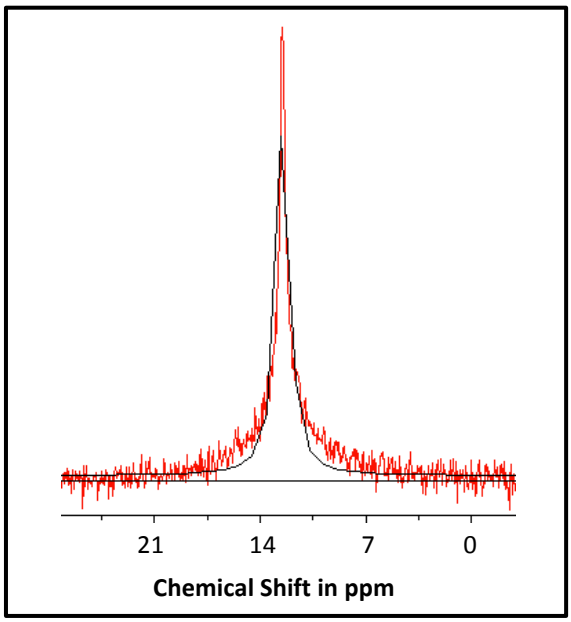


**Figure 2.42:** $^{1}H$ NMR single scan spectra (red) of pure $H_2O$ in a 400 µm i.d. capillary analyzed with a Lorentzian peak fitting curve (black) (NMR parameters: 70.9 MHz, pulse width: 24 µs, points: 512, sweep width: 4 kHz)

## 2.3 Flow Cell Capillary

In the CE-NMR device with the small permanent magnet the balancing of sample volumes and concentrations between CE and NMR is challenging [16]. On the one hand, typical CE experiments have maximum analyte concentrations of 10 mM, 50-100 µm i.d. separation capillaries and sample volumes in the low nL range. CE capillaries with larger internal diameters are not desirable due to the increased current and Joule heating effects that degrade the CE separation. On the other hand, even though microcoil NMR has been developed for sample volumes down to 5 nL [72], the concentrations have to be very high (100 mM to 1 M) at these small sample sizes. For microcoils operated in low field permanent magnets, the samples are typically pure liquids (ca. 20-55 M). Therefore, to detect lower concentrations in permanent magnets, larger sample volumes of 100-200 nL are necessary, requiring capillaries with an i.d. of 350 to 500 µm, since the NMR detection coil has a length of about 1 mm. An attempt to address this balancing act is to use a capillary which has a small overall i.d. of *e.g.* 75 µm, which matches the CE requirements, and a 1 mm long extended i.d. of *e.g.* 400 µm in the NMR coil region to increase the active sample volume for the NMR detection. Figure 2.43 a shows an example of these flow cell capillaries which achieve a compromise between the requirements of CE and NMR. These capillaries are also known as bubble-cell capillaries [40], when the extended capillary part has the shape of a bubble (see Figure 2.43 b).

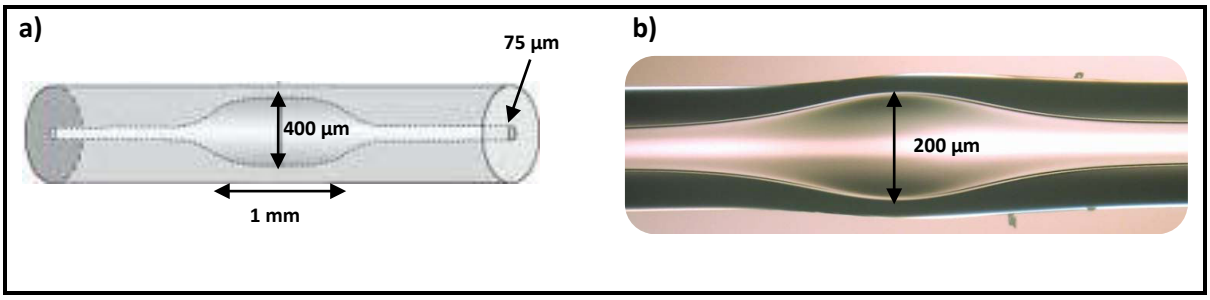


**Figure 2.43: a)** Schematic of flow cell capillary with extended i.d. [73] and **b)** picture of commercially purchased bubble-cell capillary (G1600-61332, Agilent Technologies, Santa Clara CA, USA) fabricated with glass lathe technique described in [74] (capillary i.d. 75 µm; bubble-cell i.d. 200 µm)

Flow cell capillaries can be purchased commercially (see Figure 2.43 b); however, the available capillaries will have fixed positions and sizes for the localized region of increased diameter. Therefore, it is a great advantage to manufacture those flow cell capillaries in the own lab and use the appropriate dimensions and sizes, needed for the integrated CE-NMR instrument setup. Different techniques are known to construct these customized capillaries, including 1) mechanical glass blowing techniques, such as the glass lathe technique [74][75][76], 2) wet, chemical HF etching [70][77][78][89] or a simple 3) mechanical gluing technique. The latter two techniques are employed during this research work and are explained in detail in the following chapters.

### 2.3.1 Chemical HF Etching Technique

To produce a flow cell capillary using the wet chemical method, HF is used to etch a defined space in the capillary, by using heating and cooling systems to precisely confine the flow cell along the capillary. Thereby, HF reacts with the fused-silica of the capillary:

$$SiO_2 + 4\ HF \rightarrow SiF_{4\ (g)} + 2\ H_2O$$

This reaction is catalyzed by heat and etching is much slower in cooled capillary regions.

#### 2.3.1.1 Experimental Setup

For chemical HF etching of a fused-silica capillary (i.d./o.d. = 50/360 µm) a method similar to the one described by Mosulishvili et al. [70] and modified by Mohamed et al. [79] was used (see Figure 2.44). For this purpose, the capillary (2) was placed in an ice bucket (3) and water vapor (5), produced by boiling water in a flask, was passed through a silica tube with an i.d. of 1 mm (4) for 30 min to attain equilibrium between the heated and the cooled parts of the capillary. This tube localized the heat due to a defined hole which accommodated the capillary (6), and heated only this 1 mm long region of the capillary. Therefore, the flow cell could be produced at any spot of the capillary, depending on the experimental parameters.

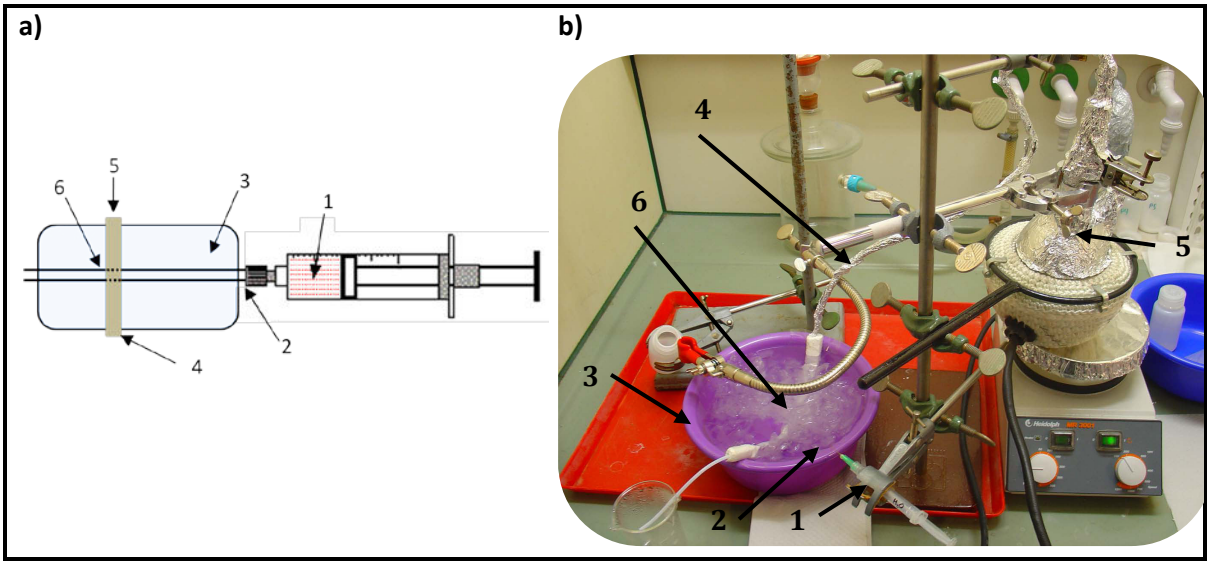


**Figure 2.44: a)** Schematic diagram and **b)** picture of the lab setup for the HF etching device: 1) 30 % HF solution in syringe, 2) capillary, 3) plastic box with ice water, 4) silica tube (i.d.: 1 mm) with little hole for capillary, 5) water vapor going in the tube, and 6) position of flow cell [79]

Then a syringe with 30 % HF solution (1), which was cooled to 4°C, was forced through the capillary. The flow velocity of the HF was kept constant, at 2 HF drops per 10 min during the etching process. Different amounts of HF were used during the optimization of the HF etching process, to see the changes in the resulting flow cell shapes and dimensions [79]. After the etching process a 0.1 M NaOH solution was immediately forced through the capillary for surface activation, followed by water and air to dry the capillary.

#### 2.3.1.2 Characteristics of the Flow Cell

The experiments in the previous section showed that the fabrication of a flow cell capillary using the chemical HF etching method was possible and different parameters were used to characterize the resulting flow cell capillary.

Since the whole capillary was flushed with HF, it was important to investigate in the capillary i.d. not only in the heated, flow cell, region but also along the cooled parts of the entire capillary, which were in the ice bucket to prevent the capillary from being etched by the HF. To measure the i.d., the capillary was placed under the digital microscope (VHX-600DSO, Keyence, Osaka, Japan). However, it is important to know that the measured i.d. of the capillary under the microscope is always bigger than the actual i.d., since the refractive index ($n$) of the fused-silica ($n = 1.458$) has to be considered [79]. The measured HF etched capillaries showed a constant i.d. of $50 \pm 4$ µm, which was very smooth and would not cause turbulent flows in the capillary or excessive sample plug broadening.

It is also important to maintain the shape of the etched flow cell, which should be as symmetrical as possible in order to get reproducible CE separations. However, as seen in Figure 2.45 the cell was not symmetrical, having a much faster cell opening on the left side, than the wider opening on the right side. The shape was a result due to the warm HF, which left the cell on the right outflow side, so that the etching in this region was more prominent, than at the cell entrance on the left side. However, since the NMR coil was just 1 mm long it was important to examine the flow cell shape in this 1 mm long region. The i.d. of the flow cell did not change more than $\pm$ 5 µm over a 1 mm length, meaning that the part of the flow cell which would be in the NMR coil yielded a constant NMR coil filling.

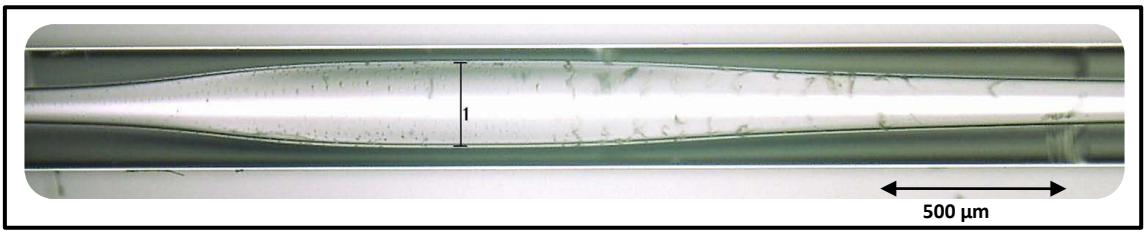


**Figure 2.45:** Picture of HF etched flow cell [79]

Furthermore, the reproducibility of this etching method was shown by running five consecutive experiments using new capillaries for every run and a 20 min HF etching process but leaving the same experimental setup. The flow cell i.d. of the different etched capillaries varied between 126 µm and 154 µm, whereas the lengths of the flow cells were between 1.7 mm and 2.5 mm. The calculated bubble factor, which is the quotient of the flow cell i.d. and the capillary i.d., presents the amount of the i.d. enlargement due to etching. It could be calculated to be between 2.8 and 3.8.

These parameters show that the reproducibility of this flow cell fabrication using HF etching is not straightforward and a lot of different influencing factors have to be considered during this etching technique. For this reason, along with the dangerous handling of HF, the time consuming etching and rinsing steps, as well as the unpredictable flow cell shape, another fabrication technique was developed.

Although these etched flow cell capillaries were not used for further applications in the integrated CE-NMR setup presented in this work, CE separations of a xanthine mixture (caffeine (0.1 mg/l), theobromine (0.1 mg/l), theophylline (0.1 mg/l), xanthine (0.05 mg/l)) were performed on the commercial P/ACE MDQ CE system to show that this etched flow cell could be used in principle. Figure 2.46 shows the comparison of two electropherograms, one taken with a 50 µm i.d. fused-silica capillary and the other one taken with an etched flow cell capillary (i.d. = 150 µm) [79].

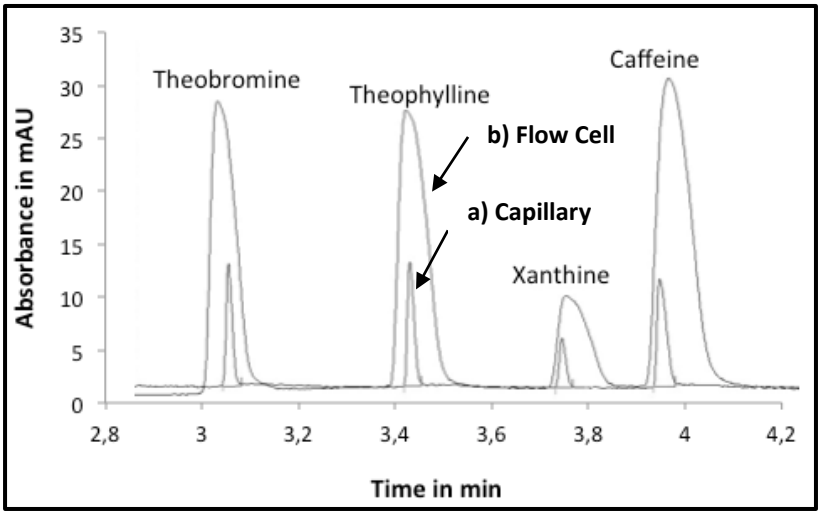


**Figure 2.46:** Comparison of two electropherograms taken with **a)** 50 µm i.d fused-silica and **b)** an etched 150 µm i.d. flow cell capillary on the commercial P/ACE MDQ CE system (xanthine mixture: caffeine (0.1 mg/l), theobromine (0.1 mg/l), theophylline (0.1 mg/l), xanthine (0.05 mg/l), 50 mM borate buffer with 100 mM SDS (pH 8.25), 50 cm long capillary, 42 cm to detector, 3 s injection with 34.5 mbar (3447 Pa), 30 kV, 214 nm) [79]

The results demonstrate that the extended capillary path of the flow cell, which was located in the UV/Vis detection window, did not influence the resolution of this CE separation. Note, with closer migration times of the individual substances, the CE separation would be influenced. Due to the increased sample volume at the UV/Vis detection, the sensitivity of the CE experiment was enhanced by a factor of 6 to 10, comparable to the 9 times larger observable volume. These results were promising, which led to further developments using different techniques to manufacture the flow cell capillaries used in this research work.

### 2.3.2 Mechanical Gluing Technique

The ultimate goal of this thesis work is to develop an integrated CE-NMR system which implies an appropriate flow cell capillary to demonstrate the instrument capabilities. The mechanical gluing technique described below is a simple approach to fabricate a robust, low-cost, and flexible flow cell to provide an enhanced sample volume for the NMR detection within the small i.d. CE capillary. However, this flow cell is not a finished product and still needs further improvement and development to achieve an ideal flow cell capillary. Discussions of the parameters required for the flow cell, in terms of the CE separations and the NMR detection are included in this section.

#### 2.3.2.1 Experimental Setup

The flow cell capillaries were fabricated by gluing two pieces (45 cm and 20 cm) of fused-silica capillaries (i.d./o.d. = 75/360 µm) into either end of a 5 mm long 400 µm i.d. (550 µm o.d.) synthetic fused-silica glass tube (CV4055s, VitroCom, Mountain Lakes, NJ, USA), using a "5-minute" two component epoxy. This gluing process of the flow cell capillary took place under a light microscope for precise working [42].

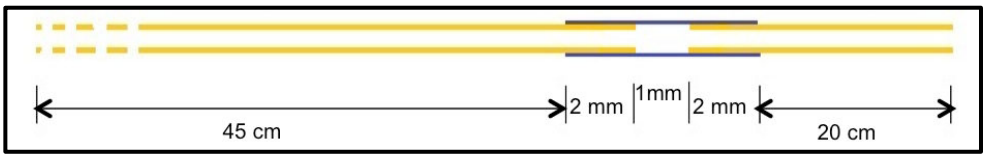


**Figure 2.47:** Schematic of customized mechanical glued flow cell capillary [42]

The capillary gluing resulted in a 1 mm long detection cell located at 45 cm along the overall capillary (see Figure 2.47). The capillary lengths shown in the schematic figure matched the miniaturized CE-NMR setup, so that UV/Vis and NMR detection could be used at the same time during an experiment.

#### 2.3.2.2 Characteristics of the Flow Cell

These glued flow cell capillaries (see Figure 2.48) were well suited for the use in the portable CE-NMR, because different capillary sizes could be chosen individually to match the special instrument requirements, and their construction was reproducible and uncomplicated.

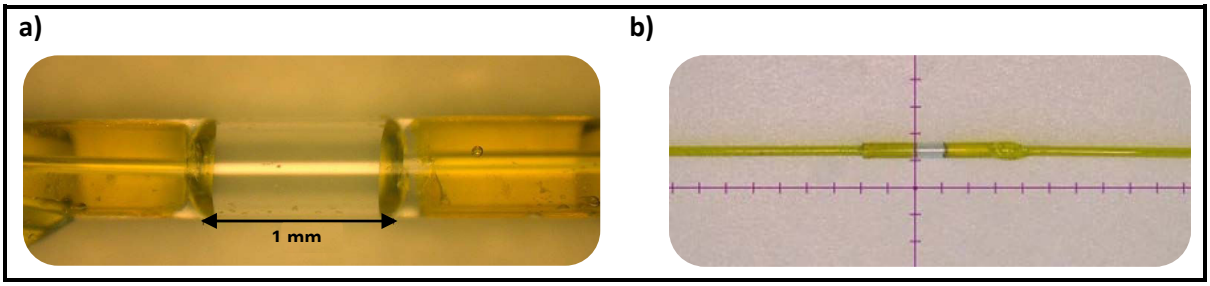


**Figure 2.48:** Microscope pictures of the 1 mm long customized glued flow cell (i.d. 400 µm) within a 75/360 µm i.d./o.d. fused-silica capillary **a)** close up of flow cell and **b)** flow cell capillary (1 mm per division on scale) [42]

The parameters and characteristics of the flow cells are summarized in Table 2.13 and are compared to a normal fused-silica capillary with an i.d. of 75 µm.

**Table 2.13** Parameters of the glued flow cell compared to a normal fused-silica capillary

| Type | Cell i.d. in µm | Cell o.d. in µm | Cell length in mm | Bubble factor | Cell volume in nL | Volume increase |
|---|---|---|---|---|---|---|
| Normal | 75 | 360 | 1 | 1 | 4 | 1 |
| Flow cell | 400 | 550 | 1 | 5.3 | 125 | 31 |

For the fabrication of the flow cells, two different glass tube materials, borosilicate (CV4055) and synthetic fused-silica (CV4055s), were tested, in order to evaluate their material performance. Due to different surface characteristics of the two glasses and the physical-chemical interactions with sample material, the synthetic fused-silica material was used for the flow cell construction in this work [42]. Using fused-silica for the flow cell had the further advantage of not adding another material in the capillary, since the 75 µm i.d. CE capillary was made of fused-silica, too.

The pictures in Figure 2.48 show that the resulting flow cell had a cylindrical shape, in contrast to the more oval shape of the HF etched flow cell capillary. Therefore, it was important to take a look at the capillary flow profiles in order to see possible memory effects of sample residues in the corners of the flow cell.

#### 2.3.2.3 Migration Characterization of Glued Flow Cell Capillary

Flow profiles of the glued capillaries were monitored visually using the digital microscope (VHX-600DSO, Keyence, Osaka, Japan) and pressurizing a blue hydrophilic ink plug through the capillary (see Figure 2.49) surrounded by colorless hydrophobic organic solvent (methyl isobutyl ketone (MIBK)), to provide sharp contrasts between the ink and the background [42].

**Figure 2.49:** Schematic setup of the flow profile monitoring [42]

Note, these substances were only used for demonstration purposes to provide a sharp plug flow within the capillary and the glued cell. The syringe pressurized migration profile of the flow cell capillary, shown in Figure 2.50, presents a parabolic and very homogeneous sample plug profile throughout the flow cell.

No turbulent flows or bubble formations, which would lead to sample mixing, were seen along the edges of the flow cell. However, a little bit of ink remained at the edges of the flow cell, where it contacted the epoxy. These ink contaminations could easily be washed out using water, so that this memory effect could be caused by physical or chemical characteristic properties of the ink and the epoxy. To investigate these ink remains, the epoxy was exposed to the blue ink for 10 min and then washed away with MIBK. No noticeable ink remained on the epoxy surface. However, when the epoxy was covered with organic MIBK solvent for 1 h, followed by a 10 min ink exposure, before the ink was washed away with MIBK, a noticeable amount of ink remained on the epoxy. This indicated that the organic solvent interacts chemically and/or physically with the epoxy, *e.g.* creating pores or changing the surface of the epoxy, so that the ink remaining in the flow cell capillary could be a result due to these interactions between the epoxy and the organic solvent.

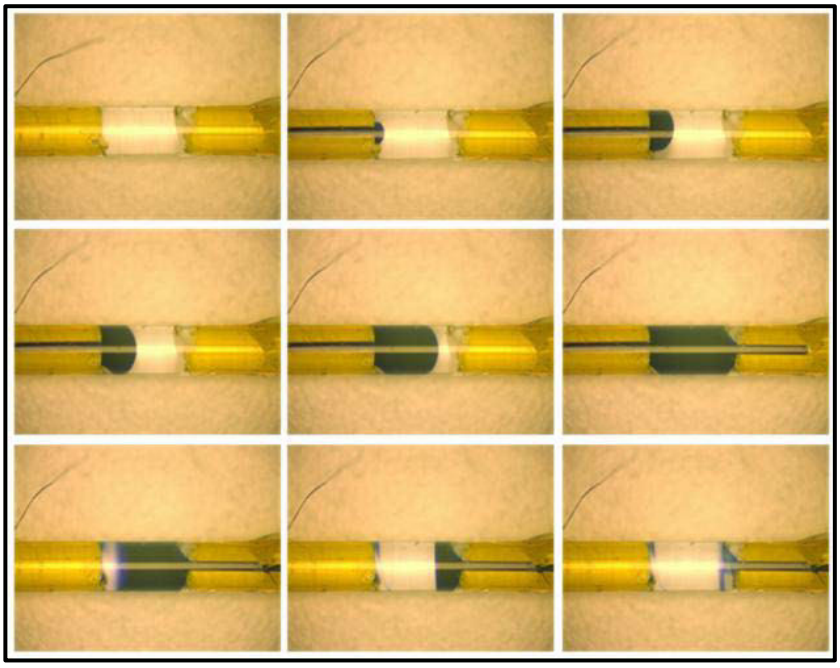

**Figure 2.50:** Pictures of the monitored flow profile in the glued fused-silica flow cell capillary (cell i.d./o.d. = 400/550 µm) with syringe pressurized flow of a blue ink sample plug and MIBK as organic solvent (magnification 100 times) [42]

In addition, the same flow cell capillary was used multiple times to see if the amount of memory effect changed after several fillings. These effects did not increase significantly with more capillary fillings [42].

Another factor which could cause ink trapping in the flow cell was the geometry influence of the glued cell. Since both of the flow cell sides were never glued in exactly the same way, differences in the resulting glue shape could manipulate the flow cell performance. Therefore, one flow cell was separately filled with the ink plug and pressurized through the capillary, using MIBK, from either side of the capillary end (see Figure 2.51). As demonstrated in the pictures, no influences caused by the geometry of the flow cell were seen, so it did not matter from which direction (long or short capillary side) the ink was injected. In both experiments more ink residue remained on the outgoing side of the flow cell [42].

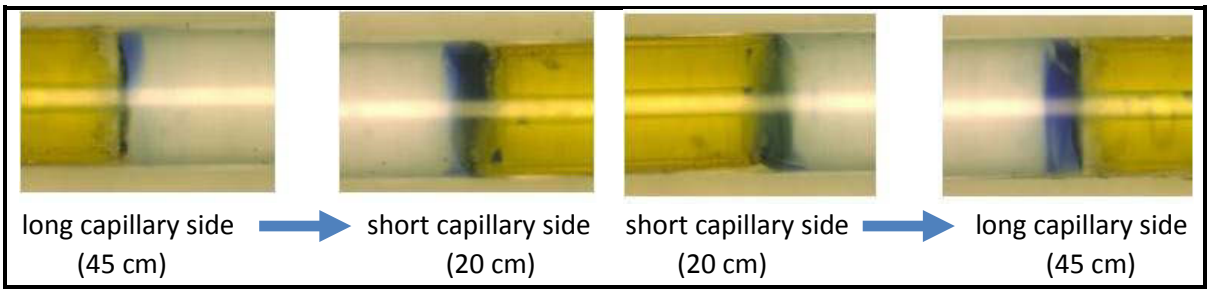


**Figure 2.51:** Pictures of monitored geometry influences in the fused-silica flow cell capillary (cell i.d./o.d. = 400/550 µm) using syringe pressurized blue ink and filling from the long and the short side of the capillary (magnification 100 times) [42]

However, the above experiments ensured that careful and symmetrical flow cell gluing was important to minimize sample remains in the cell, including:

1) Epoxy glue should not be in the flow cell,
2) No empty space between large and small i.d. capillary
3) Smooth and well cut capillary edges

To show the performance of these glued flow cell capillaries during NMR and CE experiments, the next chapter summarizes important characteristics during this testing.

### 2.3.3 NMR and CE Performance of Glued Flow Cell Capillary

The flow cell capillaries in the CE-NMR setup have to meet certain requirements, including, electrical conductivity, no air bubble formation, robustness, and magnetic field homogeneity. The mechanical and chemical robustness of the flow cells was tested by using syringe flushes of 1 M NaOH. No material failures, especially in the glued parts of the capillary, were visible after several capillary fillings with the NaOH. In addition, sometimes formed air bubbles in the flow cell led to an NMR signal loss and peak shape degradation, as well as a decrease in the CE current, so that these bubbles could be detected right away. The air bubbles could be removed by flushing the flow cell with isopropyl alcohol (IPA) or ethanol.
Further characteristics of the flow cell capillaries and their CE and NMR performance are presented in the sections below.

#### 2.3.3.1 NMR Performance of Flow Cell Capillary

An important aspect of the flow cell capillary was the effect of the cell structure on the homogeneous magnetic field, since the cells had the same length as the NMR RF coil (see Figure 2.52).

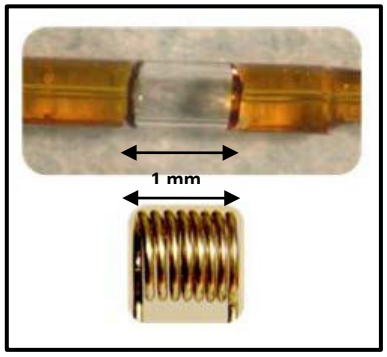


**Figure 2.52:** Pictures of flow cell capillary and NMR RF coil

Figure 2.53 shows two separate $^{1}H$ NMR spectra of pure $H_2O$ (55 M), one from a 10 cm long sealed fused-silica capillary that had the same i.d. and o.d. as the flow cell, and another one from the flow cell itself. The spectra just show minor differences due to shimming effects for the peak shapes and linewidths in the bottom part of the peak, but no significant changes in the NMR resolution, therefore, the FWHM. These results indicate that the flow cell structure

did not influence the homogeneity of the $B_0$. This result proves that the flow cell capillary is well suited for the NMR application and can be employed to address the volume requirements for the CE and the NMR experiment.

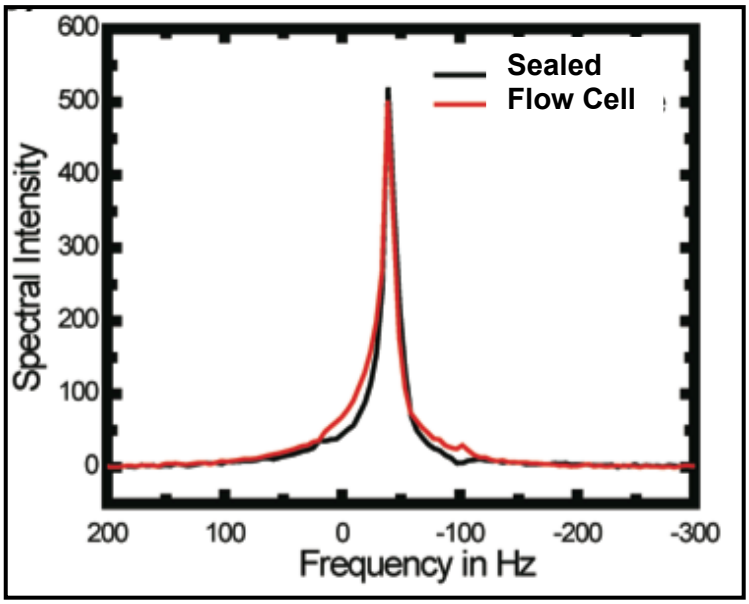


**Figure 2.53:** Comparison of two $^1$H NMR single scan spectra of pure $H_2O$ (55 M) taken in a 10 cm long, 400 µm i.d. sealed capillary (red) and a 400 µm i.d. flow cell capillary (black) (NMR parameters: 70.9 MHz, pulse width: 24 µs, points: 512, sweep width: 4 kHz)

By positioning the flow cell capillary within the NMR detection coil, a reasonable increase in the SNR and an improved concentration sensitivity of the NMR data should be seen compared to the normal 75 µm i.d. capillary. Figure 2.39 (see Chapter 2.2.6.2) presents this gain in sensitivity of the flow cell, which is approximately $50 \pm 3$ times (three consecutive experiments). However, the increase of the sample volume in the flow cell is just 31 times, meaning that the improvement in NMR sensitivity is not simply due to the bigger active sample volume in the NMR coil. The other contribution, which is non-linear, involved in the SNR is the coil filling factor ($f$) which presents the fraction of the coil detection volume filled with sample ($f$ = (i.d. sample cell/i.d. NMR coil)$^2$). To enhance the sensitivity in a NMR experiment this $f$ should be as high as possible. The NMR coil used for the flow cell had an $f$ of about (400 µm/690 µm)$^2$ = 34 %. In contrast, the small i.d. non-flow cell capillary provided an $f$ of roughly (75 µm/690 µm)$^2$ = 1 % using the same RF coil in the NMR setup, as presented in the experiment. These significant differences in $f$ explain why the detected sensitivity gain ($50 \pm 3$ times) is almost twice as high as expected, considering the increased sample volume of 31 times, because $f$ contributes to SNR non-linear.

As presented above, the glued flow cell capillary showed a significant improve in the NMR concentration sensitivity performance and did not lead to inhomogeneous magnetic fields in the NMR detection due to its structure.

#### 2.3.3.2 CE Performance of Flow Cell Capillary

When using the flow cell capillaries in the CE instrument two essential parameters, had to be investigated: The flow cell capillary should maintain the CE separation, either in terms of sample mixing or resolution loss, and the Joule heating effects during the CE separation should be analyzed.

Hence, it was important to confirm, that the glued flow cell capillary did not affect the electrophoretic current running through the CE capillary, because $I$ depends on the voltage and the electric resistance, including the capillary i.d., its length, as well as the electrolyte conductivity ($\kappa$):

$$U = I \cdot R = I \cdot \sum R = I \cdot \sum \frac{4\,L}{\text{i.d.}^2 \cdot \pi \cdot \kappa} = I \cdot \sum \frac{L}{\text{i.d.}^2} \cdot const. \qquad \text{Equation 2.5}$$

$L$ and i.d. are the only variables in Equation 2.5, so that all the other parameters can be summarized in a constant term to simplify the calculation for the electrical resistance [40]:

$$R \sim \sum \frac{L}{\text{i.d.}^2} \cdot const. \qquad \text{Equation 2.6}$$

As stated in Equation 2.6 the electrical resistance depends only on the capillary characteristics. Equivalent circuits shown in Figure 2.54 model the different resistances in the capillaries which are connected in series.

The calculation of the total resistances ($R_{\text{total}}$) show that the flow cell within the small i.d. capillary should not affect the current running through the capillary. The electrical resistance of the entire flow cell capillary only changed by 0.04 ‰ compared to the normal capillary, because the resistance of the flow cell was very low. Therefore, this added resistance from the flow cell was negligible and the CE current should not change at a given voltage.

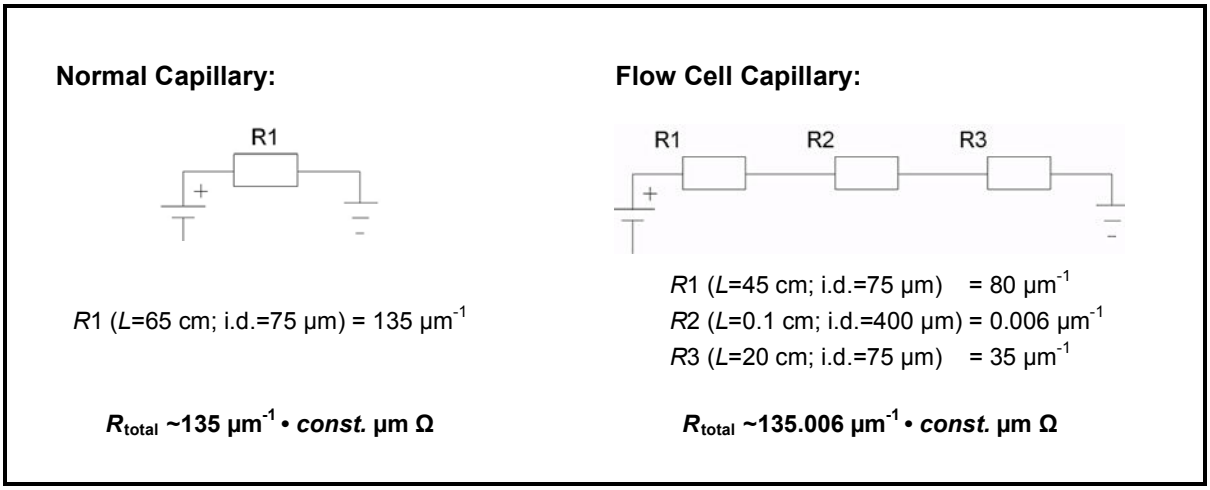


**Figure 2.54:** Equivalent circuits for the normal and the flow cell capillary including the parameters for the electrical resistance calculations.

To prove these theoretical assumptions, the current was monitored during different CE separations using various voltages. No changes in the current values and no current flow fluctuations were noticeable. A constant electrophoretic current was measured during the

repeated use of the capillary at up to 25 kV. These results were coherent with the theoretical approach discussed above.

Furthermore, the Joule heating effects were studied using an Ohm's Law Plot (see Chapter 2.1.5). As stated in Equation 2.2 the capillary cross section inversely influences the generated heat. Inserting a 1 mm long flow cell with a 5 times larger i.d. into the normal CE separation capillary, changes in the Joule heating were expected.

Therefore, the Ohm's Law Plot experiments presented in Chapter 2.1.5 were repeated on the commercial and the portable CE instrument, using the flow cell capillaries (56 cm long) as well as the 25 mM phosphate buffer (pH 2.5) solution. Figure 2.55 compares these flow cell results with the previous ones, which were taken on a normal 75 µm i.d. (56 cm long) capillary (see Chapter 2.1.5).

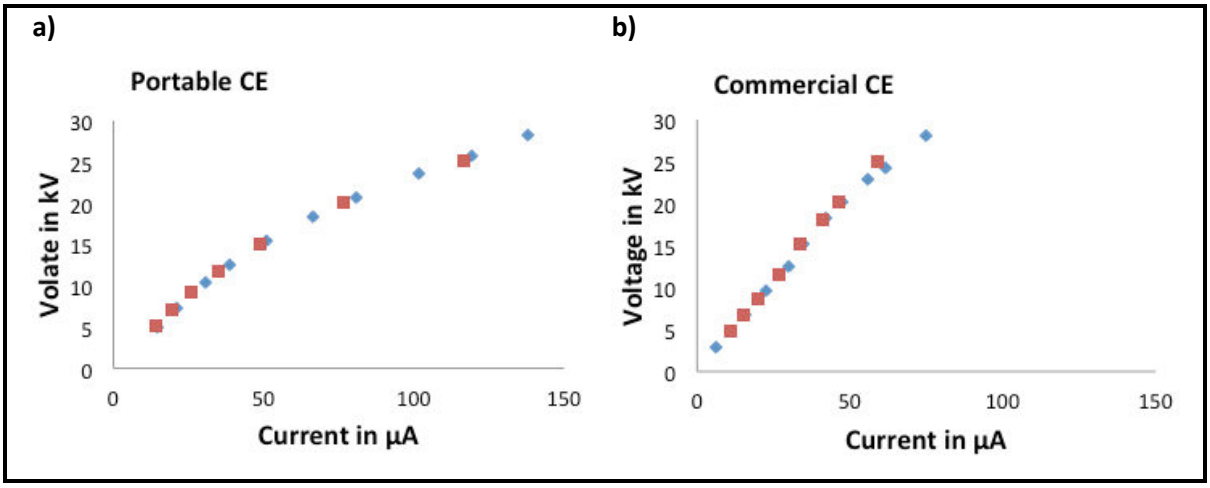


**Figure 2.55:** Ohm's Law Plots of 25 mM phosphate buffer (pH 2.5) solution taken in the **a)** portable CE and **b)** commercial CE using a flow cell capillary (blue) and a normal capillary (red) (56 cm long fused-silica capillary with/without flow cell, i.d./o.d. = 75/360 µm) [42]

It can be seen that both capillary types showed almost identical behaviors during the experiments, indicating that the flow cell capillaries did not disturb the CE current as well as they did not increase the Joule heating. However, the portable CE system still generated a larger amount of Joule heating, resulting in higher currents, than compared to the commercial system, due to the lack of a sufficient cooling system.

These results prove that the same CE separation voltage can be used for the flow cell CE experiments; since the Ohm's Law Plots had an identical shape as the ones taken with the normal capillaries (see Chapter 2.1.5).

Additionally, the flow cell capillary needed to be investigated regarding its CE separation performance. Two different experimental setups were used to study the actual sample behavior before and after the flow cell. Figure 2.56 schematically demonstrates how the flow cell was arranged in regard to the UV/Vis detector, which was used for the CE detection. In this way, the separated samples were monitored before entering the flow cell (see Figure 2.56 b) and after leaving the flow cell (Figure 2.56 a).

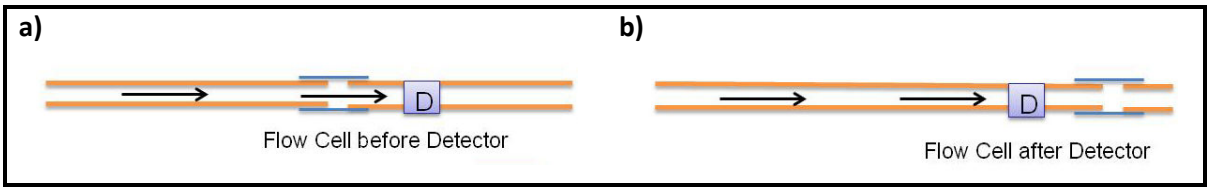


**Figure 2.56:** Schematic arrangements of the flow cell during the CE experiments [42]

Figure 2.57 presents a CE separation of glycyl-glycin and TFA at 250 mM (further examples presented in [42] and [46]) using both, the flow cell and the normal capillary for comparison. The data shows the flow cell influence of the sample separation. No differences during the CE separation were present before the sample mixture entered the flow cell, since the run overlays perfectly with the CE separation using a normal capillary. However, when the sample plug was monitored after the flow cell, a significant loss in CE resolution was detected. The faster migration times of the analytes were due to the shorter traveling distance of the sample, as a result of the experimental setup. The TFA sample migrated about 15 min faster compared to the CE separation with a normal capillary. This loss in resolution was due to the sample expansion in the flow cell, since the capillary i.d. in the cell was much bigger. Although the samples migrated closer to each other after leaving the flow cell, the peak shapes and peak widths still appeared identical.

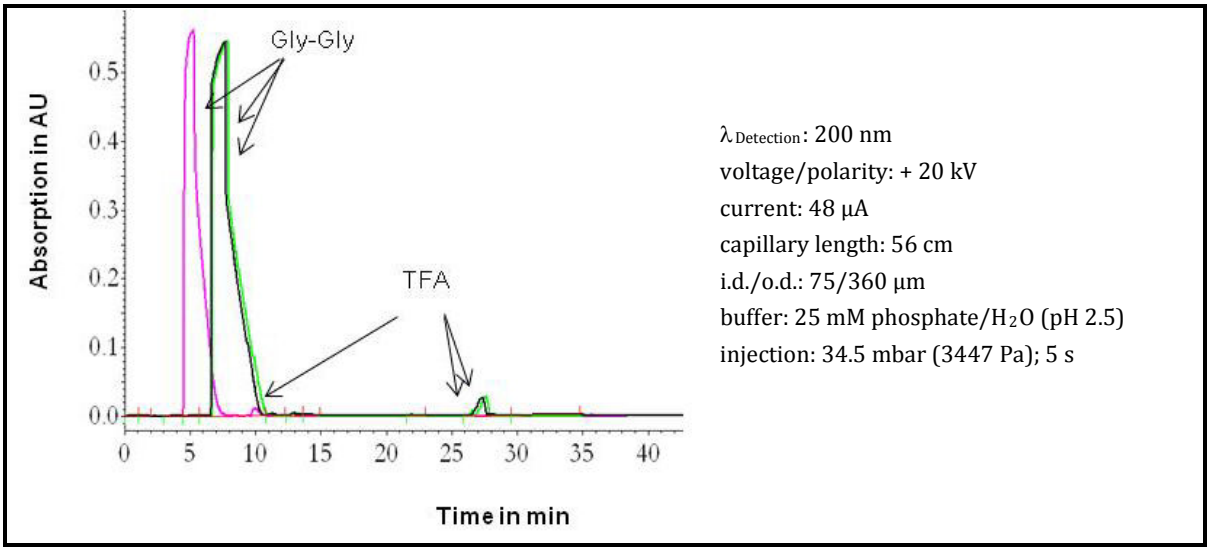


**Figure 2.57:** Overlay of three electropherograms of the glycyl-glycin (250 mM) and TFA (250 mM) CE separation using a normal capillary (black) and a capillary with a flow cell before the UV/Vis detector (pink) and after the UV/Vis detector (green) [42]

These results show that the CE separations and electrophoretic current flows were not influenced or distorted significantly by the flow cell capillary. Furthermore, it was demonstrated that the glued flow cell capillary is a possible solution between the CE separation and the NMR sensitivity, since all the above demonstrated results present positive flow cell capillary performances with sufficient peak resolution. However, further developments are necessary for the ultimate goal of having ideal flow cell capillaries, which for example do not show any sample-surface interactions.

# 3 Integrated Portable CE-NMR System

## 3.1 Commercial CE Coupled to Portable Microcoil NMR

Reproduced with permission from:

**Joana Diekmann**, Kristl L. Adams, Gregory L. Klunder, Lee Evans, Paul Steele, Carla Vogt, and Julie L. Herberg, Portable Microcoil NMR Detection Coupled to Capillary Electrophoresis, *Analytical Chemistry* **2011**, 83, 1328-1335.
http://pubs.acs.org/doi/full/10.1021/ac102389b

Copyright 2011 American Chemical Society.

### 3.1.1 Declaration of my Contribution

My personal contribution for this publication includes the method development, the planning and execution of experiments, the result analysis, the literature search and the writing of the manuscript as a first author. Kristl Adams and Gregory Klunder proposed many useful suggestions for this project, supported me in the laboratory and gave the main correction for the manuscript. Lee Evans helped to build the NMR probe heads including the tuning and matching box. Paul Steele programmed the software and designed schematic figures. Julie Herberg and Carla Vogt gave professional guidance.

### 3.1.2 Abstract

High-efficiency separation techniques, such as capillary electrophoresis (CE), coupled to a nondestructive nuclear magnetic resonance (NMR) spectrometer offer the ability to separate, chemically identify, and provide structural information on analytes in small sample volumes. Previous CE–NMR coupled systems utilized lab-scale NMR magnets and spectrometers, which require very long separation capillaries. New technological developments in electronics have reduced the size of the NMR system, and small 1-2 T permanent magnets provide the possibilities of a truly portable NMR. The microcoils used in portable and lab-scale NMR may offer the advantage of improved mass sensitivity because the limit of detection (LOD) is proportional to the coil diameter. In this work, CE is coupled with a portable, briefcase-sized NMR system that incorporates a microcoil probe and a 1.8 T permanent magnet to measure $^{19}F$ NMR spectra. Separations of fluorinated molecules are demonstrated with stopped- and continuous-flow NMR detection. The results demonstrate that coupling CE to a portable NMR instrument is feasible and can provide a low-cost method to obtain structural information on microliter samples. An LOD of 31.8 nmol for perfluorotributylamine with a resolution of 4 ppm has been achieved with this system.

## 3.2 Portable CE-NMR System

In this chapter, results of the unique miniaturized on-line CE-NMR system are summarized using the glued flow cell capillary. Although all the individual components of the system have been explained in the previous chapters, this section presents the results of the portable CE-NMR instrument, which describes a cutting-edge technology. The chapters will focus on the experimental setup of the custom-built system and preliminary experiments along with on-line CE-NMR measurements.

### 3.2.1 Portable CE-NMR Instrument Setup

The miniaturized and custom-built CE-NMR instrument is demonstrated in Figure 3.1 and all parts of this system have been described in detail in Chapter 2. The CE-NMR system consists of the following components, whereas the UV/Vis and the NMR detector were 7 cm apart:

(1) 1.6 T $Sm_2Co_{17}$ permanent magnet
(2) solenoid microcoil with circuit box
(3) UV/Vis light source
(4) CE separation capillary ($L$ = 65 cm)
(5) CE inlet vial with Pt-electrode
(6) CE outlet vial with Pt-electrode
(7) UV/Vis fiber optic cable
(8) height adjustable vial holders

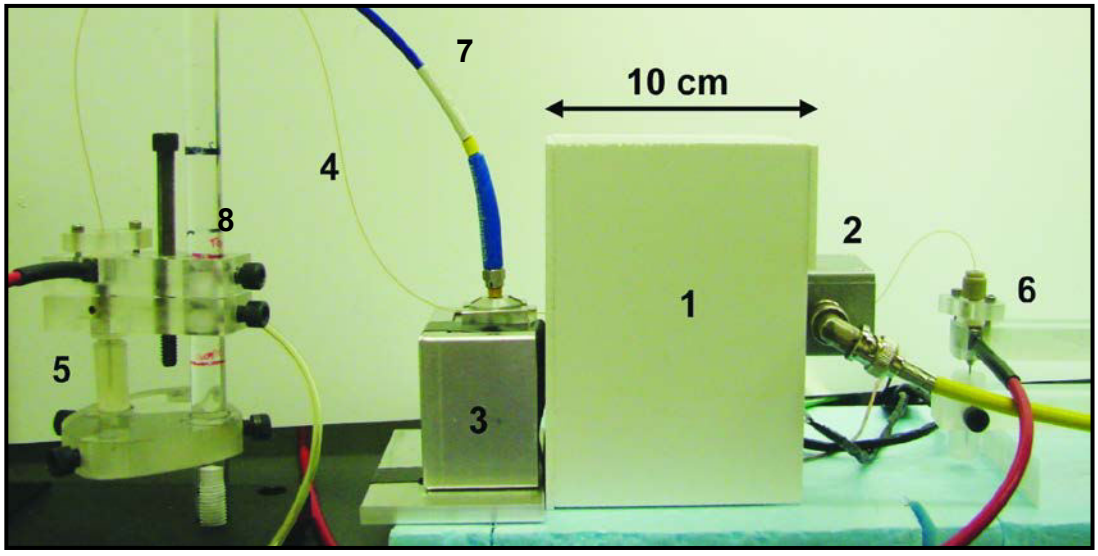


**Figure 3.1:** Custom-built miniaturized CE-NMR instrument with: (1) 1.6 T $Sm_2Co_{17}$ permanent magnet (without blue closed-cell foam), (2) solenoid microcoil ($V_{observ}$ = 125 nL), (3) UV/Vis light source, (4) CE separation capillary ($L$ = 65 cm), (5) and (6) CE inlet and outlet vial with Pt-electrode, (7) UV/Vis fiber optic cable, and (8) height adjustable vial holders

The picture does not show the PC ventilators, the optical spectrometer, the NMR electronics, the high voltage supply, and the computer. However, the whole coupled instrument can be transported in a standard suitcase and has a footprint of about 40 x 30 x 40 cm.

### 3.2.2 CE Current Effects on NMR Performance

Olson et al. [25] described the magnetic field degradation in NMR spectroscopy due to the induced $B_2$ by electrophoretic current for geometries in which the CE capillary and the static magnetic field are not parallel, *e.g.* in the case of using a solenoidal microcoil. During their experiments they observed a significant line width broadening of 18 Hz for the NMR peaks while increasing the CE current from 0 μA to 94 μA (see Figure 3.2).

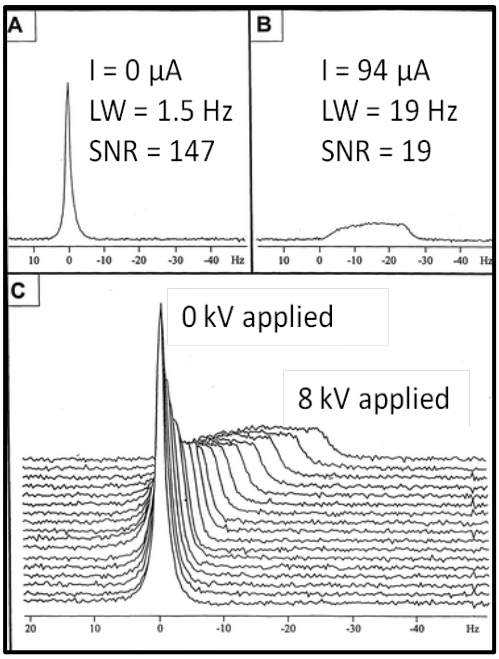


**Figure 3.2:** $^1$H NMR signal of $H_2O$ in 50 mM sodium borate buffer (pH 9.3). **A)** Resonance signal referenced to 0 Hz with no applied voltage. **B)** Observed broadening with 8 kV applied voltage. **C)** Series of spectra ranging from 0 to 8 kV [25]

Although Wu et al. [22] have suggested that the effect can be cancelled through the use of the magnet shim adjustments; other methods for minimizing the effects of the CE current have usually been employed. One possibility is the use of periodically stopped-flow CE-NMR experiments, where the sample is parked in the active volume of the NMR coil by turning off the separation voltage [80]. Li et al. suggested signal processing to restore spectral lines from the distorted NMR spectrum [81]. Another option is to use more complicated hardware solutions, *e.g.* the multiple solenoidal RF coil NMR probe [27], or the two-loop cycle CE, where two different CE separation capillaries are used to acquire NMR data from one RF coil while continuing a separation in the other capillary [82].

The $B_2$ inhomogeneity produced by the electrophoretic current that travels through the capillary cross-section of the capillary *r* can be calculated using Ampere's Law [25]. Figure 3.3 schematically shows some representative magnetic fields created by the CE current. The magnetic field is strongest at the outer edge of the capillary and falls to zero at the center, as depicted by the arrows along the horizontal *y*-axis. The magnetic field ($B(a)$) created inside the capillary at an arbitrary point (P = ($a$,β)) is given by Equation 3.1, with the magnetic constant ($\mu_0$) [83].

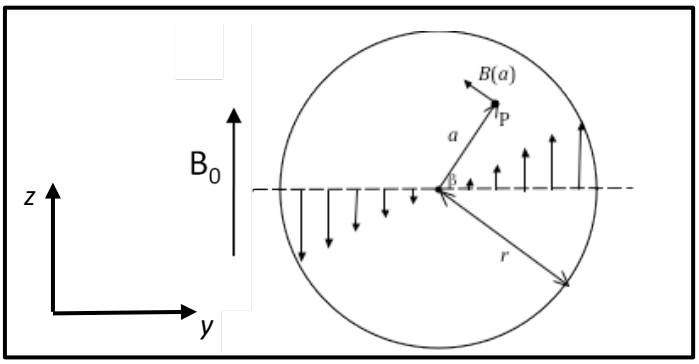


**Figure 3.3:** Schematic figure of the capillary cross-section to show $B(a)$ created at P by CE current flowing out of the page and distributed uniformly over the capillary of $r$

$$B(a) = \frac{\mu_0 I a}{2\pi r^2}\hat{\beta} = \frac{\mu_0 I a}{2\pi r^2}(-\sin\beta\,\hat{\mathbf{y}} + \cos\beta\,\hat{\mathbf{z}}) \qquad \text{Equation 3.1}$$

Since the effect of NMR spectral broadening depends only on the $z$ component of the induced magnetic field, which aligns with $B_0$, Equation 3.1 can be simplified to:

$$B_z = \frac{\mu_0 I}{2\pi r^2} a\cos\beta = \frac{\mu_0 I}{2\pi r^2} y \qquad \text{Equation 3.2}$$

Hence, the CE current establishes a simple linear field gradient in the $y$ direction:

$$\frac{\partial B_z}{\partial y} = \frac{\mu_0 I}{2\pi r^2} \qquad \text{Equation 3.3}$$

This suggests that the $y$ shim of the NMR magnet can be adjusted to correct for the effects of the CE current. To prove this concept, NMR spectra were taken while the CE current was switched on and off. The different sizes of capillary i.d. were studied, since this is the only other variable in the above equation.

Figure 3.4 a shows $^1$H NMR spectra of $H_2O$ in 50 mM phosphate buffer with the CE current on and off using a normal 75 μm i.d. capillary. At 0 μA (no CE current) the $H_2O$ peak had a FWHM of 1.5 Hz; with the current raised to 37 μA, it broadened to a 20 Hz wide peak with an elliptic shape, which is expected for cylindrical NMR samples that have an offset in a transverse linear shim. With the CE current still at 37 μA, the $y$ shim current was adjusted and the narrow NMR peak was re-established with similar linewidth and shape, within the experimental error, as when no CE current was flowing, as shown in the figure.

Using this shim technique, the significant line broadening could be overcome for all CE currents in our experiments. Also, the EOF, which can lead to NMR line broadening due to the finite residence time of the sample in the NMR coil [84], did not affect the NMR resolution in our experiments.

The shim-correction of the CE current effects can be understood quantitatively, as shown in Figure 3.4 b. The CE current was varied between 0-40 μA and the $y$ shim was adjusted so that the $H_2O$ $^1$H NMR linewidth was always minimized to ~1.6 Hz. Figure 3.4 b plots the required shim gradient strength as a function of CE current. The correlation is linear, and was successfully used to calculate the required shim setting from the measured CE current value.

According to Equation 3.3, this line should have a slope of 142 T m$^{-1}$ A$^{-1}$. Experimentally, using gradient strengths measurements from MRI experiments on a similar magnet with the same shim coil design (not shown), the slope was determined to be 194 ± 13 T m$^{-1}$ A$^{-1}$. This is in reasonable agreement, given this indirect MRI characterization of the shim gradient strengths used.

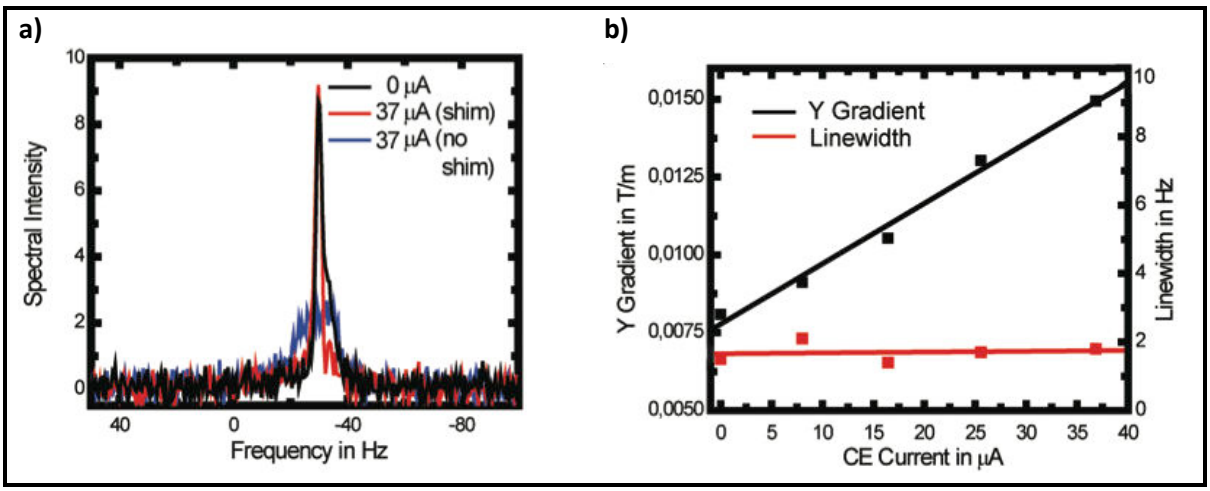


**Figure 3.4:** **a)** $^{1}$H NMR spectra of the $H_2O$ peak in the capillary with no current flowing as well as with current flowing and different shim settings. **b)** Correlations of the shim current settings (black), the linewidth (red) and the flowing CE current (CE-NMR parameters: 65 cm long capillary, i.d./o.d. = 75/360 µm, 50 mM phosphate buffer, 70.9 MHz, 4-scan averages, delay time: 1 s, pulse width: 24 µs, points: 512, sweep width: 4 kHz)

Furthermore, the electrophoretic current induced line broadening effect was investigated when using the larger i.d. flow cell (i.d./o.d. = 400/550 µm) capillary (see Figure 3.5).

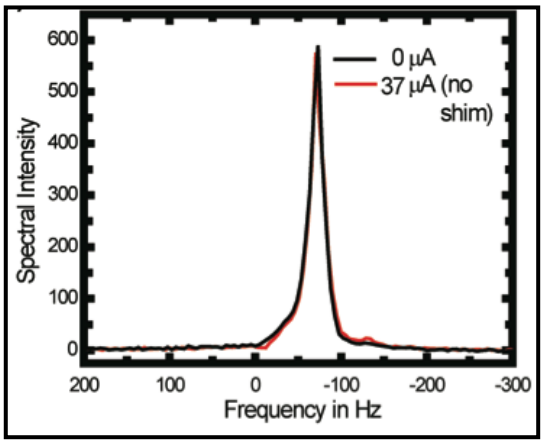


**Figure 3.5:** $^{1}$H NMR single scan spectra of pure $H_2O$ (55 M) using the 400 µm i.d. (550 µm o.d.) flow cell capillary with and without current flowing and no shim adjustments (CE-NMR parameters: 65 cm long capillary, 50 mM phosphate buffer, 70.9 MHz, pulse width: 24 µs, points: 512, sweep width: 4 kHz)

No line broadening in the frequency domain ($\Delta f$) was detected, which is due to the $r^{-2}$ dependence shown in the equations above. To quantify these results, Equation 3.3, the mathematical relationship between $B$, the gyromagnetic ratio ($\gamma$) and the NMR frequency are

used to calculate the line broadening effects caused by CE currents for different i.d. capillaries (see Equation 3.4).

$$\Delta f = \gamma \cdot \Delta B = \gamma \cdot \Delta y \cdot \frac{\partial B_z}{\partial y} = \gamma \cdot 2r \cdot \frac{\mu_0 I}{2\pi r^2} = \frac{\gamma \mu_0}{\pi} \cdot \frac{I}{r} \qquad \text{Equation 3.4}$$

Equation 3.4 shows that the line broadening effect is proportional to the CE current and reciprocal to the radius of the capillary. For the above explained flow cell experiment (i.d./o.d. = 400/550 µm) and a maximum current of 40 µA approximately 3 Hz of broadening were expected, which was not observable given the NMR linewidth in the flow cell of 16 Hz. This means that along with providing improvements in the NMR sensitivity, the flow cell design also reduces the deleterious effects of the CE current.
Using Equation 3.4 the CE current induced frequency drifts can be calculated for different capillary dimensions to estimate the effect on the line broadening and the NMR resolution (see Figure 3.6).

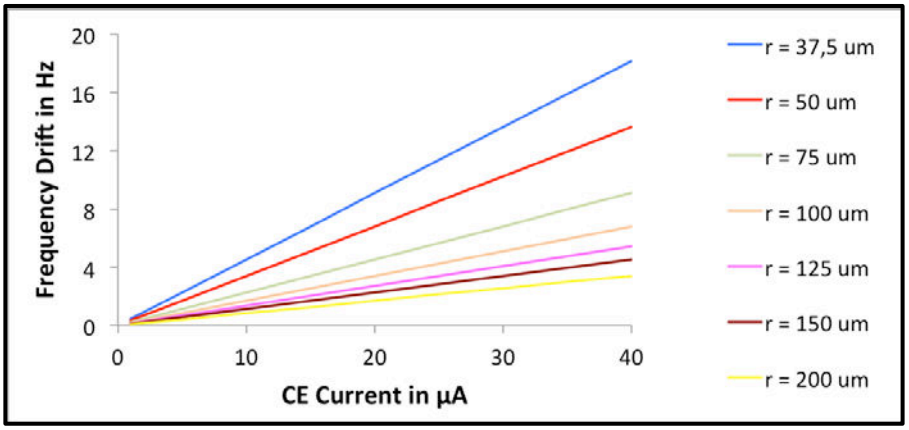


**Figure 3.6:** Calculated correlations of the frequency drifts and the flowing CE current in different i.d. capillaries

This chapter shows that the signal linewidth increase, due to the CE current effects, can be cancelled out even with using solenoidal microcoils, which have an integrated shim coil system. The spectral resolution is not lowered and the sensitivity does not decrease when these hand-wound coils are used. Furthermore, working with the larger i.d. capillaries electrophoretic current effects can be almost neglected, due to the reduced resolution of the NMR spectrum, which is a result of the larger observable coil volume. To show how the CE-NMR data will look like which is produced with this system the next chapter demonstrates a continuous flow CE-NMR experiments.

### 3.2.3 Continuous On-line CE-NMR

For the demonstration of an on-line, continuous flow CE-NMR experiment, 1 M PFOA was used which was dissolved in IPA and 50 mM TRIS CE electrolyte in a methanol / water mixture including 2,4-DNBA acid as the chromophore. The negative 25 kV high voltage was

turned on as soon as the sample was injected using syringe pressure ($V_i \approx 500$ nL). As already stated in previous chapters, typical CE injection volumes take up not more than 1-2 % of the overall capillary volume. The flow cell capillary (65 cm long) used in this experiment had a total volume of about 3000 nL, so that the injected PFOA sample volume filled 17 % of the capillary. This high sample volume caused an overloaded capillary, resulting in broad sample peaks, and changed the current flow during the experiments, as seen in the results below.

The UV/Vis electropherogram in Figure 3.7 shows the light intensity while the electrolyte and the sample were passing the optical detection window during the experimental time. $^{19}$F NMR data were acquired consecutively during the CE-NMR experiment, with a repetition time of 1 s. Signal averaging, which increased the SNR and decreased the overall size of the detected data, was implemented by acquiring 4 scans. The $^{19}$F NMR figure displays the magnitude of the initial part of the consecutively taken FIDs that are the NMR signal strength, plotted against the time of acquisition.

In the beginning of the experiment, a low UV/Vis signal was observed while the capillary was filled with the buffer. When IPA reached the UV/Vis detection window the light intensity increased to 700 counts because the absorptivity of the IPA was lower than that of the buffer. After 980 s, the negative signal peak of PFOA (1 M) was observed correlating to an average velocity of 0.038 cm s$^{-1}$ ($v$ = capillary length to detector/sample migration time) with an electrophoretic flow rate ($F$) of 1.68 nL s$^{-1}$ ($F$ = velocity x capillary cross-sectional area). The PFOA peak width, measured from baseline to baseline, was 290 s (≈ 5 min) long, corresponding to a volume of ≈ 490 nL, as expected due to the injected sample volume. This very broad CE peak was due to the non standard CE conditions using large sample volumes.

The CE current which is not shown, was also influenced by the high sample injection volume. It increased by 10 % in the first 10 min of the experiment and then decreased back to the normal separation current. However, these current variations did not interfere with the NMR, since the NMR experiment is not influenced by the CE current, when the larger i.d. capillaries were used as sample container (see Chapter 3.2.2).

At the beginning of the $^{19}$F NMR run, the acquired FIDs represent the noise level of the experiment, because the CE buffer did not contain any $^{19}$F. After 971 s $^{19}$F NMR signals were detected, with the signal growing in strength. The NMR signal strength reached a maximum at 1156 s and then decayed back to the noise level at 1341 s, as the PFOA filled and then emptied the flow cell. Therefore, the duration of the NMR detection was about 370 s. Compared to the UV/Vis data, a broader PFOA peak was observed in the NMR experiment, due to the flow cell characteristics, since it is not a point detector like the UV/Vis detector. Calculating the amount of time it took the PFOA sample to fill the flow cell ($V_{observ}$ = 125 nL) the flow rate $F$ = 1.68 nL s$^{-1}$ from above was used, resulting in about 74 s for the sample to fill the flow cell. Since 500 nL sample were injected, the flow cell was filled 4 times during the whole experiment, requiring 296 s. However, once the flow cell was filled, it took an additional 74 s for the tailing sample edge to empty the cell again. Hence, NMR spectra of the PFOA sample were acquired for 370 s (= 296 s + 74 s), consisting with the observed NMR peak signal.

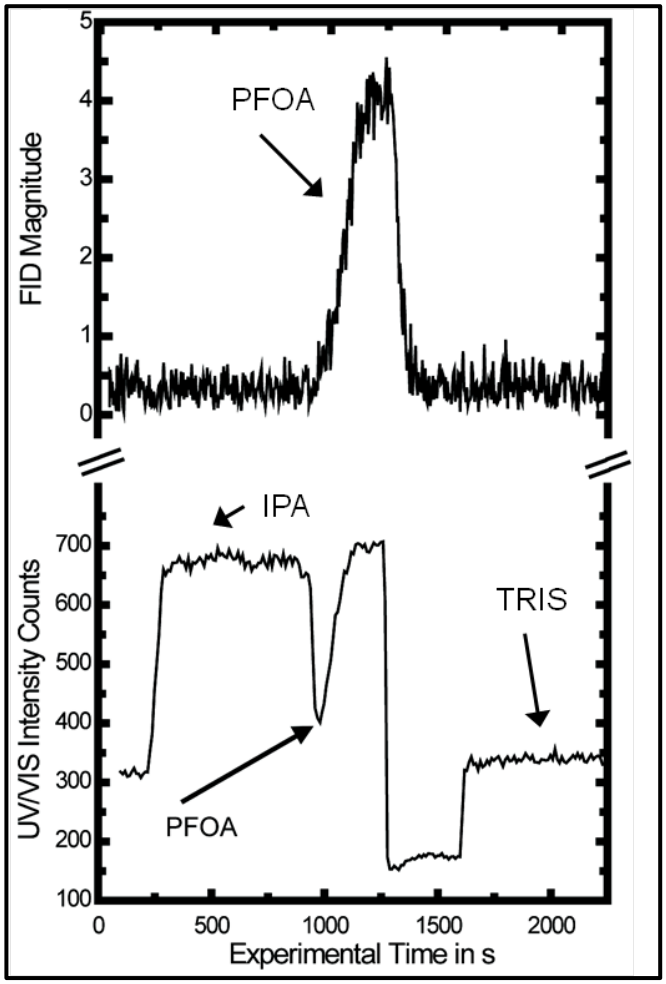


**Figure 3.7:** UV/Vis intensity and $^{19}F$ NMR FID magnitudes detected during the CE-NMR experiment plotted against the experimental time of a 1 M PFOA sample (CE-NMR parameters: 65 cm long flow cell capillary, 37.5 cm to UV/Vis detector, 44.5 cm to NMR coil, 50 mM TRIS buffer, 500 nL injection volume, -25 kV, 252 nm, 66.7 MHz, 4-scan averages, delay time: 1 s, pulse width: 24 μs, points: 1024, spectral width: 16 kHz)

The positions of the PFOA signals on the experimental time axis of the UV/Vis and the NMR detector were also consistent. The UV/Vis peak had its maximum at 980 s, whereas the center of the NMR signal occurred at 1156 s. The sample plug therefore needed 176 s to travel the 7 cm distance between the UV/Vis and the NMR detectors, resulting in a velocity of 0.039 cm $s^{-1}$ similar to the value calculated above using the UV/Vis data. These results indicate that the PFOA plug uniformly travels through the capillary and the flow cell and that no dead volume or carry over effects were detectable using the NMR spectroscopy.

Figure 3.8 demonstrates the final NMR data used to provide structural information of the sample compound, which is the great advantage of using NMR as the detector. Figure 3.8 a shows one of the $^{19}F$ FIDs acquired in the middle of the sample plug passage time. The Fourier Transform of this FID is shown in Figure 3.8 b, representing the NMR spectrum. It clearly identifies the plug as containing PFOA (compare to Chapter 2.2.6.1). The NMR spectrum shows the individual $CF_3$ peak at -84.5 ppm and $CF_2$ peaks at -120 to -130 ppm. Note that this data was acquired while the CE current and the EOF were both present.

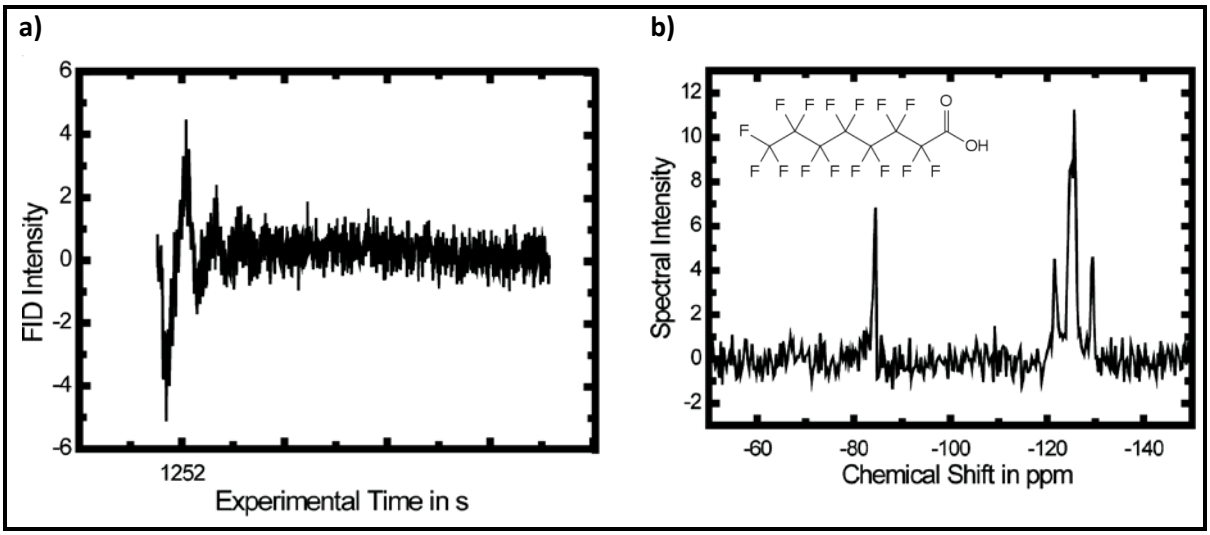


**Figure 3.8:** **a)** An individual $^{19}F$ FID signal of PFOA during the CE-NMR experiment and **b)** $^{19}F$ NMR spectrum of 1 M PFOA taken from the FID signal in the experiment while CE current and fluid-flow were present (CE-NMR parameters: 65 cm long flow cell capillary, 37.5 cm to UV/Vis detector, 44.5 cm to NMR coil, 50 mM TRIS buffer, 500 nL injection volume, -25 kV, 252 nm, 66.7 MHz, 4-scan averages, delay time: 1 s, pulse width: 24 μs, points: 1024, spectral width: 16 kHz)

To show reproducibility of the CE-NMR data, Diekmann et al. ran the same experiments using a 1 M PFPA sample [85]. Similar results were obtained during this run, verifying the CE-NMR performance of the system.

Although these CE-NMR experiments were not carried out using standard CE conditions, the high sample injection volumes can be scaled down. Due to the significant improvement in the NMR resolution and sensitivity it would be possible to use smaller injection volumes and lower concentrations. To ensure that the flow cell fills with the desired sample, an injection volume of about 100 nL should be used. In addition to that, the concentration of the sample could be decreased to 500 mM.

The chapter demonstrated for the first time that it is possible to run on-line, continuous flow CE-NMR experiments on a portable instrument in real time, acquiring UV/Vis and NMR data simultaneously. The NMR data provides structural information of the compound, identifying it specifically. To get an idea of further applications of this setup the next chapter summarizes additional areas in which this portable CE-NMR system could be used.

## 3.3 Further Applications

The demand for inexpensive, rapid, and fully portable chemical instruments continues to increase, such that it is likely that portable CE-NMR systems will find use in a wide variety of settings [1]. These diverse fields include different applications in multiple research and industrial areas of the custom-built CE-NMR system as well as further hardware developments to achieve sensitivity enhancements or multiple coupled analytical devices.

Possible applications are presented by bench chemistry in research laboratories or industries. Utilizing portable CE-NMR, routine analysis of complex sample compositions and reaction mixtures at the laboratory workbench, the fume hood, or in the glove box can be completed. These tasks could include impurity testing of *e.g.* synthesized pharmaceuticals in industry, such that the drugs are separated by CE to identify possible product contaminations and further acquire $^{1}H$ or $^{19}F$ NMR spectra for structural identification. The same concept can be used to monitor reagents and chemical reactions or to control the quality of liquid products, such as fuel, beverages, and oils [94]. Due to the low-cost and robustness of the CE-NMR instrument, it can be used in academia to demonstrate the principles of a hyphenated system and to explain the fundamentals of NMR by operating it on their own. Furthermore, due to its size, the portable device is valuable for field analysis, *e.g.* on research ships to screen possible analyte locations before sample is taken, or on exploration trucks to acquire quick information about water contents or other fluids.
As presented in this research work, a variety of PFA compounds were analyzed using the CE-NMR instrument. These perfluorinated substances are of great interest such that environmental and health concerns increase due to their persistence (*e.g.* in water) and their bioaccumulation in humans (*e.g.* blood or liver) as well as in animals (*e.g.* polar bears or fish). The most dominant PFA intake for humans is drinking water and food. In addition, several other industrial products contain PFA because of their unique chemical and physical characteristics, e.g. in fire extinguisher foams, as nonstick coatings in frying pans, and as impregnator in textiles. In general, liquid chromatography coupled to mass spectrometry (MS) is used for the analysis of these substances [90][96][97]. Utilizing the CE-NMR instrument has the advantage of preconcentrating the low amounts of the PFA substances and to get identifying structural analysis.

To broaden the utilities of the portable CE-NMR instrument, hardware developments can lead to a variety of more applications. Interesting is the trend to hyphenate multiple techniques such as LC-NMR-MS to provide multidimensional layers of knowledge, critical to optimize analyzes [95]. The CE-NMR-MS method combination would lead to a sample separation including an absolute sample mass and molecular structural information data acquisition. The same idea, to hyphenate analytical instruments, is used in process analytical technologies to control process strategies. Coupled portable instruments allow for rapid analysis at the point of interest and collect large amounts of distinctly different types of information, such as chromatography and spectroscopy information [98][99][100].

A critical aspect for many CE-NMR applications is the enhancement of the inherently low NMR mass sensitivity. In addition to take advantage of the cost-effective approach of using microcoils, hyperpolarization, such as dynamic nuclear polarization, can be utilized. As these polarization technologies develop further, couplings of hyperpolarization with microcoil CE-NMR are likely, to achieve even greater sensitivity enhancements. Further improvements to detect a wider range of heteronuclei, not only $^{1}H$ or $^{19}F$, are also an important part of expanding the scope of CE-NMR [13].

These examples show the wide variety and continuously growing areas of applications for the home-built, portable CE-NMR instrument.

# 4 Summary and Outlook

This research work demonstrates significant progress towards the unique portable CE-NMR instrument which provides several advantages for applications in analytical chemistry, pharmaceutical industries, and academia. A compact CE hyphenated to a miniaturized microcoil NMR instrument offers the promise of unmatched analytical information due to the chemical separation and the information-rich, non-destructive structural identification of the compounds. The most important advantages of this new cutting-edge, on-line coupled CE-NMR technology are summarized in Table 4.1.

**Table 4.1** Advantages of the miniaturized, on-line coupled CE-NMR instrument

| |
|---|
| 1.) Low-cost, robust system with reduced maintenance requirements |
| 2.) Quick, on-site identification of substances in remote locations |
| 3.) Small instrument footprint |
| 4.) Sample requirements for analysis: µL-nL range |
| 5.) Non-destructive, on-line chemical detection and chemical separation |
| 6.) On-line preconcentration of samples with CE |
| 7.) NMR sensitivity enhancement by detection coil size reduction |
| 8.) Potential for multidimensional coupled systems (*e.g.* CE-NMR-MS) |

For the combination of this portable device various challenges were faced, including *e.g.* the inherent sensitivity lack of the NMR and the distorting effects of the CE current during the NMR experiment. To resolve these difficulties, the development of the CE-NMR system was subdivided into its three major components, consisting of the CE system, the NMR detector, and the separation capillary, for individual optimizations. Later, these instrumental parts were coupled to show the feasibility of this analytical system.

The custom-built, portable CE instrument had a footprint of 30 x 30 x 20 cm and included a UV/Vis light source connected to a fiber optic, a hand-held UV/Vis spectrometer, CE inlet and outlet vial holders with variable heights for buffer and sample vials, two ring Pt-electrodes, a high voltage power supply, a syringe assembly to flush the capillary, and two PC ventilators for cooling. In order to build a small, user-friendly CE device, a compact CZE2000 high voltage supply with constant, fully adjustable voltage/current outputs and quickly reversible polarity switching was chosen. The CE detection was achieved using a palm-sized UV/Vis spectrometer, and two types with different power consumptions were evaluated. The USB2000+ spectrometer, requiring more power, showed better sensitivity and no data post-processing methods, such as smoothing algorithms, *e.g.* Moving Averages or Savitzky-Golay, were needed. In addition, the portable UV/Vis spectrometer was integrated into a commercial, lab-scale CE instrument to acquire consecutive electropherograms from the same CE run for comparison purposes. The results confirmed that it was possible to detect

equivalent data for both spectrometers, showing the characteristic asymmetric sample peak shapes, which were due to the high sample concentrations, as well as no significant diffusion effects along the capillary, and reproducible migration times. For sample introduction a simple, practicable hydrodynamic injection technique, based on the siphoning effect, was used. To show the reproducibility as well as the linear correlation of the injection volume with the height difference and the injection time, the technique was validated using a break-through measurement. The results indicated a good reproducibility, RSD values of 0.9-1.8 %, and were comparable with theoretical calculations, showing that this injection technique was well suited for the custom-built CE instrument. A further critical aspect during CE separations was the generated Joule heating in the CE capillary, such that efficient cooling methods had to be used for heat dissipation. The portable CE system was based on an air cooled mechanism operating two PC ventilators. Acquiring Ohm's Law Plots demonstrated a much smaller linear voltage-current correlation for the portable system, compared to a commercial CE, when using higher ionic strength buffers, *e.g.* 25 mM phosphate buffer. Testing buffers with lower concentrations, *e.g.* 5 mM phthalic acid, resulted in linear plots for the custom-built CE. Additionally, the importance of switching on the PC ventilators during the CE separations was shown in these Ohm's Law Plots and in long-term experiments. Approximately 20 % less current was monitored with running PC ventilators. Before CE separations were performed on the custom-built CE, different experiments were optimized and tested on a commercial, lab-scale CE system under challenging CE conditions, such as high sample concentrations. Two sample mixtures (glycyl-glycin/TFA and PFPA/TFA) and different concentrations (5 mM, 100 mM, and 500 mM) were used. Both measurements showed promising results with baseline separated peaks. Furthermore, the PFPA/TFA sample mixture was quantified using its peak areas for the calibration in the 100-500 mM range ($R^2 > 0.99$). Transferring this PFPA/TFA run to the portable CE system, reproducible separations were achieved showing the capability of the custom-built CE device. Another crucial part of this work was the implementation of preconcentration techniques for on-line sample stacking which is one of the great advantages in CE experiments. Therefore, tITP-CE and LVSEP were used to show preconcentration effects on a five component PFA mixture. In contrast to the high capability of tITP-CE, the experiments just showed minor stacking effects, such that this technique needs further optimization. The LVSEP method achieved a significant sample preconcentration effect of approximately two orders of magnitude for a 0.1 mM PFA sample mixture.

The miniaturized microcoil NMR instrument and the operating software were developed at ABQMR and included a small permanent magnet with integrated 1$^{st}$ and 2$^{nd}$ order shim coils, manual shim control electronics, a single-board NMR spectrometer, a hand-wound microcoil probehead, a temperature control unit and a laptop computer. For spectra acquisitions 90° one-pulse excitations with a pulse width of 24 µs were acquired at 70.9 MHz for $^{1}$H NMR and 66.7 MHz for $^{19}$F NMR. Two different microcoil geometries were built and tested in the portable NMR system. Due to the advantageous characteristics of the slotted microcoil in the

CE-NMR instrument, avoiding NMR linebroadening because of capillary current, this geometry was used and fabricated at ISAS. However, the production process of this coil was vey time-consuming. Testing this microcoil in a lab-scale NMR system, the resulting spectra showed no visible changes in the linewidth during the applications of capillary currents, as expected. Although the CE-NMR performance of these slotted microcoils seemed promising, there are still challenges for further developments, such as a different permanent magnet design, before these coils can be used in a portable NMR instrument. Therefore, hand-wound solenoidal microcoils (i.d. 690 µm, 960 µm length, 12 turns), manufactured on PCB strips, were used in this research work. The 1.6 T permanent $Sm_2Co_{17}$ magnet weighted 2.4 kg and consisted of internally integrated 1st and 2nd order shim coils. Using those shim coils in the magnet, a 100 fold times more homogeneous $B_0$ compared to the unshimmed magnet was achieved, producing a $^1$H NMR signal FWHM of 10 Hz (= 0.14 ppm). However, $B_0$ of the permanent magnet varied with temperature by -350 to -400 ppm/°C, such that a thermal stabilization system, consisting of aluminum alloys and thermal insulation, had to be built. After constructing this insulation system, temperature influences were investigated and compared to other magnet setups, including a raw magnet without any shielding and a TC magnet. The resulting temperature dependent frequency drifts of the thermally stabilized magnet showed that the insulation served as an effective thermal barrier between the laboratory and the magnet temperatures, such that the NMR frequency just changed with -18 to -26 ppm/°C. This greatly enhanced the usability of the portable NMR system in environments with changing temperatures. A similar temperature dependent frequency drift was observed for the TC magnet (-23 ppm/°C). The raw $Sm_2Co_{17}$ magnet with no additional thermal insulation showed the expected drift of -367 ppm/°C which is not suitable to use for a portable system which undergoes temperature changes in the environment. Conclusively, the sensitivity, the resolution, and the peak shape of the portable NMR performance were investigated. Lorentzian peak profiles and spectral resolutions of 0.02 ppm ($V_{observ}$ = 4 nL) as well as 0.2 ppm ($V_{observ}$ = 125 nL) were achieved using two different sample size containers, enabling access to $^1$H and $^{19}$F NMR analysis. Various analytes, including PFPA, PFOA, ethanol, acetic acid, and citric acid, of concentrations between 0.3 M and 1 M were studied. Comparing these results to lab-scale, high resolution NMR spectra, the experiments in the miniaturized NMR setup demonstrate the capability of performing NMR measurements of molecules containing different $^1$H and $^{19}$F atoms at moderate concentrations for a structural elucidation. Furthermore, these improvements in resolution and sensitivity allowed the detection of samples with concentrations and volumes more comparable with CE.

The custom-built flow cell helped to bridge the gap between the size requirements of CE and those of NMR. Two different techniques to construct these customized flow cell capillaries were employed in this work. Wet, chemical HF etching, a typical technique and widespread in literature, was tested. Even though the fabrication of flow cell capillaries was possible and no significant influences on CE separation resolutions were observed, the reproducibility of the construction process using HF was not straightforward and a lot of different influencing

factors had to be considered. For this reason, along with the dangerous HF handling, the time-consuming etching steps, and the unpredictable flow cell shape, another technique was used. The mechanical gluing technique was a simple approach to fabricate robust, low-cost, and flexible flow cell capillaries. A 1 mm long, cylindrical-shaped, synthetic fused-silica cell (400 µm i.d., 125 nL cell volume) was glued between two 75 µm i.d. capillary pieces, resulting in a very reproducible and uncomplicated construction. Capillary flow profiles were monitored using a colored ink solution and an organic solvent to investigate flow behaviors, bubble formations, and residues of samples in the cell. The syringe pressurized migration profile showed a parabolic, very homogeneous sample plug profile throughout the flow cell capillary. However, a little bit of ink remained at the edges of the cell. These remains could be a result due to the chemical and/or physical interactions of the organic solvent. In addition, the geometry influence of the capillary was monitored, since both of the flow cell sides were never glued in exactly the same way. The experiments ensured that careful and symmetrical gluing of the flow cell capillary was important to minimize sample remains in the capillary. To show the performance of these glued flow cells during CE and NMR runs, individual experiments were performed. NMR results indicated that the flow cell structure and size did not influence the $B_0$ homogeneity and significant improvements in the NMR concentration sensitivity were obtained. When using the flow cell capillaries in the CE instrument two essential parameters had to be investigated: The flow cell capillary should maintain the CE separation, either in terms of sample mixing or resolution loss, and the Joule heating effects during the CE separation, hence the electrophoretic current, should be analyzed. Theoretical assumptions and multiple experiments proved that no changes in current values and no current flow fluctuations were noticeable. Therefore, the Ohm's Law Plots showed similar current-voltage behaviors when compared to a regular capillary, such that identical CE separation parameters could be used when working with the flow cell and the regular capillaries. In addition, the glued capillary did not have any influence on the CE separation before the sample mixture entered the flow cell. Only when the sample plug migrated out of the flow cell, a significant loss in CE resolution was detected, due to the sample expansion in the flow cell. However, the peak shapes and widths still appeared identical, emphasizing the positive flow cell performance in CE and NMR experiments.

The miniaturized CE-NMR instrument combined the three main components (CE, NMR, and flow cell capillary) which were summarized above and had a footprint of 40 x 30 x 40 cm. It could be demonstrated that the effects of the CE current on the NMR resolution could be understood quantitatively and corrected by an adjustment of the NMR shim setting, using the *y* gradient. With these shim alterations linewidths of 1.6 Hz were maintained for all CE currents up to 37 µA, such that the NMR linebroadening could be cancelled out even with solenoidal microcoils. The spectral resolution was not lowered and the sensitivity did not decrease when these hand-wound coils were used in CE-NMR experiments. Furthermore, working with the flow cell capillaries electrophoretic current effects could be almost neglected, due to the reduced resolution of the NMR spectrum, which was a result of the

larger observable coil volume. To show how the CE-NMR data looked like, an on-line, continuous flow CE-NMR experiment was demonstrated for the first time with this unique, miniaturized system. Accordingly, simultaneous NMR and UV/Vis acquisitions during CE experiments were presented in real time, showing that NMR-based detection of CE operations could replace UV/Vis detection. The NMR analysis improved the detection by providing chemical and structural information of the compound, identifying it specifically.

As the last chapter demonstrated, the demand for inexpensive, rapid, and fully portable chemical analysis tools continues to increase, such that it is likely that portable CE-NMR systems will find use in a wide variety of settings.

Still, there are several challenges present requiring further developments to achieve a fully integrated miniaturized CE-NMR instrument which is not straightforward. Figure 4.1 illustrates the significant progress of this research work.

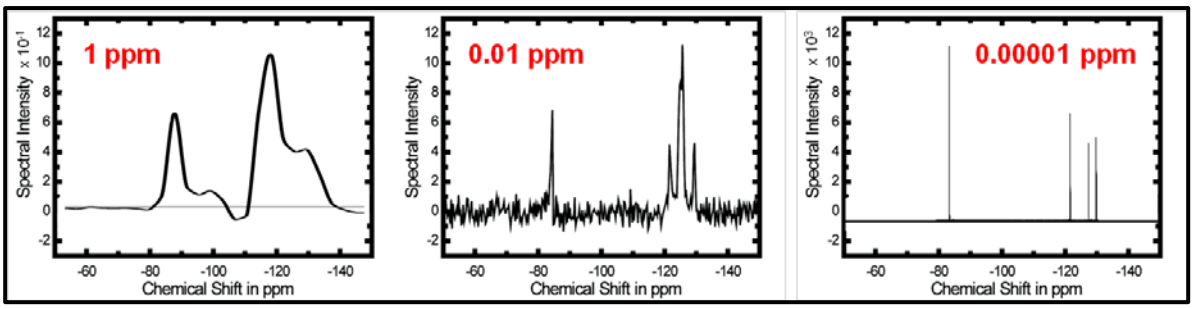


**Figure 4.1:** $^{19}$F NMR spectra of 1 M PFOA (**Left:** 32 scan average on the lower resolution portable NMR setup at LLNL with a resolution of 10 ppm, **Middle:** one scan experiment on the portable CE-NMR setup presented in this work with a resolution of 0.01 ppm, **Right:** 500 MHz high field NMR spectrum with resolution < 0.00001 ppm)

This dissertation presented a future perspective of the current trend towards portable analytical instruments. The ambition of developing the first, on-line coupled CE-NMR system for true portability with sufficient NMR resolution and sensitivity for CE separations in the mM range was succeeded.

# 5 References


[1] G. McMahon, *Analytical Instrumentation: A Guide to Laboratory, Portable and Miniaturized Instruments,* John Wiley & Sons, **2008**

[2] M. E. Lacey, A. G. Webb, J. V. Sweedler, *Monitoring Temperature Changes in Capillary Electrophoresis with Nanoliter-Volume NMR Thermometry,* Analytical Chemistry, 72, 4991-4998, **2000**

[3] A. M. Wolters, D. A. Jayawickrama, C. K. Larive, J. V. Sweedler, *Capillary Isotachophoresis/NMR: Extension to Trace Impurity Analysis and Improved Instrumental Coupling*, Analytical Chemistry, 74, 2306-2313, **2002**

[4] P. Gfrörer, J. Schewitz, K. Pusecker, L. H. Tseng, K. Albert, E. Bayer, *Gradient elution capillary electrochromatography and hyphenation with nuclear magnetic resonance,* Electrophoresis, 20, 3-8, **1999**

[5] A. K. Korir, V. K. Almeida, D. S. Malkin, C. K. Larive, *Separation and Analysis of Nanomole Quantities of Heparin Oligosaccharides Using On-Line Capillary Isotachophoresis Coupled with NMR Detection,* Analytical Chemistry, 77, 5998-6003, **2005**

[6] G. Schwedt, C. Vogt, *Analytische Trennmethoden*, John Wiley & Sons, **2010**

[7] H. Günther, *NMR Spectroscopy – Basic Principles, Concepts, and Applications in Chemistry*, John Wiley & Sons, **1995**

[8] J. K. M. Sanders, B. K. Hunter, *Modern NMR Spectroscopy: A Guide for Chemists*, Second Edition, Oxford University Press, **1993**

[9] D. I. Hoult, R. E. Richards, *The Signal-to-Noise Ratio of the Nuclear Magnetic Resonance Experiment,* Journal of Magnetic Resonance, 24, 71-85, **1976**

[10] A. G. Webb, *Radiofrequency microcoils in magnetic resonance,* Progress in Nuclear Magnetic Resonance Spectroscopy, 31, 1-42, **1997**

[11] M. Spraul, A. S. Freund, R. E. Nast, R. S. Withers, W. E. Maas, O. Corcoran, *Advancing NMR sensitivity for LC-NMR-MS using a cryoflow probe: application to the analysis of acetaminophen metabolites in urine,* Analytical Chemistry, 75, 1536-1541, **2003**

[12] Z. Serber, C. Richter, D. Moskau, J. M. Böhlen, T. Gerfin, D. Marek, M. Häberli, L. Baselgia, F. Laukien, A. S. Stern, J. C. Hoch, V. Dötsch*, New carbon-detected protein NMR experiments using CryoProbes,* Journal of the American Chemical Society, 122, 3554-3555, **2000**

[13] C. J. Jones, C. K. Larive, *Could smaller really be better? Current and future trends in high-resolution microcoil NMR spectroscopy,* Analytical and Bioanalytical Chemistry, 402, 61-68, **2012**

[14] T.L. Peck, R. L. Magin, P. C. Lauterbur, *Design and Analysis of Microcoils for NMR Microscopy*, Journal of Magnetic Resonance, 108, 114-124, **1995**

[15] F. C. Schroeder, M. Gronquist*, Extending the Scope of NMR Spectroscopy with Microcoil Probes,* Angewandte Chemie International Edition, 45, 7122-7131, **2006**

[16] J. Diekmann, K. L. Adams, G. L. Klunder, L. Evans, P. Steele, C. Vogt, J. L. Herberg, *Portable Microcoil NMR Detection Coupled to Capillary Electrophoresis*, Analytical Chemistry, 83, 1328-1335, **2011**

[17] C. J. Jones, S. Beni, J. F. K. Limtiaco, D. J. Langeslay, C. K. Larive, *Heparin characterization: challenges and solutions*, Annual Reviews of Analytical Chemistry, 4, 439-465, **2011**

[18] T. L. Peck, A. G. Webb, N. Wu, R. L. Magin, J. V. Sweedler, *On-line NMR detection in capillary electrophoresis using an RF microcoil*, IEEE, 2, 986-987, **1994**

[19] K. Pusecker, J. Schewitz, P. Gfrörer, L. H. Tseng, K. Albert, E. Bayer, *On-Line Coupling of Capillary Electrochromatography, Capillary Electrophoresis, and Capillary HPLC with Nuclear Magnetic Resonance Spectroscopy,* Analytical Chemistry, 70, 3280-3285, **1998**

[20] T. R. Saarinen, C. S. Johnson, *High-resolution electrophoretic NMR,* Journal of the American Chemical Society, *110,* 3332-3333, **1988**

[21] N. Wu, T. L. Peck, A. G. Webb, R. L. Magin, J. V. Sweedler, *Nanoliter Volume Sample Cells for $^{1}$H NMR: Application to Online Detection in Capillary Electrophoresis*, Journal of the American Chemical Society, 116, 7929-7930, **1994**

[22] N. Wu, T. L. Peck, A. G. Webb, R. L. Magin. J. V. Sweedler, *$^{1}$H-NMR Spectroscopy on the Nanoliter Scale for Static and Online Measurements,* Analytical Chemistry, 66, 3849-3857, **1994**

[23] K. Albert, G. Schlotterbeck, L. H. Tseng, U. Braumann, *Application of on-line capillary high-performance liquid chromatography-nuclear magnetic resonance spectrometry coupling for the analysis of vitamin A derivatives,* Journal of Chromatography A, 750, 303-309, **1996**

[24] K. Albert, *Hyphenation of Chromatographic Separation Techniques with Nuclear Magnetic Resonance Spectroscopy: Present Status and Future*, Analusis, 24, M17-M18, **1996**

[25] D. L. Olson, M. E. Lacey, A. G. Webb, J. V. Sweedler, *Nanoliter-Volume $^{1}$H NMR Detection Using Periodic Stopped-Flow Capillary Electrophoresis*, Analytical Chemistry, 71, 3070-3076, **1999**

[26] H. G. Krojanski, J. Lambert, Y. Gerikalan, D. Suter, R. Hergenröder, *Microslot NMR Probe for Metabolomics Studies,* Analytical Chemistry, 80, 8668-8672, **2008**

[27] A. M. Wolters, D. A. Jayawickrama, A. G. Webb, J. V. Sweedler, *NMR Detection with Multiple Solenoidal Microcoils for Continuous-Flow Capillary Electrophoresis,* Analytical Chemistry, 74, 5550-5555, **2002**

[28] H. Raich, P. Blümler, *Design and construction of a dipolar Halbach array with a homogeneous field from identical bar magnets: NMR Mandhalas,* Concepts in Magnetic Resonance Part B: Magnetic Resonance Engineering, 23B, 16-25, **2004**

[29] J. Schewitz, P. Gfrörer, K. Pusecker, L. H. Tseng, K. Albert, E. Bayer, I. D. Wilson, N. J. Bailey, G. B. Scarfe, J. K. Nicholson, J. C. Lindon, *Directly coupled CZE-NMR and CEC-NMR spectroscopy for metabolite analysis: paracetamol metabolites in human urine,* Analyst, 123, 2835-2837, **1998**

[30] D. L. Olson, M. E. Lacey, J. V. Sweedler, *The nanoliter niche – NMR detection for trace analysis and capillary separation*, Analytical Chemistry, 70, 257A-264A, **1998**

[31] V. Demas, J. L. Herberg, V. Malba, A. Bernhardt, L. Evans, C. Harvey, S. C. Chinn, R. S. Maxwell, J. Reimer, *Portable, low-cost NMR with laser-lathe lithography produced microcoils,* Journal of Magnetic Resonance, 189, 121-129, **2007**

[32] E. Danieli, J. Perlo, B. Blümich, F. Casanova, *Small Magnets for Portable NMR Spectrometers,* Angewandte Chemie International Edition, 49, 4133-4135, **2010**

[33] A. F. McDowell, E. Fukushima, *Ultracompact NMR: $^{1}H$ Spectroscopy in a Subkilogram Magnet*, Applied Magnetic Resonance, 35, 185-195, **2008**

[34] Spellman High Voltage Electronics Corporation, *CZE2000 Instruction Manual*, Hauppauge, New York, USA, **2010**

[35] P. Camilleri, *Capillary Electrophoresis: Theory and Practice*, CRC Press, Second Edition, **1998**

[36] T. O'Haver, *An Introduction to Signal Processing with applications in Chemical Analysis,* University of Maryland at College Park, **2012**

[37] P. Jandik, G. Bonn, *Capillary Electrophoresis of Small Molecules and Ions*, John Wiley & Sons, **1993**

[38] J. P. Landers, *Handbook of Capillary Electrophoresis*, Second Edition, CRC Press, **1997**

[39] F. Lottspeich, H. Zorbas, *Bioanalytik*, Spektrum Verlag, **2006**

[40] H. Engelhardt, W. Beck, T. Schmitt, *Kapillarelektrophorese Methoden und Möglichkeiten,* Vieweg & Sohn, **1994**

[41] T. Hoffmann, *Elektrophoretische Trennverfahren*, Vorlesungsskript, Johannes Gutenberg Universität Mainz, **2010**

[42] M. Cheng, *Grundlagenuntersuchung zur Kopplung von CE und NMR in einem portablen System*, Masterarbeit, Leibniz Universität Hannover, **2011**

[43] Polymicro Technologies, *Flexible Fused Silica Capillary Tubing*, **2008**

[44] *Introduction to Capillary Electrophoresis*, Beckman Instruments INC., Fullerton, California, **1991**

[45] R. J. Nelson, A. Paulus, A. S. Cohen, A. Guttman, B. L. Karger, *Use of peltier thermoelectric devices to control column temperature in high-performance capillary electrophoresis*, Journal of Chromatography A, 480, 111-127, **1989**

[46] M. Holst, *Trennung von fluorierten Säuren mit der (portablen) Kapillarelektrophorese*, Forschungspraktikum, Leibniz Universität Hannover, **2011**

[47] T. Hirokawa, H. Okamoto, N. Ikuta, B. Gas, *Optimization of operational modes for transient isotachophoresis preconcentration-CZE*, Analytical Sciences, 17, i185-i188, **2001**

[48] A. R. Timerbaev, T. Hirokawa, *Recent advances of transient isotachophoresis-capillary electrophoresis in the analysis of small ions from high-conductivity matrices*, Electrophoresis, 27, 323-340, **2006**

[49] M. Schäfer, *Kapillarelektrophoretische Trennung und Isotachophoretische Aufkonzentrierung von perfluorierten, langkettigen Carbonsäuren*, Bachelorarbeit, Leibniz Universität Hannover, **2010**

[50] R. L. Chien, D. S. Burgi, *On-Column Sample Concentration Using Field Amplification in CZE,* Analytical Chemistry, *64*, 489A-496A, **1992**

[51] B. Kim, D. S. Chung, *Large-volume stacking in capillary electrophoresis using a methanol run buffer,* Electrophoresis, *23*, 49-55, **2002**

[52] M. S. Chun, D. S. Chung, *Large volume sample stacking in capillary electrophoresis of weakly acidic compounds using coated capillaries at high pH*, Analytica Chimica Acta, 491, 173-179, **2003**

[53] A. G. Webb, *Microcoil nuclear magnetic resonance spectroscopy,* Journal of Pharmaceutical and Biomedical Analysis, 38, 892-903, **2005**

[54] J.N. Shoolery, Top. Carbon-13 NMR Spectroscopy, 2, 28-38, **1979**

[55] M. E. Lacey, Z. J. Tan, A. G. Webb, J. V. Sweedler, *Union of capillary high-performance liquid chromatography microcoil nuclear magnetic resonance spectroscopy applied to the separation and identification of terpenoids*, Journal of Chromatography A, 922, 139-149, **2001**

[56] J. Schewitz, K. Pusecker, P. Gfrörer, U. Götz, L.-H. Tseng, K. Albert, E. Bayer, *Direct Coupling of Capillary Electrophoresis and Nuclear Magnetic Resonance Spectroscopy for the Identification of a Dinucleotide*, Chromatographia, 50, 333-337, **1999**

[57] C. J. Jones, C. K. Larive, *Mass limited separation and sample detection using cITP microcoil NMR*, 241st National Meeting and Exposition of the ACS, **2011**

[58] J. P. Hornak, *The Basics of MRI*, www.cis.rit.edu/htbooks, **2011**

[59] Y. Maguire, I. L. Chuang, S. Zhang, N. Gershenfeld, *Ultra-small-sample molecular structure detection using microslot waveguide nuclear spin resonance,* Proceeding of National Academy of Sciences of the United States of America, 104, 9198-9203, **2007**

[60] R. Nunlist, *Probe Tuning Techniques*, www.cchem.berkeley.edu/nmr/apps/probetune, **2011**

[61] H. G. Krojanski , J. Lambert, R. Hergenröder, *Capillary Electrophoresis hyphenated with slotted Microstrip Nuclear Magnetic Resonance Detection*, ISAS – Institute for Analytical Sciences, Dortmund, Germany, **2009**

[62] A. F. McDowell, United States Patent, US 8,115,488 B2, *Tuning Low-Inductance Coils at Low Frequencies*, **2011**

[63] J. Diekmann, *Coupling of Capillary Electrophoresis with Nuclear Magnetic Resonance Spectroscopy for the Analysis of Pharmaceutical and Environmental Relevant Compounds*, Masterarbeit, Leibniz Universität Hannover, **2009**

[64] B. Blümich, J. Perlo, F. Casanova, *Mobile single-sided NMR,* Progress in Nuclear Magnetic Resonance Spectroscopy, 52, 197-269, **2008**

[65] G. Eidmann, R. Savelsberg, P. Blümler, B. Blümich, *The NMR MOUSE: A Mobile Universal Surface Explorer,* Journal of Magnetic Resonance, 122, 104-109, **1996**

[66] C. A. Meriles, D. Sakellariou, H. Heise, A. J. Moule, A. Pines, *Approach to High-Resolution ex Situ NMR Spectroscopy,* Science, 293, 82-85, **2001**

[67] V. Demas, P. J. Prado, *Compact Magnets for Magnetic Resonance*, Concepts in Magnetic Resonance Part A, 34A, 48-59, **2009**

[68] J. Liu, *Sm-Co Magnets and Applications*, International Magnetics Association, Electron Energy Corporation, **2010**

[69] K. L. Adams, J. Diekmann, K. L. Klunder, J. L. Herberg, *On-Line Coupling of Capillary Electrophoresis With Portable NMR Detection For Pharmaceutical And Environmental Exposure Applications*, ICMRM, **2009**

[70] L. M. Mosulishvili, V. A. Barnov, N. Ya. Tsibakhashvili, H. Engelhardt, W. Beck, *Enhancing Detection Sensitivity in Capillary Electrophoresis,* Journal of Analytical Chemistry, 56, 512-514, **2001**

[71] D. Holmes, *Basic NMR Concepts: A Guide for the Modern Laboratory*, Handout, Michigan State University, **2004**

[72] D. L. Olson, T. L. Peck, A. G. Webb, R. L. Magin, J. V. Sweedler, *High-Resolution Microcoil $^{1}$H-NMR for Mass-Limited, Nanoliter-Volume Samples,* Science, 270, 1967-1970, **1995**

[73] Agilent Technologies, *Extended Light Path Capillaries*, **2012**

[74] G. Gary, European Patent, EP 0,386,925 A1, *Capillary Zone Electrophoresis Cell System*, **1990**

[75] Y. Xue, E. S. Yeung, *Characterization of Band Broadening in Capillary Electrophoresis due to Nonuniform Capillary Geometries,* Analytical Chemistry, 66, 3575-3580, **1994**

[76] Y. W. Lin, C. C. Huang, H. T. Chang, *Capillary Electrophoretic Separation of dsDNA Under Nonuniform Electric Fields,* Analytical and Bioanalytical Chemistry, 376, 379-383, **2003**

[77] I. D. Henry, G. H. J. Park, R. Kc, B. Tobias, D. Raftery, *Design and Construction of a Microcoil NMR Probe for the Routine Analysis of 20-µL Samples,* Concepts in Magnetic Resonance Part B: Magnetic Resonance Engineering, 33B, 1-8, **2008**

[78] W. S. Law, J. H. Zhao, S. F. Y. Li, *On-line sample enrichment for the determination of proteins by capillary zone electrophoresis with poly(vinyl alcohol)-coated bubble cells,* Electrophoresis, 26, 3486-3494, **2005**

[79] T. Mohamed, *Der Einfluss von Bubble-Cell Kapillaren auf die CE-Trennung von Xanthinen*, Bachelorarbeit, Leibniz Universität Hannover, **2010**

[80] A. M. Wolters, D. A. Jayawickrama, J. V. Sweedler, *Comparative Analysis of a Neurotoxin from Calliostoma canaliculatum by On-Line Capillary Isotachophoresis/$^{1}$H NMR and Diffusion $^{1}$H NMR,* Journal of Natural Products, 68, 162-167, **2005**

[81] Y. Li, M. E. Lacey, J. V. Sweedler, A. G. Webb, *Spectral restoration from low signal-to-noise, distorted NMR signals: application to hyphenated capillary electrophoresis-NMR,* Journal of Magnetic Resonance, 162, 133-140, **2003**

[82] D. A. Jayawickrama, J. V. Sweedler, *Dual Microcoil NMR Probe to Cyclic CE for Continuous Separation and Analyte Isolation,* Analytical Chemistry, 76, 4894-4900, **2004**

[83] D. Halliday, R. Resnick, *Physics,* Second Edition, John Wiley & Sons, **1962**

[84] M. E. Lacey, R. Subramanian, D. L. Olson, A. G. Webb, J. V. Sweedler, *High-Resolution NMR Spectroscopy of Sample Volumes from 1 nL to 10 µL,* Chemical Reviews, 99, 3133-3152, **1999**

[85] J. Diekmann, K. L. Adams, G. L. Klunder, C. Vogt, A. F. McDowell, *Portable Coupled Capillary Electrophoresis and microNMR: Analysis of Perfluoro Carbonic Acids*, ENC, **2011**

[86] S. Kromidas, *Validierung in der Analytik*, Second Edition, Wiley–VCH Verlag & Co KGaA, **2011**

[87] A. G. Webb, *Nuclear magnetic resonance coupled microseparations*, Magnetic Resonance in Chemistry, 43, 688-696, **2005**

[88] H. Russmann, *Analytik der Fluortenside in biologischen Modellsystemen*, Dissertation, Leibniz Universität Hannover, **1997**

[89] H. Stutz, K. Pittertschatscher, H. Malissa, *Capillary Zone Electrophoretic Determination of Hydroxymetabolites of Atrazine in Potable Water Using Solid-Phase Extraction with Amberchrom Resins,* Mikrochimica Acta, 128, 107-117, **1998**

[90] A. H. Neilson, *Organofluorine,* in *The Handbook of Environmental Chemistry*, Volume 3, Part N, Springer, Berlin, **2002**

[91] V. Exarchou, M. Krucker, T. A. van Beek, J. Vervoort, I. P. Gerothanassis, K. Albert, *LC–NMR coupling technology: recent advancements and applications in natural products analysis,* Magnetic Resonance in Chemistry, 43, 681-687, **2005**

[92] L. Steven, S. L. Simpson, J. P. Quirino, S. Terabe, *On-line sample preconcentration in capillary electrophoresis: Fundamentals and applications*, Journal of Chromatography A, 1184, 504-541, **2008**

[93] B. Jung, R. Bharadwaj, J. G. Santiago, *On-Chip Millionfold Sample Stacking Using Transient Isotachophoresis,* Analytical Chemistry, 78, 2319-2327, **2006**

[94] J. Price, picoSpin, LLC, www.picospin.com, **2012**

[95] I. Green, *Fully Integrated Analysis of Metabolites, Impurities, and Degradants Using LC-NMR-MS*, Current Trends in Mass Spectrometry, 12-19, **2006**

[96] D. Barkowski, P. Günther, F. Raecke, D. Wind, *Abschlussbericht am Institut für Umwelt-Analyse IFUA*, Bezirksregierung Arnsberg, 1-10, **2007**

[97] P. d. Voogt, M. Sáez, *Analytical Chemistry of perfluoroalkylated substances*, Trends in Analytical Chemistry, 25, 326-342, **2006**

[98] K. Rübberdt, *Prozessanalytik: Der Weg zur wissensbasierten Produktion*, Trendbericht No. 8: Prozessanalysentechnik, **2012**

[99] M. Koch, *The Impact of Micro-Analytical Instrumentation on PAT Application*, Center for Process Analytical Chemistry (CPAC), University of Washington, **2010**

[100] T. I. Dearing, B. Marquardt, C. Rechsteiner, *Combining NeSSI and Data Fusion for Process Control and Understanding*, FACSS, **2011**

# 6 Appendix

## 6.1 Publication List

| | |
|---|---|
| **Publications** | |
| 01/2011 | Diekmann, J.; Adams, K.L.; Klunder, K.L.; Evans, L.; Steele, P.; Vogt, C.; Herberg, J. L.: "Portable Microcoil NMR Detection Coupled to Capillary Electrophoresis"; Analytical Chemistry, 83 (4), 1328-1335. |
| 08/2009 | Master Thesis – Diekmann, J.: "Coupling of Capillary Electrophoresis with Nuclear Magnetic Resonance Spectroscopy for the Analysis of Pharmaceutical and Environmental Relevant Compounds". |
| **Oral Presentations** | |
| 10/2011 | 38$^{th}$ FACSS Conference (Title: "On-line Coupled Miniaturized Capillary Electrophoresis-Microcoil NMR Device") |
| 08/2011 | 11$^{th}$ ICMRM Conference (Topic: "Miniaturized Capillary Electrophoresis-Microcoil NMR device for $^{1}$H and $^{19}$F Spectroscopy") |
| 07/2010 | ETH Zurich – PhD Colloquium for Spectroscopy (Topic: "On-line Coupling of Portable Microcoil NMR Spectroscopy with CE for the Analysis of Perfluoro Organic Acids") |
| **Poster Presentations** | |
| 10/2011 | 38$^{th}$ FACSS Conference (Title: "On-line Coupled Miniaturized Capillary Electrophoresis-Microcoil NMR Device") |
| 09/2011 | WiFo Bremen 2011 (Title: "On-line Coupled Miniaturized Capillary Electrophoresis-Microcoil NMR Device") |
| 04/2011 | 52$^{nd}$ ENC Conference (Title: "Portable Coupled Capillary Electrophoresis and microNMR: Analysis of Perfluoro Carbonic Acids") |
| 10/2010 | 37$^{th}$ FACSS Conference (Title: "Portable Microcoil NMR Detection Coupled to Capillary Electrophoresis (CE) for the Analysis of Perfluoro Organic Acids") |
| 10/2009 | 36$^{th}$ FACSS Conference (Title: "CE with On-line Portable NMR Spectroscopy for the Analysis of Pharmaceutical and Environmental Relevant compounds") |

## 6.2 Curriculum Vitae

JOANA DIEKMANN

born on June 17th 1985 in Berlin

| **Education** | |
|---|---|
| 10/2009 – 09/2012 | Leibniz University Hannover, Germany (PhD Student in Analytical Chemistry) |
| 10/2007 – 09/2009 | Leibniz University Hannover, Germany (Master of Science in Analytical Chemistry) |
| 08/2004 – 09/2007 | Ruhr University Bochum, Germany (Bachelor of Science in Chemistry) |
| 08/1995 – 07/2004 | Graf-Engelbert-School Bochum, Germany (School leaving Exam) |

# 7 Erklärung zur Dissertation

Gemäß §6(1) der Promotionsordnung der Naturwissenschaftlichen Fakultät der Gottfried Wilhelm Leibniz Universität Hannover für die Promotion zum Dr. rer. nat..

Hiermit erkläre ich, Joana Diekmann, dass ich diese Dissertation mit dem Titel *Development of On-line Coupled Capillary Electrophoresis to Portable Microcoil NMR Detection* selbständig verfasst und die benutzten Hilfsmittel und Quellen sowie gegebenenfalls die zu Hilfsleistungen herangezogenen Institutionen vollständig angegeben habe.

Diese Dissertation wurde nicht schon als Masterarbeit, Diplomarbeit oder ähnliche Prüfungsarbeit verwendet.

_____ _____

Ort, Datum Joana Diekmann